CRYSTALLINITY VARIATIONS OF SMECTITE-ILLITE AND KAOLIN HYDROTHERMAL ALTERATION MINERALS BY USING SWIR SPECTROSCOPY.
A STUDY OF THE RODALQUILAR AU-DEPOSIT, SE SPAIN

LUZ ADRIANA GUATAME GARCIA
February, 2013

SUPERVISORS:
Dr. F.J.A. (Frank) van Ruitenbeek
Drs. J.B. (Boudewijn) de Smeth

CRYSTALLINITY VARIATIONS OF SMECTITE-ILLITE AND KAOLIN HYDROTHERMAL ALTERATION MINERALS BY USING SWIR SPECTROSCOPY.
A STUDY OF THE RODALQUILAR AU-DEPOSIT, SE SPAIN

LUZ ADRIANA GUATAME GARCIA
Enschede, The Netherlands, February, 2013

Thesis submitted to the Faculty of Geo-Information Science and Earth Observation of the University of Twente in partial fulfilment of the requirements for the degree of Master of Science in Geo-information Science and Earth Observation.
Specialization: Applied Earth Sciences – Earth Resources Exploration

SUPERVISORS:
Dr. F.J.A. (Frank) van Ruitenbeek
Drs. J.B. (Boudewijn) de Smeth

THESIS ASSESSMENT BOARD:
Prof. Dr. F.D. (Freek) van deer Meer (Chair)
Dr. P.M. (Paul) van Dijk (External Examiner, University of Twente)

ABSTRACT

Crystallinity variations in the smectite-illite and kaolin hydrothermal alteration minerals are identified by using SWIR spectroscopy in the Rodalquilar caldera complex, which hosts an epithermal Au deposit. Previous research on IR spectrometry carried out in other areas has demonstrated that changes in the structural order of layered silicates can be quantified by analysing the principal absorption features. Spectral parameters measured on those features give an estimate about the position in the crystal structure of the water molecules, hydroxyl groups and other cations, which allow the estimation of *crystallinity* degree and compositional changes of certain minerals. These features act at the same time as geothermometres, and hence as indicators of the conditions of formation of the hydrothermal alteration. Despite of the fact that in the Rodalquilar caldera complex several earlier studies have characterized the hydrothermal system, of which some used remotely sensed techniques, none of these have addressed the *crystallinity* variations of smectite-illite and kaolin minerals in the study of the hydrothermal alteration in this epithermal system. In this research, SWIR spectroscopy is gathered from proximal and remotely sensed sources. The integration of IR spectral parameters with analytical techniques XRD and TGA leads to the identification of gradual *crystallinity* and compositional changes in the smectite-illite and kaolin minerals. Moreover, by extrapolating the spectral parameters to hyperspectral airborne data, the *crystallinity* variations are mapped with some uncertainty. The relationship between the spectral parameters and the distribution of the hydrothermal alteration zones reveals that poorly *crystalline* minerals are associated with weak alteration and lower temperatures, whereas the well *crystallized* ones are related with intense alteration and high temperatures that are typical for the mineralized zones. The interpretation of the *crystallinity* variations leads to establish that 350ºC is the highest temperature in the Rodalquilar system.

This research proves that *crystallinity* variations in smectite-illite and kaolin minerals, and to a lesser degree, compositional variations of smectite-illite, are not only related to the hydrothermal alteration zones, but also by themselves provide enough information about the mineralization system in the Rodalquilar caldera complex. This can be used as a valuable tool in exploration tool on other epithermal mineral deposits.

Keywords: crystallinity, smectite, illite, kaolin, hydrothermal alteration, SWIR spectroscopy, Rodalquilar gold deposit

ACKNOWLEDGEMENTS

This thesis would not have been possible without the contributions and support of several people and institutions who were involved direct or indirectly in the research process. I feel sincerely grateful with all of them, and since I cannot mention everyone I would like to single out a few.

I foremost would like to thank my supervisors Frank van Ruitenbeek and Boudewijn de Smeth for their scientific guidance and for encouraging me to keep searching and learning. Also thanks to Boudewijn for his assistance in the laboratory work.

The sponsoring by the Netherlands Fellowship Programme (NFP) in the completion of the MSc programme is highly appreciated.

I am grateful to Mr. Hay Berden of Mettler Toledo for his cooperation carrying out the preliminary TGA tests and for his advice on the interpretation. I also thank to Dr. S. Harkema TNW-ICE and Mr. T.L.M. Velthuizen TNW-CPM at the University of Twente for their help in the XRD and TGA work.

My gratitude is also to the staff members of the Applied Earth Sciences department for their support in my studies, and especially to Chris Hecker, Harald van der Werff and Wim Bakker for their valuable contributions at particular stages of the research.

Finally, my greatest thanks go to my family: mom, dad, Carolina and Carlos Julio, for their love, for encouraging me on pursuing my studies and for being with me at every time during this period.

TABLE OF CONTENTS

LIST OF FIGURES

LIST OF TABLES

LIST OF APPENDICES

LIST OF ABBREVIATIONS

ASD	Analytical Spectral Devices
FWHM	Full Width at Half Maximum
HypPy	Hyperspectral Python
HS	High sulfidation
LS	Low sulfidation
IR	Infrared
IS	Illite-Smectite
μm	micrometres
nm	nanometres
PIMA	Portable Infrared Mineral Analyser
SQM	Simple Quadratic Method
SWIR	Short-Wave Infrared
TGA	Thermogravimetric analysis or Thermal Gravimetric Analysis
TSG	The Spectral Geologist
VIS	Visible
VNIR	Visible/Near infrared
XRD	X-ray diffraction

Absorption feature parameters

1400D	Depth of the 1400 nm or 1.4 μm (water, OH) absorption feature
1400W	Wavelength position of the 1400 nm or 1.4 μm (water, OH) absorption feature
1400AS	Asymmetry of the 1400 nm or 1.4 μm (water, OH) absorption feature
1900D	Depth of the 1900 nm or 1.9 μm (water) absorption feature
1900W	Wavelength position of the 1900 nm or 1.9 μm (water) absorption feature
2200D	Depth of the 2200 nm or 2.2 μm (AlOH) absorption feature
2220W	Wavelength position of the 2200 nm 2.2 μm (Al OH) absorption feature
2200AS	Asymmetry of the 2200 nm 2.2 μm (AlOH) absorption feature
2100-2500W	Wavelength position of the deepest absorption feature in the 2100-2500 nm (2.1-2.5 μm) range
R####	Reflectance at #### specific wavelength in nanometres or micrometres
####D	Depth at #### specific wavelength in nanometres or micrometres

1. INTRODUCTION

1.1. Research Background

The variations in the structural order of the crystal lattice in smectite, illite and kaolin minerals are mainly caused by the changing temperatures in the geological environment they are formed, therefore they are commonly considered as geothermomethers. As a consequence, these variations have been broadly used in the characterization of low-grade metamorphism, diagenetic processes and hydrothermal alteration systems (Duba and Williams-Jones, 1983; Kubler and Jaboyedoff, 2000). Previous researches have demonstrated the suitability on using IR reflectance spectroscopy for measuring the degree of structural order in layered silicates (Hauff et al., 1990; Kruse and Hauff, 1991), and hence this technique is considered appropriate for the analysis of *crystallinity* changes in different geological settings.

The Rodalquilar gold-alunite deposit, south-eastern Spain, is one of the best-exposed epithermal high-sulfidation systems in the world. The geological evolution as well as the hydrothermal alteration in this deposit have been studied mainly by using petrographical and geochemical techniques (Arribas et al., 1995), although recent research has proved that the implementation of remote sensing spectroscopy is highly convenient in this area (Bedini et al., 2009).

1.2. Problem Definition

In the Rodalquilar caldera, the use of imaging spectrometry has allowed the refinement of the distribution of the hydrothermal alteration zones. Although research published so far has succeeded in retrieving surface information at good level, there are not studies yet about the *crystallinity* and compositional changes of the alteration mineralogy. Such changes detected by using SWIR spectroscopy can explain in greater detail the configuration of the system and can be used as a mineral exploration tool.

Common analytical methods for studying hydrothermal alteration minerals are costly and require complex laboratory work, while the acquisition of ground SWIR spectroscopy permits the efficient, accurate and less cost detection of particular mineral features either in laboratory or in the field.

Thus, this research focuses on identification of *crystallinity* variations in smectite-illite and kaolin minerals in the Rodalquilar caldera. The use of spectroscopy from proximal and remotely sensed sources leads to the interpretation of the mineral variations in relation to the hydrothermal alteration and the configuration of the Rodalquilar system.

1.3. Research Objectives

To study the crystallinity and compositional variations of smectite, illite and kaolin minerals in the Rodalquilar caldera complex by using proximal and remotely sensed SWIR spectroscopy, and to determine the relationship of those variations with the configuration of the hydrothermal system.

Specific objectives

1. To identify the mineralogy in the Rodalquilar caldera complex that presents crystallinity and compositional variations detectable with SWIR spectroscopy, and to determine the parameters for their characterization.
2. To identify the crystallinity and compositional variations in smectite and illite minerals by using SWIR spectroscopy and other complementary techniques.
3. To identify the crystallinity variations in kaolin minerals by using SWIR spectroscopy and other complementary techniques.

4. To determine how the detected mineral variations are related with the configuration of the Rodalquilar system.

1.4. Researh Questions

1. Which is the dominant SWIR active mineralogy that is related with the hydrothermal alteration system?
2. Are there any detectable crystallinity variations in smectite, illite and kaolin minerals along the system?
3. Are there any detectable compositional changes in smectite and illite minerals along the system?
4. Which techniques are more appropriate and successful in the identification of crystallinity and compositional variations of the studied minerals?
5. How is the relationship of the crystallinity and compositional variations of smectite, illite and kaolin minerals with the configuration of the Rodalquilar system?

1.5. Hypothesis

- The dominant mineralogy in the study area corresponds with minerals typical of hydrothermal alteration in high and low sulfidation epithermal systems.
- Smectite, illite and kaolin minerals present variations in their crystal structure and composition. These changes can be identified by the systematic modifications in their SWIR spectroscopy response.
- The studied mineralogical variations are close related with the configuration of the epithermal system, and specifically with the alteration zones.

1.6. Datasets, software and laboratory facilities

The available materials and datasets consist of a compilation of diverse campaigns and research conducted by ITC students and staff in the Rodalquilar area since 2003, including the research theses conducted by Bedini (2005) and Chororoka (2012). The complete dataset consist of:

- Geological map of the mining district of Rodalquilar, Almeria (esc. 1:25.000) (Arribas, 1993)
- Map of alteration zones described by Arribas et al. (1995).
- Subset of an airborne HyMap scene recorded on 11-07-2003 in 126 narrow bands, from 0.45 to 2.048 µm with spatial resolution of 4m/px used by Bedini (2005) and (Bedini et al., 2009).
- 181 rock samples of 137 stations collected in 2003 and 2004 in the Rodalquilar area by different campaigns developed by ITC staff and students (see Appendix 1)
- 235 field and laboratory spectra acquired with ASD FieldSpec and PIMA II by ITC staff and students in the Rodalquilar area in campaigns since 2003 until 2006. Additionally, transect and other stations used by Bedini (2005) (see Appendix 1).

1.7. Thesis Structure

This document presents the most relevant issues about the research in seven chapters: **Chapter 1** gives a general framework for this research, describing the background, problem, objectives and questions. **Chapter 2** describes the geographic location and the geological setting of the study area, and the relevant aspects regarding the mineralization model. **Chapter 3 e**xplains the fundamental concepts about spectroscopy used in this research, as well as aspects concerning mineral crystallinity. **Chapter 4** is a detailed description of the followed methodology, including spectroscopy, XRD and TGA analysis. **Chapter 5** presents the obtained outputs. **Chapter 6** discusses integrally the meaning of the results. Finally, **Chapter 7** presents de conclusions and recommendations.

2. GEOLOGIC SETTING OF THE RODALQUILAR CALDERA COMPLEX

2.1. Location

The Rodalquilar caldera complex is located in the Cabo de Gata volcanic field, Almeria Province, south eastern Spain. It is a 45 Km² area that hosts Rodalquilar epithermal Au alunite deposit (Figure 2-1).

In the eastern part of the Betic Cordillera, the Cabo de Gata volcanic field is bounded by NE-SW strike slip faults, and it is mainly composed of calc-alkaline rocks formed due to the magmatic activity in the Miocene (17-6 Ma) (López Ruiz and Rodríguez-Badiola, 1980) as a consequence of the tectonic activity during the Cretaceous and Tertiary periods. The rocks composition varies between basaltic andesites, andesites, dacites, rhyodacites and rhyolites (López Ruiz and Rodríguez-Badiola, 1980; Di Battistini et al., 1987; Toscani et al., 1990). In the central part of the volcanic field three large Valle-type calderas have been identified, one of them the Rodalquilar caldera complex (Rytuba et al., 1990).

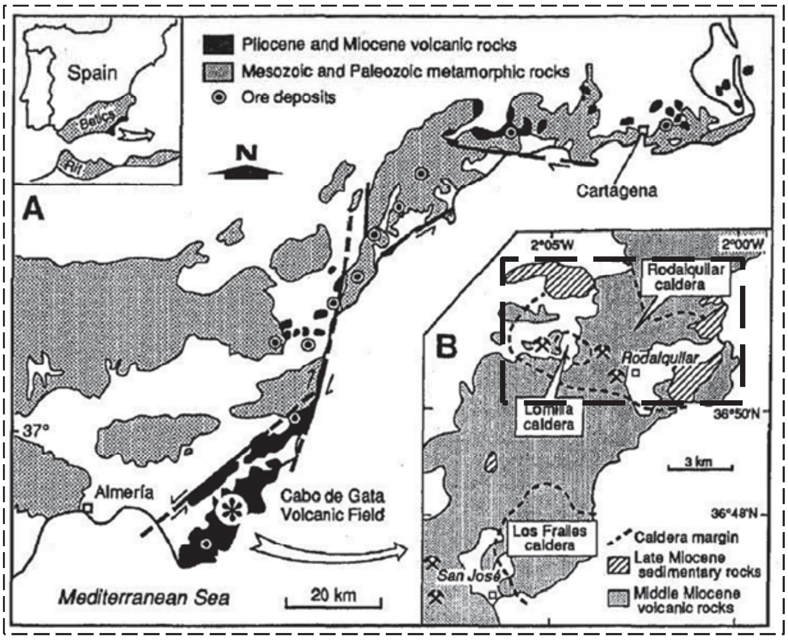

Figure 2-1: (A). Location of the Rodalquilar gold alunite deposit within the Cabo de Gata volcanic field, (inset), southeastern Spain. (B) Index map of the central part of the Cabo de Gata volcanic field. After Arribas et al. (1995). Black-dashed square outlines the research study area

2.2. Evolution

The Rodalquilar caldera complex consists of two nested calderas being the Rodalquilar caldera the biggest one; this hosts in turn the second smaller Lomilla caldera in its central part (Rytuba et al., 1990) (Figure 2-2). The processes that led to the formation of this complex can be divided into three phases. The first phase was the emplacement of dacitic domes and the eruption of the Cinto ignimbrites about 11 Ma that resulted in the collapse of the Rodalquilar caldera and the subsequent emplacement of rhyolitic ring domes. In the second phase, the reactivation of the magmatic processes led to the eruption of Las Lázaras ignimbrite and the formation of the Lomilla caldera. Lastly, a new increment in the volcanic activity resulted in the eruption of hornblende andesite flows and caused intense faulting mainly with a N-S trending. This allowed the development of the hydrothermal activity that conducted the mineralization (Rytuba et al., 1990; Arribas, 1993; Arribas et al., 1995).

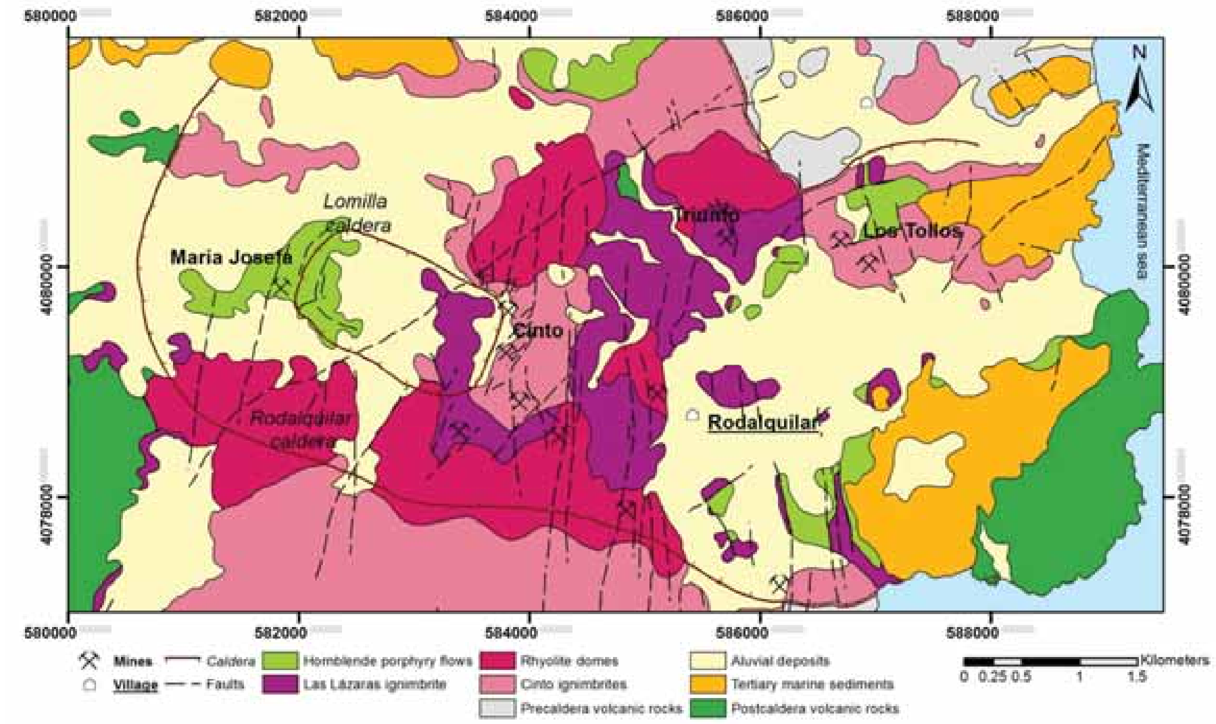

Figure 2-2: Geologic map of the Rodalquilar and Lomilla calderas (modified after Rytuba et al. (1990) and Arribas (1993))

2.3. Mineralization model

The ore deposits in the Rodalquilar caldera complex are mainly alunite, gold – alunite of high-sulfidation origin, and lead – zinc- silver – gold of low-sulfidation origin, of which the gold – alunite mineralization has been the most important economically. These deposits were formed 9 Ma ago near the surface. An intruding andesitic magma provided the heat source for hydrothermal alteration (Arribas et al., 1989), which was influenced by the interaction of two fluids of different origin. The first one was a hypersaline fluid of magmatic origin and the other one a low-salinity fluid derived from the seawater as a consequence of the marine transgressions that took place at that time (Saenger-van Oepen et al., 1989). The subsequent wall rock alteration of the formed epithermal system is characterized by mineral zonation from vuggy silica to advanced argillic, argillic and propyllitic (Figure 2-3) (Arribas et al., 1995), being the advanced argillic zone the host of the highest grade gold mineralization in the eastern part of the Lomilla caldera (Arribas et al., 1989). An intense acid sulphate supergene alteration took place in the epithermal system 7 Ma ago, causing remobilization of primary gold ores and modifying the original mineral paragenesis and the surface expression of the system (Saenger-van Oepen et al., 1989; Arribas et al., 1995).

Historically, Cinto mine in the eastern flank of the Lomilla caldera was exploited for high-grade gold, whereas María Josefa, Las Niñas and Triunfo mines, in the west, south and northern flanks of the Rodalquilar caldera respectively, were exploited for lead, silver, zinc and low-grade gold. Los Tollos mines are metal barren, but they have been exploited for alunite of supergene origin (Arribas et al., 1995; Hernández Ortiz, 2002).

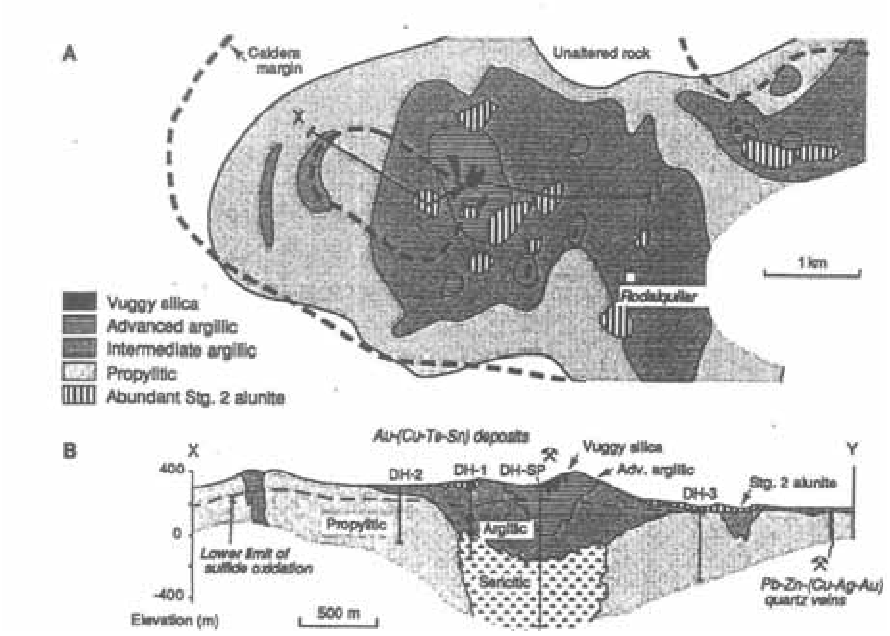

Figure 2-3: Schematic surface alteration map (A) and cross section (B) of the Rodalquilar and the Lomilla calderas. After Arribas et al. (1995). The boundaries among alteration zones are irregular and gradational.

2.4. Spectroscopy studies

Due to its good exposure and documentation, the Rodalquilar caldera complex has been subject of different studies that evaluates the use of spectroscopy as technique to characterize epithermal deposits. These studies have mainly improved. the delineation of the alteration minerals previously defined by Arribas et al. (1995), in which in fact Landsat-5 imagery was used as complementary tool. Ferrier and Wadge (1996) tested different methods for retrieving apparent surface reflectance succeeding in the identification of alunite alteration using Airborne Visible/Infrared Imaging Spectrometer (AVIRIS) data. Afterwards, Bedini et al. (2009) applied the Multiple End-member Mixture Analysis (MESMA) technique to analyse the short-wave infrared (SWIR) spectra over a HyMap scene in order to map the surface distribution of hydrothermal alteration minerals such as alunite, kaolinite, smectite-illite and pyrophyllite.

3. MINERAL SPECTROSCOPY AND CRYSTALLINITY IN EPITHERMAL SYSTEMS

3.1. Alteration in epithermal systems

Epithermal systems have been generally defined as those formed at shallow depths (<1-1.5 km), low pressures (<500 bar), low to moderate temperatures (50-300ºC) and mainly meteoric hydrothermal fluids, but also magmatic in smaller proportion. Based on the pH conditions and the salinity of these fluids, different mineral assemblages as well as the ore elements that are produced, leading to the classification of epithermal systems into two distinctly chemical environments known as Low-Sulfidation and High-Sulfidation (Hedenquist et al., 2000; Pirajno, 2008 and referred works).

The thermal gradient in epithermal systems is a function of pressure, which in turn is dependent on the salinity and gas content in the hydrothermal fluid. Loss of gasses such as CO_2 and H_2S leads to more saline and hence acidic pH, resulting in increasing of the hydrodynamic pressure and therefore the isotherms are moved towards shallower depths. Conversely, fluids that are gas rich and neutral pH place the isotherms at greater depths. Typically, these later fluids are product of mixing of hydrothermal and shallow waters in the margins of the system (Hedenquist and Henley, 1985; Hedenquist et al., 2000).

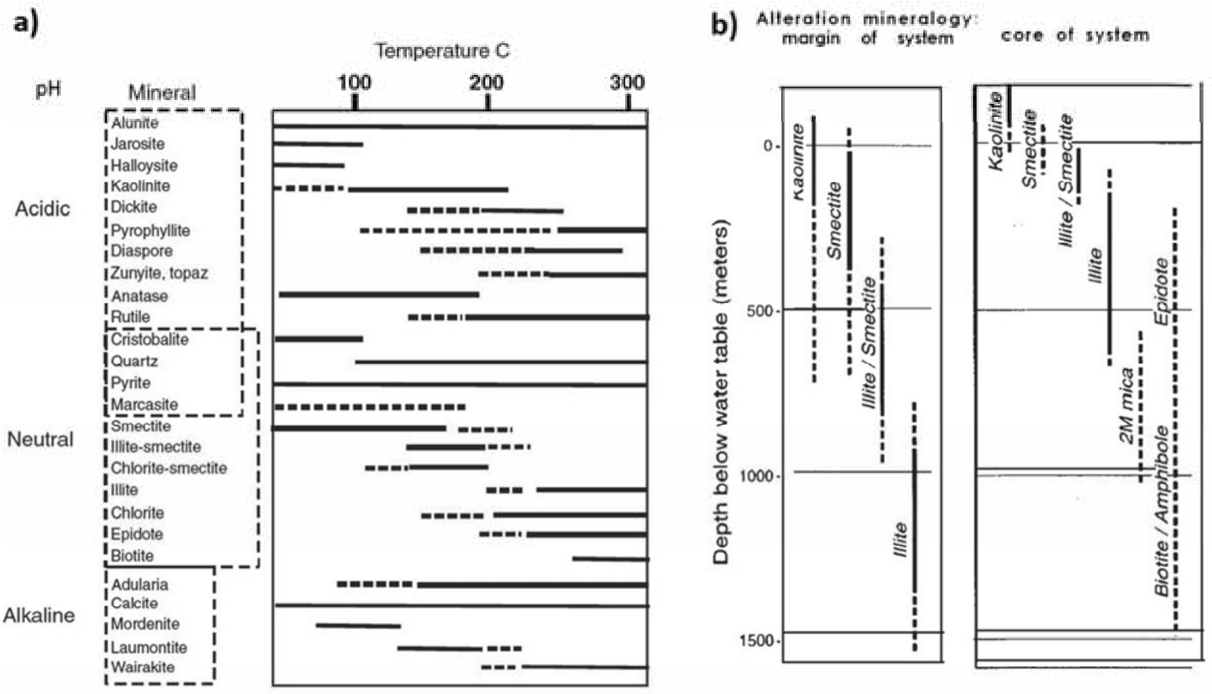

Figure 3-1: a) Temperature and pH range of hydrothermal mineral phases in epithermal systems. After Hedenquist et al. (2000). According to Reyes (1990) illite is also present in acidic pH environments associated with pyrophyllite. b) Schematic depth distribution of some temperature dependent alteration minerals in the margin of the system (low pressure) and in the core of the system (high pressure). Modified after Hedenquist et al. (2000).

Minerals that are highly sensitive of temperature changes, such as kaolins, smectites or illites, can be restricted to characteristic temperature ranges (Figure 3-1a) and might reflect the distribution of the isotherms when these are changing in depth regarding the pressure of the system, as is shown in Figure 3-1b. In addition, These facts make alteration mineral assemblages useful tools as geobaromethers, depth estimators and indicator of chemical conditions of the hydrothermal fluids (Reyes, 1990; Hedenquist et al., 2000).

3.2. Spectroscopy and spectral detectable mineralogy

The study of hydrothermal alteration associated with ore deposits is the beginning to understand the genetic history and events that have affected a mineralized system. The chemical reactions and metasomatic processes that take place in the interaction between host rocks and hydrothermal fluids, and the newly formed mineral assemblages that define the type of alteration, allow the estimation of the physical and chemical environment of formation as well as the spatio-temporal changes in the genetic conditions of the system (Meyer and Hemley, 1967; Pirajno, 1992). The characteristics of the hydrothermal alteration zones in low and high sulfidation epithermal systems have been broadly documented in numerous publications (Henley, 1985; Arribas, 1995; Hedenquist et al., 2000; Corbett, 2002; Sillitoe and Hedenquist, 2003). These studies highlight the importance of smectite, illite, kaolinite, pyrophyllite, alunite and quartz as the principal alteration minerals that define hydrothermal halos or zones, and pinpoint to their potential as indicators of mineralization of economic significance.

Many of the hydrothermal alteration minerals can be analysed by using infrared spectroscopy, since they present characteristic spectral properties. Transitional metals are responsible of electronic processes that generate absorptions in the visible-near infrared (VNIR) between 0.3-1.0 µm, meanwhile water and OH molecules produce vibrational processes that cause energy absorption in the short-wave infrared (SWIR) between 1.0-2.5µm. (Serratosa and Bradley, 1958; Tuddenham and Lyon, 1960; Stubican and Roy, 1961; Hunt, 1977). Particularly, absorption features in the SWIR spectral region have a remarkable importance in mineral exploration since they permit the determination of hydrothermal alteration mineralogy and can assist in the identification of phyllosilicates, clays, carbonates and some sulphates, especially when looking at the features near 2.2µm (Hunt and Ashley, 1979; Thompson et al., 1999). These studies support the role of spectroscopy as a tool for field mineral mapping and ore exploration.

Spectral detectable SWIR mineralogy in epithermal systems

Spectral variations, such as shifts in the wavelength position of the absorption features or changes in the hull shape, have demonstrated the sensitivity of the SWIR to variations in chemical composition and crystallinity degree of the hydrothermal alteration minerals (Hunt and Ashley, 1979; Thompson et al., 1999). Presence of water and hydroxyl in the mineral composition play a particular role in the generation of fundamental vibrations in the TIR and their most common known overtones in the SWIR. Absorption features at 1.4 µm and 1.9 µm are diagnostic of water bearing minerals, and features at 2.2 µm and 2.3 µm are diagnostic of Al-OH and (Fe, Mg)-OH bonds, respectively (Clark et al., 1990).

Those spectral patterns that describe SWIR active minerals can be used for identifying mineral assemblages which are typical of zonation in epithermal systems. Pontual et al. (1997) and Thompson et al. (1999) have summarized the distinctive assemblages of different alteration zones for high sulphidation as well as low sulphidation systems (Table 3-1). Depending on the mineralogical group they belong to, specific spectral features are used for mineral description and identification (Pontual et al., 1997), as is explained below.

Table 3-1: Summary of Infrared-active minerals, with distinctive spectra in the SWIR for epithermal systems (modified after Thompson et al. (1999))

Environment of formation	Standard terminology for alteration zones	SWIR active mineral assemblage
High sulfidation	Advanced argillic – acid sulphate	Kaolinite, dickite, alunite, pyrophyllite, illite, zunyite
	Argillic, intermediate argillic	Kaolinite, dickite, montmorillonite, illite-smectite
	Propylitic	Calcite, chlorite, epidote, sericite, clay
Low sulfidation	"Adularia" – sericite, sericitic, argillic	Sericite, illite-smectite, kaolinite, chalcedony, opal, montmorillonite, calcite, dolomite
	Advanced argillic – acid-sulphate (steam-heated)	Kaolinite, alunite, cristobalite (opal, chalcedony), Jarosite
	Propylitic, zeolitic	Calcite, epidote, chlorite, illite-smectite, montmorillonite

Smectite and Mica (illite-muscovite) groups

- Montmorillonite $(\frac{1}{2}Ca,Na)_{0.7}(Al,MgFe)_4[(Si,Al)_8O_{20}](OH)_4\cdot nH_2O)$
- Illite $((Ca_{0.05}Na_{0.03}K_{0.61})(Al_{1.53}Fe^{+3}{}_{0.22}Fe^{+2}{}_{0.03}Mg_{0.28})(Si_{3.4}Al_{0.6})O_{10}(OH)_2)$
- Muscovite $(K_2Al_4[Si_6Al_2O_{20}](OH,F)_4)$

The most distinctive features that characterize the minerals in the smectite group, as montmorillonite, and mica group, as illite and muscovite, are due to the vibrations of the H_2O molecules and OH^- ion. Firstly, depth of the absorption feature at 1400 nm and 1900 nm is indicative of the water content and its location in the mineral structure; in this sense, smectites that bear high quantities of water show deeper and broader water features than illite and muscovite, in which these features are almost inexistent at 1900 nm and narrower at 1400 nm (Hauff et al., 1991; Kruse and Hauff, 1991; Post and Noble, 1993). Secondly, ion substitutions as the Tschermak cation exchange that involves Mg, Fe and Al, modify features related with OH-cation bend in the 2000-2500 nm range. The most prominent feature is at 2200 nm regarding the variation in Al content, whereas secondary features located between 2350-2450 nm and related with the Fe and Mg substitution (Clark et al., 1990; Duke, 1994). The typical spectral profiles of montmorillonite, illite, sericite and muscovite are shown in the Figure 3-2a.

Kaolin group

- Kaolinite $Al_4[Si_4O_{10}](OH)_8$
- Halloysite $Al_4Si_4(OH)_8O_{10}\cdot 8H_2O$
- Dickite $Al_4[Si_4O_{10}](OH)_8$

As other clay minerals, the characteristic absorptions of minerals in the kaolin group are controlled by the hydroxyl-stretching bands near 1400nm and 2200 nm. The location of the hydroxyl in the mineral structure produces changes in its vibration energy, which is reflected in the development of doublets in the hydroxyl features, being weak in the poorly crystalline halloysite and becoming better defined throughout kaolinite to dickite (Brindley et al., 1986). The presence of molecular water specially on halloysite and poorly crystalline kaolinite is reflected on the presence of the 1900 nm feature (Crowley and Vergo, 1988). Figure 3-2b displays examples of spectral profiles for dickite, kaolinite and halloysite.

Pyrophyllite

- Pyrophyllite $Al_4[Si_8O_{20}](OH)_4$

In the SWIR, pyrophyllite has very unique features that ease its differentiation from other minerals. Representative single sharp absorptions of this mineral are located at 1396 regarding the H_2O and OH content, and at 2166 nm regarding Al-OH bond. Other characteristic absorptions are a not well resolved shoulder at 2066-2078 nm and secondary features at 2319 nm, that remain present even in mixtures (Clark et al., 1990; Pontual et al., 1997). Diagnostic features of pyrophyllite can be seen in Figure 3-2c.

Zunyite

- Zunyite $Al_{13}Si_5O_{20}(OH,F)_{18}Cl$

This mineral has a singular crystal structure that generates unique diagnostic features, allowing its clear identification. The most prominent absorption located at 2135 nm is produced by the Al-OH vibrations and OH stretching. In the 1400 nm region, two strong absorptions at 1410 and 1475 nm are associated with OH stretching and hydrogen-bonded OH groups, respectively (Crowley, 1984). The particular absorptions of zunyite are in Figure 3-2d.

Carbonate group

Calcite	$CaCO_3$
Dolomite	$CaMg(CO_3)$
Siderite	$FeCO_3$

Unlike phyllosilicates, the distinguishing features in carbonates are due to the CO_3 ion. Overtones of the fundamental vibrations in the IR occur near 2500-2550 nm and 2300-2350 nm. Other weaker bands are located at 2120-2160 nm, 1970-2000 nm and 1850-1870 nm (Clark et al., 1990). Figure 3-2e shows typical spectral profile of dolomite, calcite and siderite carbonates.

Sulphate group

Alunite	$(K,Na,NH_4)Al_3(SO_4)_2(OH)_6$
Jarosite	$KFe_3(SO_4)_2(OH)_6$
Gypsum	$CaSO_4 \cdot 2H_2O$

Sulphate bearing minerals are characterized by the: broad features at 1400 nm due to water content and OH-stretch overtones; the shape of the feature is characteristic of each specimen. Another characteristic sulphate absorption which varies among 1700 or 1800 nm is OH related. The spectral region 1900-2500 nm is quite different for each mineral. In the case of alunite, a broad feature with doublet is present due to the OH-stretch and Al-OH bend and varies in position depending on mineral composition (Na, K or NH_4), whereas in jarosite the feature occurs at longer wavelengths and is related with the Fe-OH bend. Gypsum does not really have clear absorptions in this region (Clark et al., 1990; Pontual et al., 1997). The spectral features of the most common sulphates alunite, jarosite and gypsum are shown in Figure 3-2f.

3.3. Importance of mineral crystallinity in epithermal systems

Although the terms illite crystallinity and kaolinite crystallinity have been widely used, they have been questioned due to the imprecise definition and dependence on the measuring technique (Guggenheim et al., 2002). Because of its common use as referring to the "degree of ordering" in the crystal structure for phyllosilicates, herein it is used in that sense.

3.3.1. *Crystallinity* in the Smectite – Illite-Muscovite group

From smectites to micas, both dioctahedral 2:1 layer silicates, a genetic mineralogical sequence can be described, going from the hydrated montmorillonite smectite specie, throughout the illite series (interlayer deficient micas) until muscovite (true mica) (Rieder et al., 1998). Changes in formation conditions cause gradual variations in the arrangement of the crystal structure and composition, generating different mineral specimens or polymorphs of a single mineral (Yoder and Eugster, 1955). Regarding smectites and micas, the increasing pressure and temperature result in a succession from the smectite species montmorillonite, throughout mixed layered montmorillonite/illite with dominant montmorillonite, montmorillonite/illite with dominant illite, illite and finally muscovite (Velde, 1977). Transition from montmorillonite to muscovite throughout an illite mixed layer phase begins with the loss of structural water and replacement of Ca^{2+}by K^{+} in the interlayer spaces of montmorillonite. The subsequent development of the illite mixed layer phase involves a gradual ordering in the crystal structure, generating different illite polymorphs, since the disordered 1M$_{d}$ type until the very well ordered 2M variety (Duba and Williams-Jones, 1983). Later, in the more crystalline illite phases and muscovite the octahedral-tetrahedral Tschermak exchange produces enrichment in Al, while there is a decrease in Si, Fe and Mg, bringing about a more homogeneous or crystalline structure (Duke, 1994).

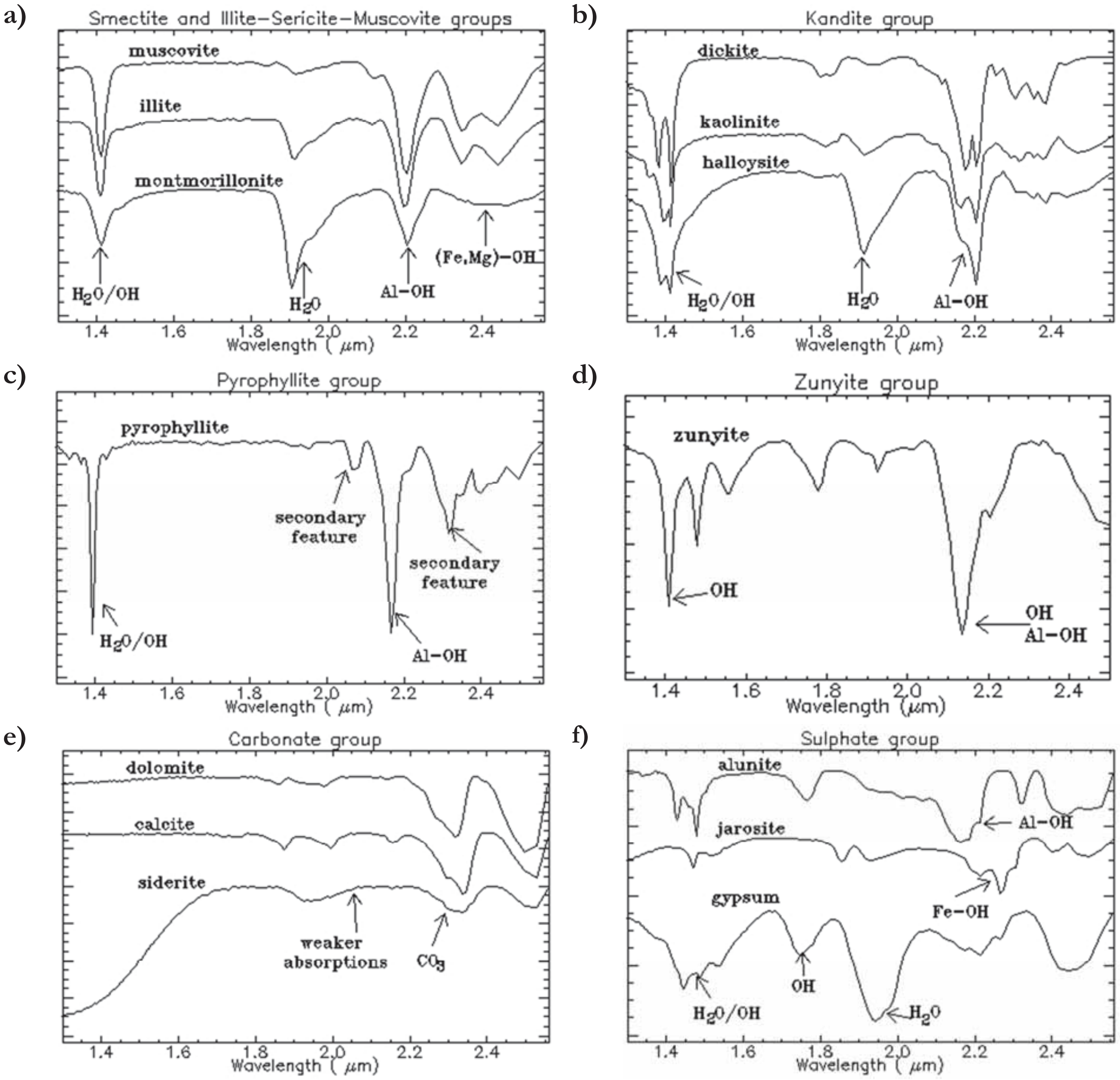

Figure 3-2: Distinctive spectral features of the main SWIR active mineral groups: a) illite-sericite-muscovite group, b)kaolin group, c) pyrophyllite group, d) zunyite, e)carbonate group, f) sulphate group. Spectral profiles from USGS spectral library (Clark et al., 2007). Values in vertical axis are offset for clarity.

Different mineral analytical techniques commonly use the term *illite crystallinity* as a measure of the structural ordering of illites. Despite this, the ambiguous definition of illite in old literature and the mixed-layered nature of smectite and illite, the term might be used for description of the crystal structure from montmorillonite to well-ordered illite (Kubler and Jaboyedoff, 2000). Probably the most used technique for detection of *crystallinity* changes is X-ray diffraction (XRD) which measures interlayer space, although this is highly dependent on the size of the measured particles. However, Kruse and Hauff (1991) have indicated that SWIR spectrometry is even a more successful technique in measuring the structural ordering of illite. This method uses the depth of absorptions related with Al-OH bonds and OH-stretch and H_2O content as measurement of the *crystallinity* degree in the crystal lattice.

The increasing structural ordering in this mineralogical sequence has been widely used for describing temperatures in different diagenetic stages, late phases of metamorphism and hydrothermal environments. Conversion from smectite to mica in hydrothermal systems has been reported as a very low temperature sequence on geothermal fields, being the conversion from montmorillonite to illite at approximately 100-130°C and from illite to muscovite at 210-230°C (Steiner, 1968; Muffler and White, 1969). These gradual variations are commonly associated to epithermal gold mineralization, where the montmorillonite-illite-muscovite sequence is present lateral and vertically throughout most of the alteration zones (Table 3-1), acting as indicator of temperatures of ore formation and proximity to the hydrothermal fluids (Hauff et al., 1989).

3.3.2. *Crystallinity* in the Kaolin group

Kaolinite, together with dickite and halloysite are polytypes of the kaolin group, previously known as kandite group (Guggenheim et al., 1997), which are characteristically dioctahedral 1:1 layer silicates. Dickite is typically a product of high temperatures in hydrothermal environments, whereas kaolinite and halloysite might be either from hydrothermal or weathering origin. The differences that lead to different grades of order in the crystal lattice are due to the location of the vacant octahedral sites those are occupied by cations. That results in a very well-ordered cell in dickite and well-ordered cell in kaolinite. Hosting of structural water in halloysite increases the interlayer spacing and as a consequence a less ordered structure.

In epithermal environments, the variation among kaolins is caused by the interaction of the host rock and acid fluids, that leads with the removal of cations such as Ca, Na or Mg and the fixation of Al and Si (Pontual et al., 1997). At temperatures above 200°C, well-ordered dickite structures are formed; later, decrease of temperature (200-120°C) leads to simultaneous formation of disordered dickite to ordered kaolinite (Brindley et al., 1986; Reyes, 1990). As a final stage, up to surface conditions, water is incorporated to the crystal structure resulting in the less ordered halloysite. Later degradation to weathering environment generates distortion in kaolinite the crystal lattice, sometimes related with Fe enrichment and Al depletion (Brindley et al., 1986). The position in the weathering profile, regarding the water activity, leads with the formation of the water saturated halloysite as alteration product from alumino-silicate minerals (Pontual et al., 1997).

Kaolin polytypes have been used as geothermometers in geothermal systems (Reyes, 1990) and for distinguishing among hydrothermal and weathering environments (Brathwaite et al., 2012). Despite that many of these studies have analysed the structural changes with different analytical techniques with X-ray diffraction as the most common one, IR spectroscopy has proven to be very precise, since it is not dependent on the size or orientation of the measured particles. The development of hydroxyl-stretch bands and their wavelength positions can be used to measure the *crystallinity* degree of kaolinite and dickite (Crowley and Vergo, 1988). Even though in halloysite this feature is also present, the occurrence of molecular water is a more distinctive characteristic for its identification.

4. METHODOLOGY

Identifying SWIR active minerals and assemblages as well as the *crystallinity* variations of smectite-illite-muscovite and kaolin groups, required the integration of different methods for both data, proximal and remotely sensed. The primary sources of information were ground spectroscopic measurements in the SWIR range, taken either in the field or in the laboratory. The data was retrieved at continuous and high spectral resolution that led to the identification of most of the features that spectrally characterize the surveyed minerals. For validating as well as complementing and supporting the obtained results, analysis with X-ray diffraction (XRD) and Thermal Gravimetric Analysis (TGA) techniques were conducted in order to compare the identified mineralogy aside from the *crystallinity* degree based on different parameters for each technique. Finally, the derived spectral parameters from the ground data analysis were extrapolated to a HyMap scene that covers the whole study area. This was done in order to obtain a complete overview of not only the spatial distribution of the alteration mineralogy, but also the distribution *crystallinity* variations of the studied minerals, allowing the mapping and interpretation of the these variations in the Rodalquilar deposit. Figure 4-1: Diagram describing the methodology followed in this research

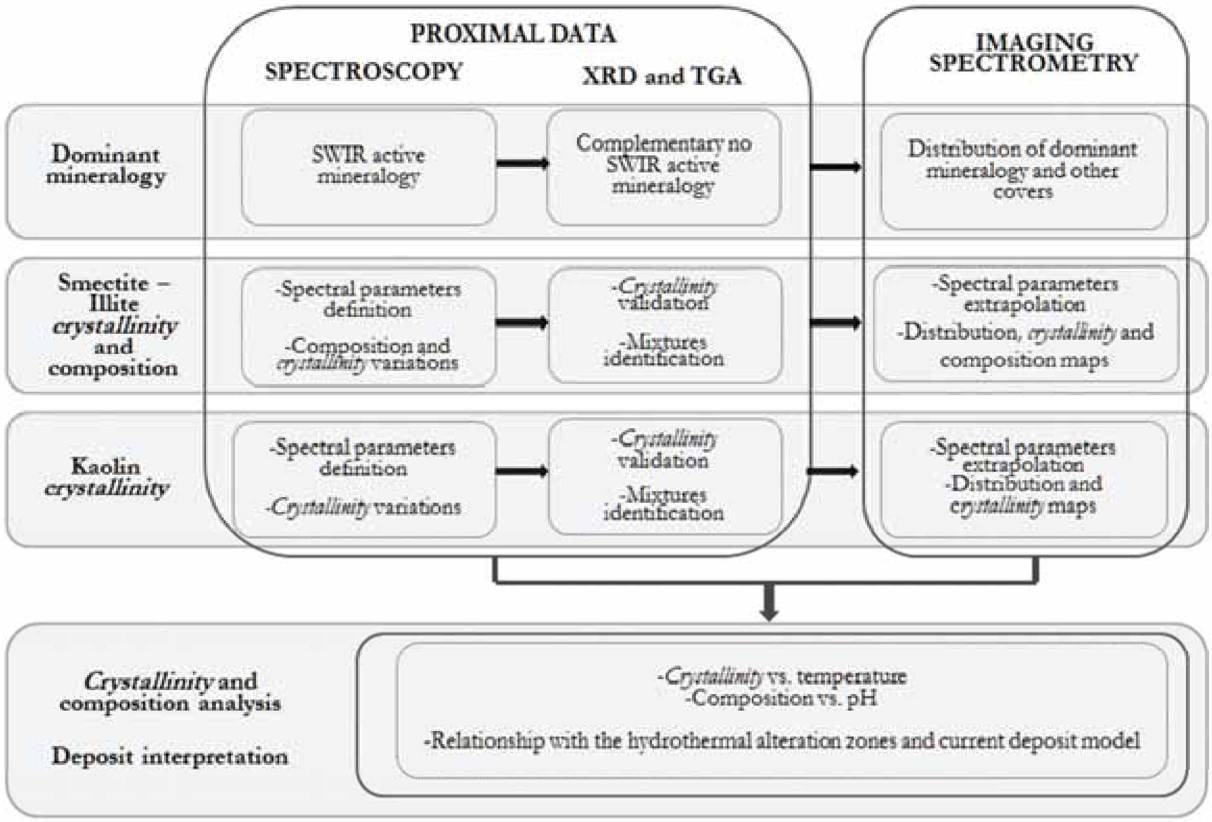

Figure 4-1: Diagram describing the methodology followed in this research

4.1. Ground and laboratory spectroscopy

4.1.1. Dataset and instruments

For this research ground spectra and rock samples collected in the Rodalquilar area by ITC staff and students from 2003 to 2006 in campaigns with different purposes are the main source of spectral information. The location of the sampling points is shown in Figure 4-2 and detailed tables with the specific coordinates and spectral files are available in Appendix 1.

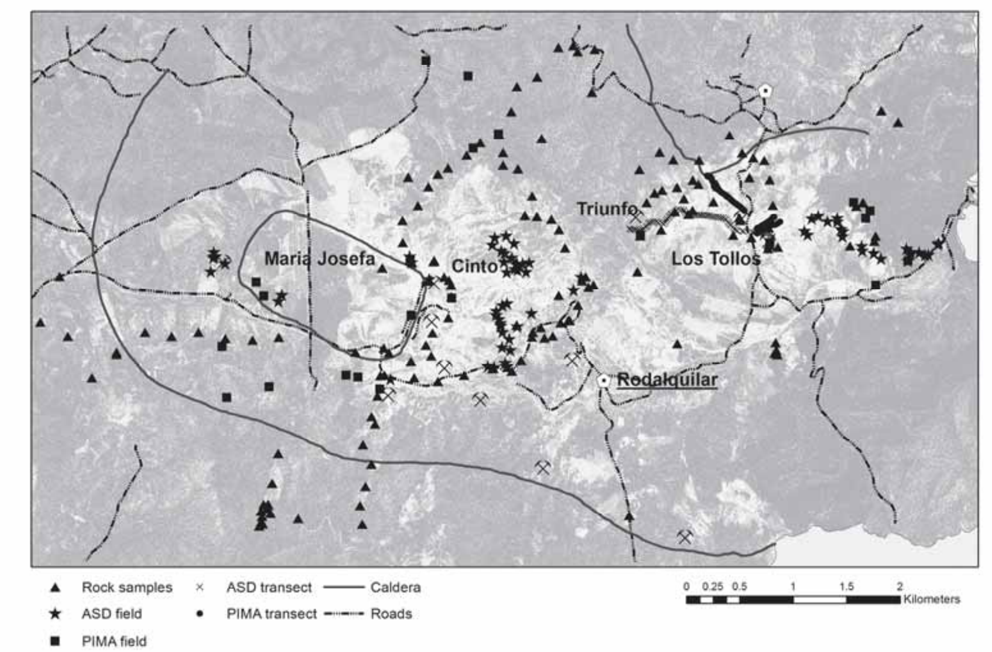

Figure 4-2: Location of rock samples and ground spectra collected on previous field campaigns. Background image: HyMap wavelength indicating the presence of minerals with strong Al-OH absorption (light colour), delineating the areas with intense hydrothermal alteration.

Ground spectra datasets were acquired in the past using Portable Infrared Mineral Analyser (PIMA) II and Analytical Spectral Device (ASD) FieldSpec spectrometers with the pistol grip or contact probe devices, while laboratory data were collected for this research using ASD FieldSpec with the contact probe. The detailed specifications of these instruments are summarized in Table 4-1.

For ease and accuracy in the spectral analysis, the dataset was subdivided based on the nature of the sampling method (transect or individual locations) and the instrument used for measurement. One part of the dataset consists of spectral measurements along four transect lines in Los Tollos area. The first transect is located between Los Tollos and Triunfo mines; it was measured by using the ASD spectrometer with the pistol grip and the sun as light source, generating a noisy spectra with the atmospheric absorption interference. The other three transects located north-eastward Los Tollos mine were measured using PIMA spectrometer and are relatively noisy. The second part of the dataset includes ground spectra measurements taken in different parts of the Rodalquilar caldera mostly with the ASD using the contact probe, giving a full range and good quality spectra. Other few measurements were taken with PIMA and their quality is similar to the PIMA transect. Finally, 211 altered and unaltered rock samples collected in different locations along the area of study were available for ASD laboratory spectra.

Table 4-1: Instrument specifications for PIMA II and ASD FieldSpec spectrometers

Characteristics	PIMA II	ASD FieldSpec
Spectral range	1300-2500 nm	350-2500 nm
Spectral resolution	7 nm	3 nm at 700 nm 10 nm at 1400-2100 nm
Sampling interval	2 nm	1.4 nm VNIR 2 nm SWIR
Light source	Internal lamp	Sunlight (pistol grip) Internal lamp (contact probe)

4.1.2. Processing and interpretation of SWIR reflectance spectra

Active SWIR minerals can often be identified because of their absorption features in the 2200 nm region as a consequence of the vibrational processes due to the Al-OH molecular bonds. The wavelength position and the shape of this feature permit the identification of different mineral groups. The Al-OH parameter together with other absorption features generated by, for instance, the presence of water, ions or other molecules in the mineral structure, are the base for mineral identification.

Besides the ground spectra, laboratory measurements were made for the 211 rock samples using the ASD spectrometer. For each sample, three different measurements were taken using the contact probe device, regular re-calibration of the spectrometer was made with the dark current and white reference in order to preserve the quality of the measurements. The raw data was processed using the ViewSpec software for splice correction and conversion to suitable formats for The Spectral Geologist (TSG), ENVI and Hyperspectral Python (HypPy) software[1]. TSG software was used to obtain a first interpretation of the spectral mineralogy and for the extraction of the spectral parameters. ASCII converted files allowed the creation of spectral libraries in ENVI for comparing the collected spectra with the USGS reference and with the HyMap image. The same processing procedure was followed for the raw files of the ground spectra. Due to the atmospheric interference that masks some of the relevant absorptions, the ASD transect dataset was set aside in this part of the analysis.

The dominant infrared active mineralogy in the spectra was interpreted at first by using The Spectral Assistant (TSA) algorithm of the TSG software. The TSA enabled also the extraction of spectral features, as well as the indices calculation and the grouping of minerals according the pure or mixed spectra, easing the subsequent analysis.

Spectral features that are relevant for hydrothermal mineral identification in the SWIR were extracted from the continuum removed spectra. Depth and wavelength position of the deepest absorption features related with bending and stretching in hydroxyl (OH), water and carbonate (CO_3), and vibrations between AlOH, FeOH and MgOH were used (Figure 4-3). For water at 1400 nm absorption the asymmetry was also considered, besides the ratio of the depth of AlOH and water at 1900 nm features as relative measure of water content. The summary of the used absorption parameters is listed below.

Depth of the 1400 nm (water, OH) absorption feature	*1400D*
Wavelength position of the 1400 nm (water, OH) absorption feature	*1400W*
Asymmetry of the 1400 nm (water, OH) absorption feature	*1400AS*

---

[1] HypPy is a freeware software developed by Wim Bakker from the ITC Faculty – University of Twente. The syntax of the used formulas for the extraction of spectral parameters is given in Appendix 2

• Depth of the 1900 nm (water) absorption feature	*1900D*
• Depth of the 2200 nm (AlOH) absorption feature	*2200D*
• Wavelength position of the 2200 nm (Al OH) absorption feature	*2220W*
• Asymmetry of the 2200 nm (AlOH) absorption feature	*2200AS*
• Wavelength position of the deepest absorption feature in the 2100-2500 nm range	*2100-2500W*

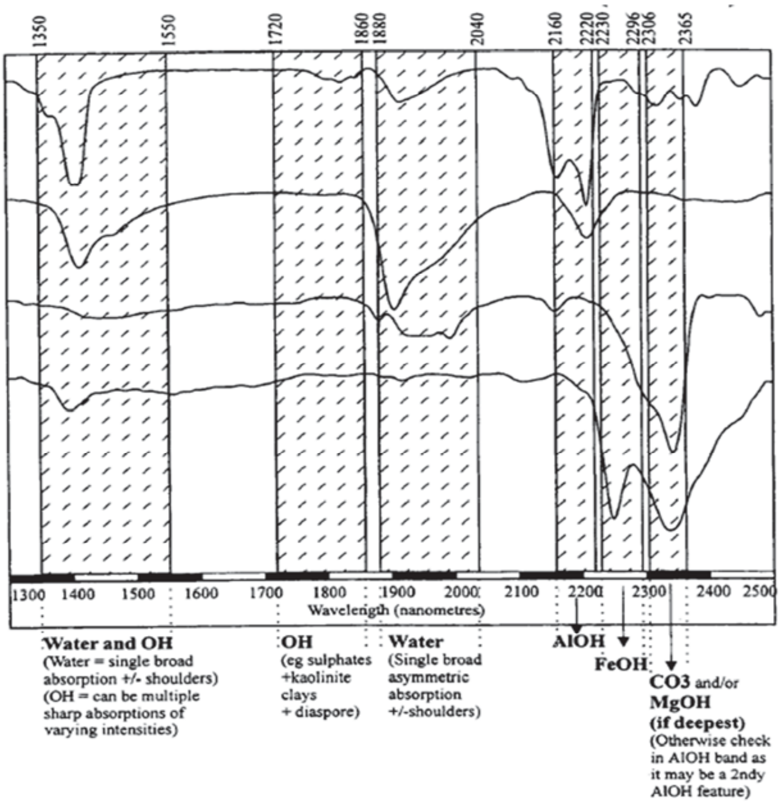

Figure 4-3: Spectral parameters for SWIR active mineralogy identification. After from Pontual et al. (1997).

Identification of spectral groups and the mineral subsequent end-member selection was mainly based on plots that relate the *2100-2500W* and relative water content (*2200D/1900D*) parameters. Besides, other specific diagnostic features, such as doublets, were also taken into account for mineral identification. Finally, samples in the 2175-2220 spectral group, which belong mostly to the kaolin, illite-muscovite and smectite groups, were subject of more detailed observations regarding *crystallinity* analysis. These later analysis were conducted using HypPy software in order to ease the extrapolation of the analysed features from laboratory to remotely sensed data. At this stage, datasets from different sources did not present significant differences; hence onwards they were treated as a single dataset.

***Crystallinity* in the Smectite – Illite-Muscovite group**

The *2200D/1900D* parameter is widely considered as a *crystallinity* parameter in illites, and hence here is also considered as the main *crystallinity* indicator for the smectite – illite-muscovite group. The relationship of this parameter with *2200AS* and *1400AS* was measured for exploring changes in *crystallinity*. Besides, secondary features between 2300-2500 nm were also used as an indicator of degree of structural order. Finally, the *2200D/1900D* ratio was related with the *2200W* parameter, which is considered as an indicator of aluminium content (Duke, 1994; van Ruitenbeek et al., 2005); shorter wavelengths are close related with aluminium-rich minerals, which in turn have a well ordered lattice structure, hence it is expected that very well ordered illites have short wavelength in the 2200 nm absorption and therefore, they are aluminium-rich. Based on these parameters, end-members were selected and a *crystallinity* classification was conducted and used for mapping the distribution of the smectite to illite-muscovite *crystallinity* changes in the study area. Due to the results obtained of these analyses, it was decided to simplify the name of the group just as "smectite-illite". The extracted absorption parameters for crystallinity analysis are given in Appendix 3.

Crystallinity in the Kaolin group

The most relevant feature that points out the degree of crystallinity in the kaolin group is the doublet in the AlOH absorption. For its measurement, the slope parameter (2160D/2177D and 2184D/2190D ratios) and the Kaolinite *crystallinity* index *KX* (Equation 4-1) were calculated. Aiming to avoid misinterpretation related with mixtures, the 2200D/1900D parameter as well as the 1400as, 1400w doublets in the 1400 nm feature were interpreted. Based on these parameters, end-members for dickite, kaolinite and halloysite were selected, and, likewise the smectite – illite-muscovite group, the *crystallinity* variations were determined. The extracted absorption parameters for crystallinity analysis are given in Appendix 4.

$$KX = (R2160/R2177) - ((R2184/R2190) - (R2160/R2177)) \qquad \text{Equation 4-1}^{2}$$

4.2. X-ray diffraction and Thermogravimetric analyses

In order to corroborate as well as to clarify and expand the interpretation of the SWIR reflectance spectra, complementary analyses for the identification of mineralogy and assessment of the *crystallinity* degree were conducted. X-ray diffraction (XRD) and Thermogravimetric Analysis (TGA) were chosen not only due to their ability on identifying the mineralogy previously analysed, but also because they allow different approaches for *crystallinity* measurement.

Twenty representative rock samples from the most relevant mineral groups analysed with SWIR spectroscopy were selected based on different criteria. Samples from smectite – illite and kaolin groups were selected mostly to study the gradational changes in structural order as well as to identify mineral mixtures. From the smectite-illite group 9 samples with different degree of structural order, based on the SWIR *crystallinity* classification, were selected; in the kaolin group 8 samples that comprise the dickite, halloysite and kaolinite end-members besides samples representing intermediate phases and mixtures were also chosen. Furthermore, the sample selection included end-members of K and Na alunite, as well as zunyite. Description of the samples is given in Appendix 5.

The sample preparation consisted first on rock powdering and sieving in order to get homogeneous fractions and to reduce the high amount of quartz that could interfere in the analyses; then they were re-measured with the ASD spectrometer with the purpose of being able to make a direct comparison between the three analytical techniques. After that, XRD measurements were conducted and finally, based on these results, a subset of samples was selected for TGA analysis.

4.2.1. X-ray diffraction

Although X-ray diffraction is highly sensitive to the size and orientation of the measured particles, it has been the most common technique for measuring unit-cell parameters of mineral crystal structure, such as thickness and lattice strain. Typically XRD has been used along with SWIR spectroscopy in illite *crystallinity* studies, for instance in the identification of polytypes (Hauff et al., 1991) or measuring the well-known Kübler index. Similarly, Hinckley index (Hinckley, 1963) has been used for analysing XRD patterns related with the order in crystal structure in kaolin.

---

[2] R#### makes reference to the reflectance at the given #### wavelength

In this research XRD analysis were mainly based on the position of the first basal reflection of the studied minerals located between 5-15°2θ (~15-7 Å), supported by other diagnostic peaks between 17-19°2θ and 23-35°2θ. Even though peaks at 21°2θ and 26°2θ can be diagnostic of some of the studied minerals, they were not taken into account, since they are characteristic of quartz-rich acidic rocks. Even though there are sample preparation methods that reduce the influence of particle orientation, in this research simple analysis on air-dried samples were performed. Measurements were carried out on a Bruker D2 Phaser XRD diffractometer (CuKα radiation, Lynxeye detector), from 5 to 70°2θ. Analysis of the measured samples was conducted using the software XRDCalc V5.1, and results were compared with the American Mineralogist crystal structure database (Downs and Hall-Wallace, 2003). Results of the XRD analysis are given in Appendix 6 and Appendix 7.

4.2.2. Thermogravimetric Analysis

Thermogravimetric analysis, thermal gravity analysis or differential thermal analysis (TGA) is a very simple technique that records the endothermic and exothermic effects in certain material when heating a small amount of it up to 1000°C. In mineralogical studies, TGA mostly reflects the water-loss, measured as weight loss, and might be related with the ordering in the lattice structure (Grim and Rowland, 1942).

The position of the first endothermic peak is the most revealing feature in TGA curves; it allows a clear differentiation between the kaolin and smectite-illite groups. Halloysite and kaolinite have a sharp peak at 550-600°C, whereas illite has a broad feature between 500-650°C and montmorillonite at 600-700°C. Given these diagnostic features, a subset of 11 samples was chosen for TGA analysis: 8 kaolin samples for analysing mixtures and support XRD analysis, 1 illite and 1 montmorillonite sample as reference material, and the sample containing zunyite as complement data.

A pilot study on 6 samples for assessing the usefulness of TGA analysis in this dataset was conducted by Hay Berden of Mettler Toledo using a TGA/SDTA 851 Thermogravimetric Analyzer with a large furnace and balance resolution of 0.1 μg; measurements were taken in a temperature range from 30°C to1100°C and heating rate of 5°C /min. The second set of samples was measured in the University of Twente, using similar equipment as described above, in a temperature range from 25 to 1000 °C and a heating rate of 10/min. In both set of measurements the sample size were variable and is given with the data. TGA and derivative TGA curves were compared with the curves presented by Grim and Rowland (1942) and Bish and Duffy (1990). Results of these analyses are given in Appendix 8.

4.3. Imaging spectrometry

The remote sensing analysis was conducted over an atmospherically corrected mosaic of images recorded by the HyMap airborne imaging system on July 11th 2003. A typical HyMap scene consists of 126 spectral bands that cover almost continuously the VIS and SWIR regions from 0.45 to 2.5 μm, with a signal to noise ratio of more than 500:1 (Cocks et al., 1998). The specifications of HyMap scene used in this research are shown in Table 4-2.

4.3.1. Extrapolation of laboratory to airborne spectroscopy

In order to extrapolate the spectral parameters from the continuous and very high resolution lab and field spectra to the atmospherically disturbed and lower resolution airborne spectra, the spectral library of the powdered samples was resampled to the resolution of the HyMap image. For achieving this and IDL-based Gaussian resampling method run in ENVI was used, obtaining a new spectral library with the HyMap spectral resolution. The resampled library was utilized for calibration and estimation of the spectral parameters that should be applied on the image, similarly as is done in Rodger et al. (2012). Once all the parameters were assessed in the resampled library, those that were still considered suitable for analysis were applied to the HyMap scene. Since commonly the wavelength units in the HyMap imagery are expressed as micrometres (μm) instead of nanometres (nm), in this document the resampled spectral library and the HyMap scene units are also expressed in micrometres, but the names of the spectral parameters are kept the same as in the ground and laboratory spectroscopy.

Table 4-2: Specifications of HyMap scene used in this research

Characteristic	Description
Spectral range	0.44 to 1.34 μm 1.40 to 1.8 μm 1.95 to 2.48 μm
Bandwidth	17 nm (0.017 μm)
FWHM	19 nm (0.019 μm)
Pixel size	4 meters

Extrapolation of absorption features from the full resolution library to the resampled one was done mostly for smectite-illite and kaolin parameters, rather than for general mineralogy identification. Depth and wavelength position of the 1400 and 2200 nm features in the HyMap-resampled spectral library were interpolated using the Simple Quadratic Method (SQM) explained by Rodger et al. (2012) which is also used by the HypPy software in the image processing. Aside, because of the absence of some bands for the 1900 nm feature due to the atmospheric interference, a method using the few present bands was developed to extrapolate the $1900D$ parameter (see Appendix 10).

The smectite-illite *crystallinity* was calculated again as the ratio of the interpolated $2200D$ and $1900D$. The kaolin *crystallinity* assessment a different method was required to deal with the low HyMap resolution, which masks the characteristic kaolin doublet at 2164 nm. Equation 2 used by Cudahy et al. (2008), that calculates the depth at 2160 nm as indicator of kaolin crystallinity degree, was solved for the resampled spectral library and compared with the $2160D/2177D$.

$$2160D = (R2138 + R2190)/R2156 \qquad \text{Equation 4-2}$$

4.3.2. Processing and interpretation of HyMap imagery

Identification of dominant hydrothermal mineralogy and identification of crystallinity and compositional changes in the HyMap scene involved several processing steps. Since the HyMap sensor records all the surface materials that are SWIR active, the mineralogical interpretation required first a general identification of the different covers in the area of study. Then, processing and analyses focused on the distribution of the minerals and their relationship with the geological units in the Rodalquilar caldera. Finally, specific procedures were followed leading to crystallinity and compositional analysis of smectite-illite and kaolin groups.

Although the Rodalquilar area is a semi-desert region, there is still presence of vegetation that recorded in the HyMap image might either hinder or interfere with the mineralogical analysis. For this reason, NDVI for detection of green vegetation and the absorption feature of cellulose at 2.090 μm for dry vegetation were calculated. As a result, the abundance and distribution of the vegetation cover was visualized and from this a mask was built in order to be removed the effects of vegetation in the remaining image processing.

Identification of the dominant SWIR active mineralogy in the remotely sensed image was done by detecting the deepest absorption between 2.100 and 2.400 µm. A wavelength map was processed with HypPy software in order to display the identified absorption wavelengths and the distribution of the recognized mineralogy. Such wavelength map displays in a single image the wavelength value as hue and the depth as intensity, easing the visualization of the range of wavelengths present in the hyperspectral image. Alike that in the ground and laboratory data, spectral groups were defined for their detailed analysis and a second wavelength map enhancing the 2.150-2.280 µm range was elaborated. Considering the abundance of sulphates on the surface a third wavelength map for the unique absorption of these minerals at 1.750 µm was processed. Based on that, a sulphate mask was built in order to avoid their interference with the smectite-illite and kaolin analysis.

Distribution, crystallinity and composition of smectite-illite and kaolin groups

Regarding the specific smectite-illite and kaolin groups, processing restricted to the absorptions between 2.170 and 2.225 µm. First of all, the common parameters for both groups were extracted. From the "wavelength of minimum" function of HypPy software, the interpolated wavelength and depth of the deepest absorption feature in the specified range were retrieved, generating in this way the HyMap 2200W and 2200D parameters, whereas water feature or 1900D parameter was calculated similarly to the resampled spectral library explained before. Three filters based on the secondary absorptions of smectite, illite and kaolin between 2.250 and 2.350 µm were applied to the image in order to separate these minerals as is explain by Cudahy et al. (2008).

Spatial distribution, crystallinity and composition of smectite-illite were interpreted from the HyMap image. The distribution of this mineral group in the study area was visualized from the remaining pixels after the kaolin separation, whereas the crystallinity was computed as the 2200D/1900D ratio. For the analysis of compositional variation, a new wavelength map that displays the different values of the 2200W parameter was processed. Respecting the kaolin group, spatial distribution and crystallinity were also interpreted. The spatial distribution was spotted with the pixels present after the smectite-illite separation, and the crystallinity degree by computing Equation 4 2 in the image; the 2200D/1900D ratio was also processed for comparison with the crystallinity index. All the spectral parameters were calculated by using HypPy software and the masks were built and applied in ENVI. For details of the HypPy functions used, see Appendix 2.

At the end, the results were correlated with the outcomes of the ground and laboratory spectroscopy. A spectral library built with 47 samples from the smectite-illite group and 48 from the kaolin group was resampled to HyMap resolution. All the spectral parameters measured in the image were calculated for the resampled library aiming to get estimated values suitable for comparison and correlation. The location of those samples was checked in windows of 3x3 and 5x5 pixels to verify the presence of the minerals in the image. Then, with the pixels that showed a positive match, the image values and the estimated ones from the resampled library were correlated. Finally, maps that display simultaneosly the results of crystalline and compositional variations from both, proximal and remotely sensed data were used as validation of the HyMap products.

5. RESULTS

5.1. Dominant mineralogy in the Rodalquilar caldera complex

The analysis of alteration minerals present in the Rodalquilar caldera complex was mainly concentrated on those specimens which are SWIR active. Even though the main scope of this research focused on the mica-smectite and kaolin groups, the identification of other minerals is important for supporting the interpretation of the above mentioned groups. In this sense, detection of SWIR active secondary minerals on one hand, and non-active SWIR minerals with XRD on the other hand, was also useful. Besides this, its results combined with TGA were used in the validation of the spectroscopy results.

5.1.1. Hydrothermal alteration mineralogy identified with ground and laboratory SWIR spectroscopy

Identification of the dominant SWIR active mineralogy was done based on the deepest absorption feature in the 2100-2500 nm spectral region. Based on the methodology suggested by Pontual et al. (1997), four spectral ranges were defined, as is shown in Figure 5-1 and Table 5-1. Once the spectra were grouped, parameters such as presence of secondary features, doublets and other unique characteristics were used for the subsequent identification of spectral groups. Finally, with aid of the TSA interpretation and comparison with the USGS spectral library, the minerals present in each group were identified. The distribution of the recognized minerals is displayed in Figure 5-2.

Samples representing the purest spectra were selected as end-members for the identified minerals (Figure 5-3), except for the smectite-mica and kaolin groups which are treated with more detail in section 5.2 and 5.3, respectively. For the identified minerals, their origin, whether hydrothermal or secondary, was considered based on their mineral associations, spatial distribution in the study area and other referred works.

The spectral group with the shortest wavelengths, from 2100 to 2175 nm, is composed by zunyite, pyrophyllite and alunite (Figure 5-3 a, b and h). Zunyite and pyrophyllite were identified as characteristic minerals for the advanced argillic alteration zone; their association is typical of temperatures above 200°C and presence of per-aluminous fluids, giving information about the extreme physicochemical conditions of the mineralization. Alunite, according with Arribas et al. (1995), in surface is present only as a product from supergene alteration, and hence is not interpreted as characteristic of any alteration zone; two different types of alunite were identified according with the 2200w parameter: K-alunite and Na-alunite, the K-rich end-member is determined by the shortest alunite wavelengths, close to 2164 nm, whereas the main absorption feature of the Na-rich end-member is placed at 2169 nm.

Most of the samples belong to the 2175-2220 spectral group, which is dominated by the presence of smectite, illite-smectite and kaolin groups (Figure 5-3 c-g); minerals within these groups are differentiated by the presence of typical doublets in the 1400 and 2200 features in the kaolin group, and by the relation *2200D/1900D* which tends to be higher also in the kaolin minerals, in close relationship with the more ordered lattice structure. All these minerals are of hydrothermal origin and can be related to different alteration zones, besides kaolinite and halloysite in the study area that are also formed by weathering. Gypsum also presents the main absorption in the 2175-2220 nm spectral region, but the unique shape of the whole spectrum of this mineral is enough for an easy identification (Figure 5-3i); in the study area it is from secondary origin.

Minerals with the deepest absorption between 2220-2500 nm are just a small portion of the dataset and correspond mostly to secondary mineralogy (Figure 5-3 i-m), jarosite is commonly found in mixtures with alunite, opal is frequently present as secondary product, but can be also related to advanced argillic alteration. The presence of Fe and Mg clays is related with rocks with low or no-hydrothermal alteration, mainly andesites. Finally, identified carbonates are exclusively dolomite, and given their spatial distribution are associated with the tertiary marine units.

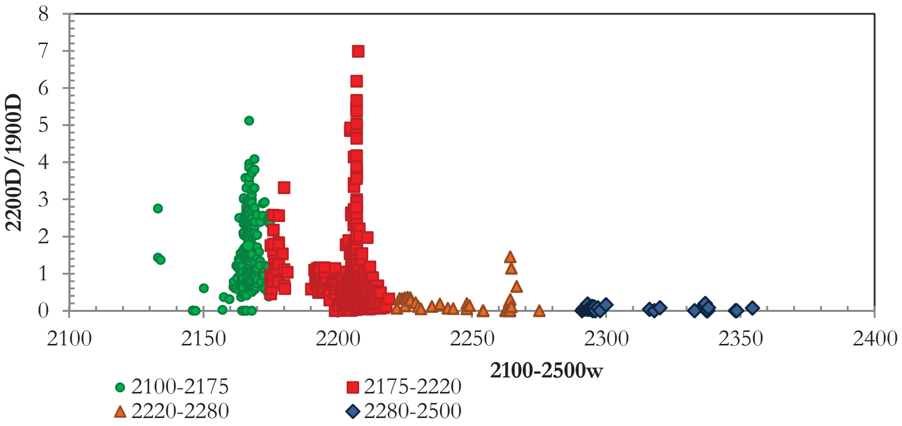

Figure 5-1: Position of the deepest absorption feature in the 2100-2500 nm range and separation by spectral groups

Table 5-1: Identified spectral groups based on the deepest absorption feature between 2100-2500 nm and SWIR active mineralogy

SPECTRAL RANGE	SPECTRAL GROUP	IDENTIFIED MINERALOGY	ORIGIN
2100-1275	**Zunyite**	Zunyite	Hydrothermal origin, characteristic of advanced argillic alteration
	Pyrophyllite	Pyrophyllite	Hydrothermal origin, advanced argillic alteration
	Sulphate	Alunite (Na, K)	Supergene alteration. K and K varieties
2175-2220	**Sulphate**	Gypsum	Supergene alteration
	Illite-muscovite	Illite	Hydrothermal origin
	Smectite	Montmorillonite	Hydrothermal origin
	Kaolin	Kaolinite	Hydrothermal and secondary origin
		Dickite	Hydrothermal origin
		Halloysite	Hydrothermal and secondary origin
2220-2280	**Sulphate**	Jarosite	Secondary origin.
	Other minerals	Opal	Hydrothermal and secondary origin
2280-2500	**Carbonates**	Dolomite	Associated only with sedimentary units
	Other min.	Mg clays	Secondary alteration

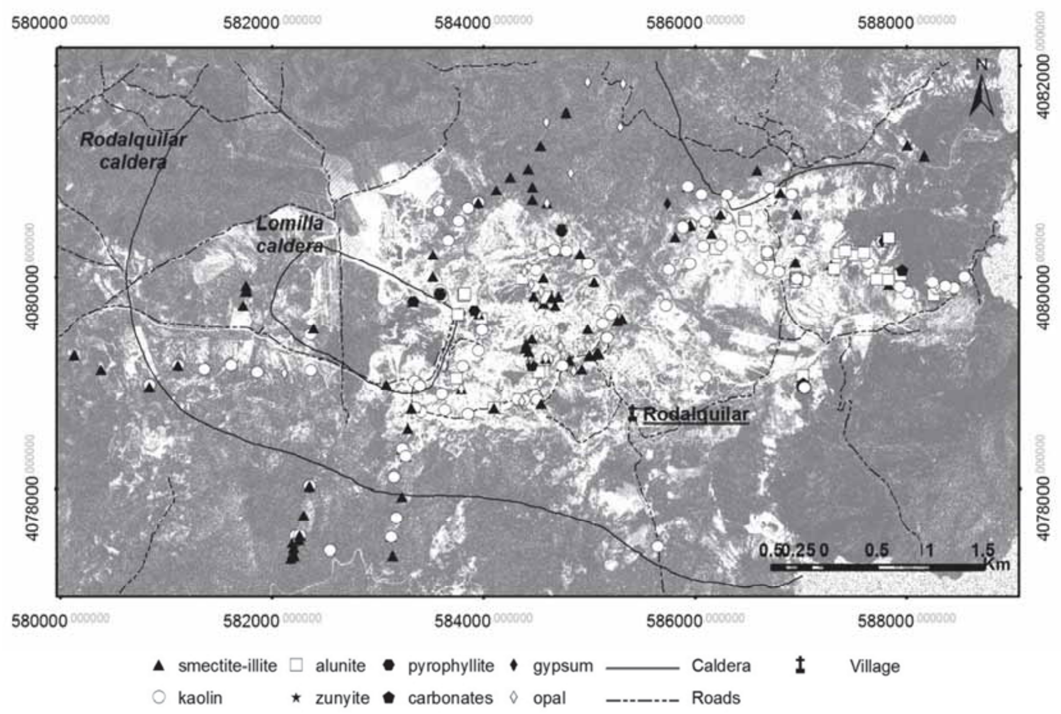

Figure 5-2: Distribution of the identified mineralogy by using ground and laboratory spectra

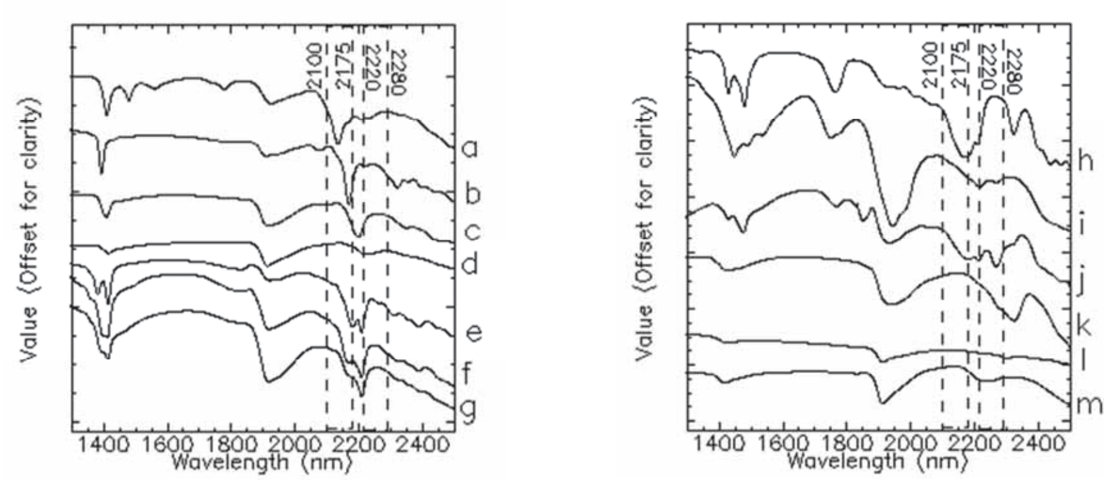

Figure 5-3: Reflectance spectra of the end-members of the interpreted SWIR active mineralogy. a) zunyite b) pyrophyllite c) illite d) montmorillonite e) dickite f) kaolinite g) halloysite h) alunite i) gypsum j) jarosite-alunite k) dolomite l) Mg clay m) opal. Spectra of illite, montmorillonite, kaolinite and halloysite are just representative, but not end-members at this stage.

5.1.2. Hydrothermal alteration mineralogy identified with XRD

Although XRD analysis concentrated in the smectite-illite and kaolin groups, the results revealed also information about hydrothermal mineralogy that is not detectable with SWIR spectroscopy, but it is worth to include them in the observations. The qualitative mineral identification for selected samples is given in Appendix 9.

In most of the analysed samples, diffractograms are dominated by the basal reflections of quartz, which is expected because of the dominant rhyolitic lithology in the Rodalquilar caldera. Identification of quartz in

XRD analysis is important not only for its geological meaning, but also for the interpretation of other minerals that share the same peak position and that are masked due to the strongest response of quartz. Adularia, which is an indicator of pH conditions in low sulfidation systems, was also found in few samples associated with illite 2M1, this will be further analysed in section 5.2. Moreover, results of SWIR spectroscopy were validated for zunyite and alunite. Zunyite was identified as a mixture only with quartz. Alunite samples that revealed different composition in SWIR spectra did not show any significant difference that could be interpreted as compositional change in XRD data. Minerals of the smectite, illite-muscovite and kaolin groups were satisfactorily identified and the results were used to complement the *crystallinity* analysis that is presented in the following sections.

5.2. *Crystallinity* and compositional variations in the smectite – illite group

Samples identified as members of the smectite and illite-muscovite groups were isolated for specific analysis from the spectral mineralogical interpretation conducted before. Aiming to study the crystalline and compositional variations that define the smectite-illite-muscovite mineralogical sequence, SWIR spectral parameters related to water and aluminium-hydroxyl features were correlated. Furthermore, rock samples considered as representative of different degrees of crystallinity were selected for validation and complementary analysis with XRD.

5.2.1. SWIR smectite-illite *crystallinity* in ground and laboratory SWIR spectroscopy

Since different mineral groups share similar features in the 2175-2220 spectral group, samples containing only smectite, illite and muscovite had to be isolated in order to get the purest specimens as possible. These minerals share the same wavelength position of the 1400, 1900 and 2200 nm features with the kaolin group, but the characteristic doublets at 1400 and 2200 nm features in the latter, caused by the location of the -OH group in the crystal lattice, are commonly used to separate kaolins from the smectite-illite-muscovite minerals. Opal and gypsum are in the same spectral group, but they have deeper and broader 1400 and 1900 nm features because of the increased amount of water hosted in a highly disordered structure (Hunt, 1977). The relationship of the variations in the reflectance spectra according to the mineralogy and structural ordering are shown in Figure 5-4.

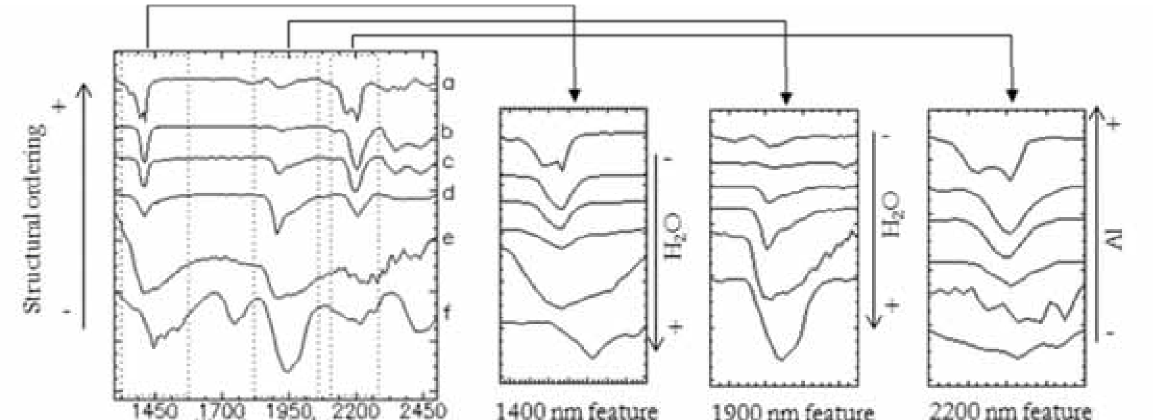

Figure 5-4: Relationship of the spectral parameters with the reflectance spectra. 1400 nm feature (*1400AS*): broadens to longer wavelengths with increasing water content and form doublets at shorter wavelength depending on the OH position in the crystal lattice. 1900 nm feature (*1900D*): becomes deeper with increasing in content of water molecules. 2200 nm feature (*2200D* and *2200AS*): related with the Al-OH bending, becomes deeper with increasing Al, and tends to form doublets to shorter doublets according to the structural position of the hydroxyl, as in the 1400 nm feature. Reflectance spectra from the USGS spectral library (Clark et al., 2007) : a) kaolinite, b) muscovite, c) illite, d) montmorillonite, e) opal, f) gypsum .

The relationship of the 1400, 1900, and 2200 nm features allows separation of these minerals from other with similar characteristics and it is shown in the Figure 5-5. The most determinative parameter is the ratio *2200D/1900D,* since it responds to the aluminium and water content and is an indicator of the *crystallinity* degree in the mineral lattice. It was calculated in order to establish the variability in the studied set of minerals. In such way, high values of the *2200D/1900D* ratio characterize aluminium-rich and well-ordered minerals such as kaolins; in contrast, very low values are typical from highly-hydrated and poorly-*crystallized* minerals, such as gypsum, opal, or mixtures of hydrated minerals in general. The smectite-illite-muscovite mineral sequence falls in the middle of those extremes. Accordingly, the most hydrated and less ordered mineral of the sequence, that is montmorillonite, has relatively low *2200D/1900D* values. The water-loss and increment in aluminium content – and hence an increment on the vibrations of the Al-OH bending – that characterize the transition from montmorillonite to illite and muscovite is accompanied by a gradual increment of that ratio, and consequently, an increasing in the *crystallinity* degree.

The symmetry of the 1400 nm feature, or 1400AS parameter, was used as second determinant factor for smectite-illite-muscovite identification. This absorption feature is particularly useful since its shape, specifically the asymmetry, is function of the amount of water and the position of the hydroxyl in the crystal lattice at the same time. The hydroxyl position in the highly-ordered structure of kaolin minerals causes a doublet likewise in the 2200 nm feature, and hence, the absorption feature leans to shorter wavelengths. In contrast, the slightly less ordered structure of muscovite and illite lacks of such doublet, producing a sharp and symmetric feature. The gradual increasing of water in the structure of the minerals is evidenced by the broadening of the 1400 nm feature towards longer wavelengths, which is also interpreted as decreasing in the crystallinity degree.

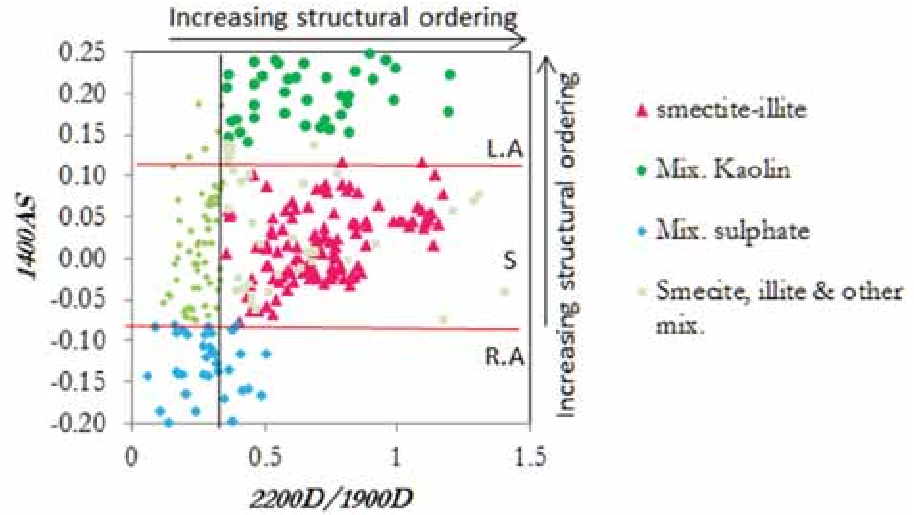

Figure 5-5: Relationship between the *1400AS* and *2200D/1900D* spectral parameters for differentiation of minerals of the 2175-2220 spectral group. Horizontal red lines are the boundaries for *1400AS* parameter; LA (left asymmetry) indicates position of hydroxyl groups, S (symmetric) indicates no hydroxyl feature and low water content, RA (right asymmetry) indicates increasing water content. The vertical black line is considered as the limit where highly hydrated mineral or a mixture of water bearing minerals occurs.

Once the smectite-illite-muscovite samples were separated from the other minerals, the variations in *crystallinity* and composition were studied in detail. The correlation between of the different spectral parameters revealed which factors are involved in the gradual *crystallinity* increment in the mineralogical sequence. First of all, the relation between *1400AS* and *2200D/1900D* was checked specifically for this group (Figure 5-6a). The sample with the lowest *2200D/1900D* value and more right-asymmetric feature was considered as the less *crystalline*, and therefore it was selected as the montmorillonite end-member. On the other extreme of the plot, the highest *2200D/1900D* ratio and symmetric or left-asymmetric values were taken as the more *crystalline*. Although well-ordered samples were found, none of them is *crystalline* enough to be considered as a muscovite; consequently, the sample with the highest *crystallinity* value is taken as the highly *crystalline* illite end-member. Minerals in between the two end-members are the transition or gradual interlayering from smectite to pure and well-ordered illite. The distribution of the samples in the scatter plot evidences how along the sequence the amount of water is gradually decreasing, giving place to a more ordered crystal structure.

Different researchers have considered that in a typical muscovite the relationship between the depth of the 2200 and 1900 nm feature should be at least 3:1; hence, in a plot as the one shown in Figure 5-5 the presence of muscovite should be noted at *2200D/1900D* values greater than the ones plotted here; however the 1400 nm feature is equally symmetric in highly *crystallized* illites as well as in muscovites, and therefore the increase of structural ordering along the Y-axis is not applicable anymore if there are muscovites in the dataset.

In the 2200 nm absorption besides the depth, the shape is somehow related to the degree of structural order in smectite-illite minerals. Presence of cations different from Al, or a structural order not typical of smectite and illite, distort the shape of the absorption; therefore a symmetric feature is an indicator of well-crystallized mineral, whereas the asymmetric one indicates a lower degree in the structural order. Based on that, in Figure 5-6b broad and asymmetric 2200 nm feature is related with poorly ordered structures. A barely perceptible trend of symmetrisation of the feature while increasing the *crystallinity* degree is annotated with the grey arrow in the plot. It demonstrates that even though the shape of the 2200 nm absorption is modified with variations in the structural order of smectite-illite, they are not clear enough to be considered as a main *crystallinity* parameter.

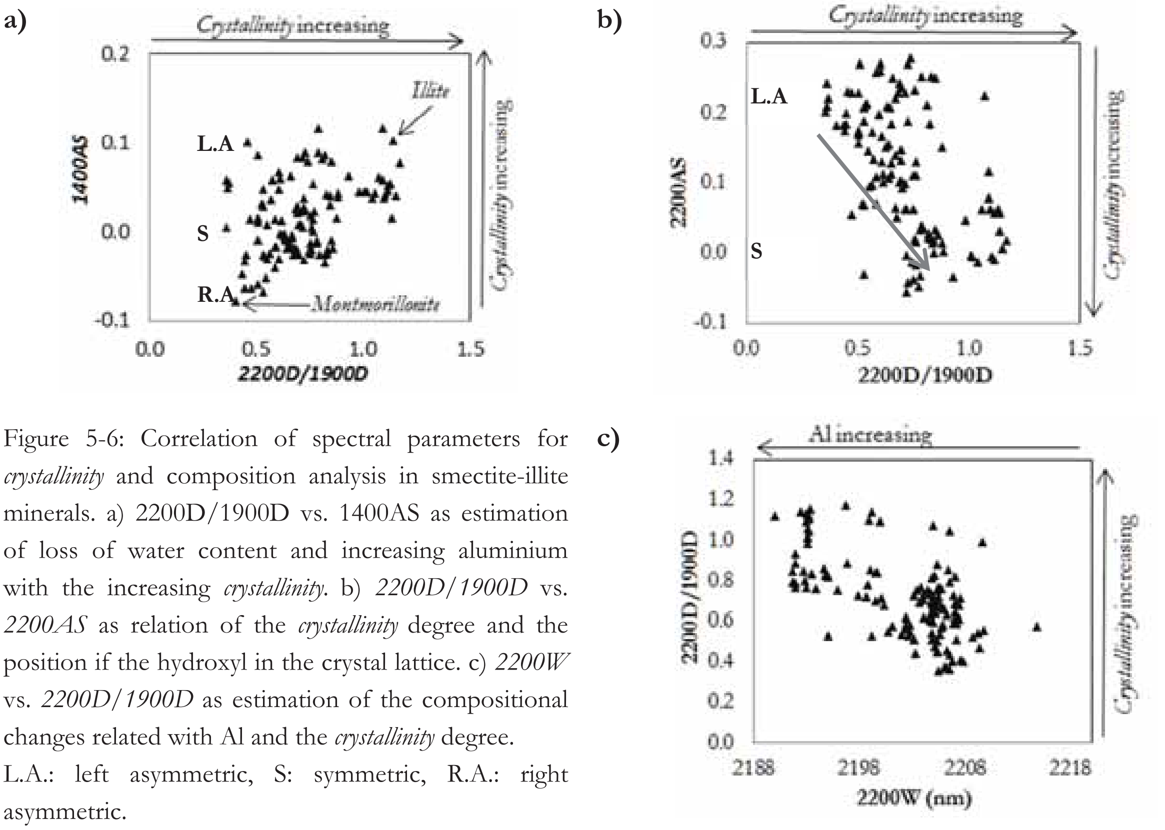

Figure 5-6: Correlation of spectral parameters for *crystallinity* and composition analysis in smectite-illite minerals. a) 2200D/1900D vs. 1400AS as estimation of loss of water content and increasing aluminium with the increasing *crystallinity*. b) *2200D/1900D* vs. *2200AS* as relation of the *crystallinity* degree and the position if the hydroxyl in the crystal lattice. c) *2200W* vs. *2200D/1900D* as estimation of the compositional changes related with Al and the *crystallinity* degree.
L.A.: left asymmetric, S: symmetric, R.A.: right asymmetric.

Finally, the *crystallinity* degree was compared to the compositional changes of smectite-illite, which are related with the wavelength position of the 2200 nm absorption (Figure 5-6c). The wavelength range of this dominant feature varies between 2190 and 2210 nm. As expected, shorter wavelengths are related with the highest *crystallinity* values, meaning that the most organized samples are also aluminium-rich. For longer wavelengths that pattern is not that clear and a wide range of *crystallinity* values are present. However, there is a tendency to exhibit lower *crystallinity* at longer wavelengths, which is interpreted as low aluminium content of the mineral. It is worth pointing out that in this set of samples the diagnostic 2200 nm feature presents a spectral range that does not overpass the 2210 nm (only 2214 nm for one sample). In Figure 5-1 numerous samples present *2200D/1900D* values that fit in the smectite-illite range with absorptions around 2215-2220 nm; according to the detailed analysis of pure smectite and illite specimens, it is concluded that those minerals with longer wavelengths might correspond to gypsum, opal, or mixtures rather than pure smectite-illite, and therefore they are not taken into account the analysis.

In order to visualize the spatial patterns that might be present in the *crystallinity* and compositional variation distribution, these variations were mapped in the study area. For enhancing the *crystallinity* values, the *1400AS* and *2200D/1900D* were multiplied (see Appendix 3). A simple plot was produced where values were divided in 6 classes, representing different degrees of *crystallinity*. At the same time, the compositional variations represented by the *2200W* parameter mapped. Figure 5-7 shows the distribution and the relationship between the *crystallinity* and compositional variations in the area of study. As general patterns, most of the smectite illite samples are concentrated in the central part of the study area, where also the most *crystalline* and shorter wavelength samples are dominant, similarly to the western area. Further away, towards the periphery of the caldera, low *crystalline* and longer wavelength values are dominant.

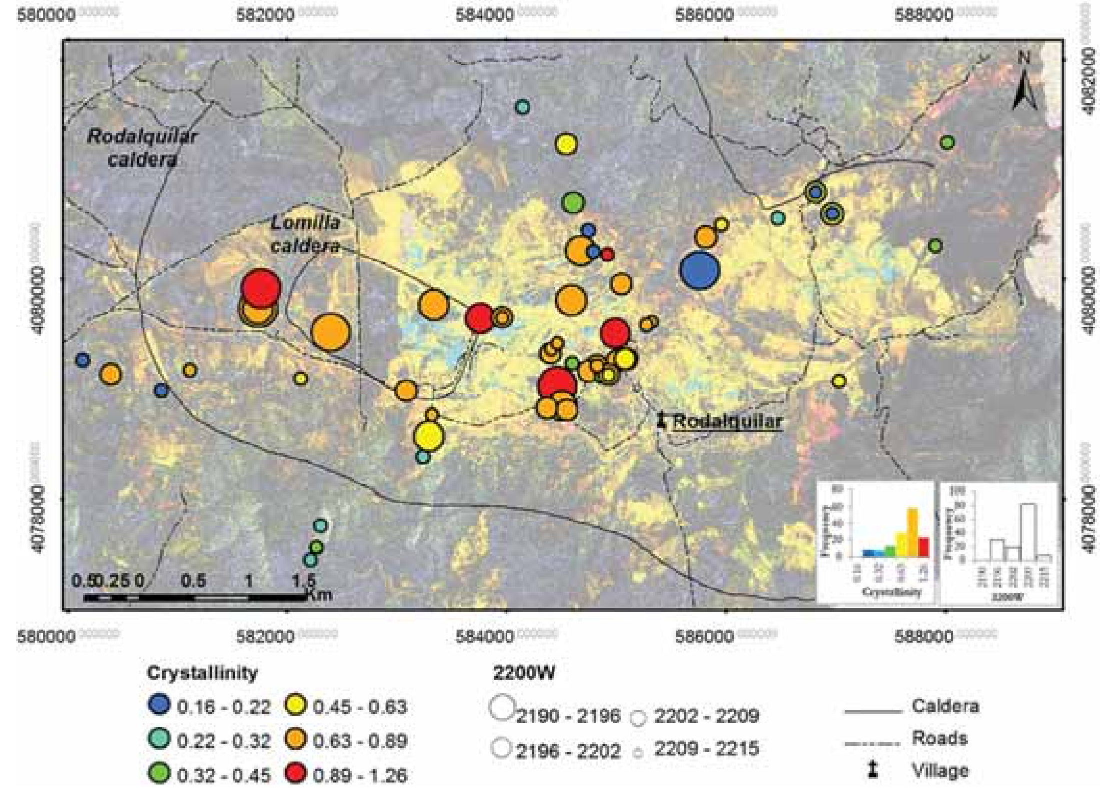

Figure 5-7: Compositional and *crystallinity* variations of smectite-illite in the Rodalquilar area. The size of the circles represent the composition (*2200W* parameter), the biggest circles represent shortest wavelengths and the smaller ones longer values. The colours represent the increasing *crystallinity* from blue (low *crystallinity*) to red (high *crystallinity*). Background image: HyMap wavelength indicating the presence of minerals with strong Al-OH absorption at 2175 nm in cyan, 2195 in yellow and 2220 nm in magenta.

5.2.2. Comparative analysis: Smectite-illite *crystallinity* in SWIR spectroscopy and XRD

The XRD analysis conducted over samples with different degree of crystallinity confirmed the variations in structural order in the smectite-illite minerals (see Appendix 6 and Appendix 7). First of all, a qualitative interpretation of the samples in the XRDcalc V5.0 software revealed the presence of illite 2M, illite 1M and montmorillonite. In agreement with the SWIR crystallinity results, the higher crystalline values match with the illite 2M polytypes, while intermediate values correspond to mixtures of illite 2M and illite 1M, and the lowest values with montmorillonite. In some samples there are mixtures with halloysite as well.

More detailed observations of the position of the first basal reflection, which for pure illites is located at 10Å (8.9°2θ) and for montmorillonite at 15Å (7°2θ), show a good relation with the SWIR crystallinity values. The shape and the position of the peaks were considered as indicator of the degree of structural order in the analysed specimens. Samples with higher SWIR crystallinity values present the narrowest and better-defined XRD profile at 9.5Å (9.2°2θ). For the remaining samples, the profile is less sharp and the d-spacing becomes gradually larger with the decreasing crystallinity. The XRD values were correlated with the SWIR crystallinity values taken as the 2200D/1900D and the enhanced values using the 1400AS parameter as well (Figure 5-8a and b). The correlation between the 2200D/1900D parameter and the XRD data is lower correlation than only correlations of the products of the 2200D/1900D and 1400AS parameters with the XRD data. This shows how the 1400 nm feature is highly affected by the changes in structural order of smectite-illite, and hence its characterization gives valuable support in the crystallinity analysis.

The correlation plots show that there is a good correlation between crystallinity of smectite-illite measured with SWIR spectroscopy and XRD. There are only two samples that can be interpreted as outliers in the correlation. The first one corresponds to the less crystalline sample, which presents a significantly lower angle value (7.0°2θ), meaning that the interlayer d-spacing is much higher than in the other samples (11.8Å); based also in the other peaks at different angles this sample is interpreted as pure montmorillonite rather that an smectite-illite interlayering. The second outlier is the sample with the highest angle or smaller interlayer space (9.3°2θ and 9.4 Å, respectively), which in the SWIR observations is interpreted as moderate degree of crystallization. The XRD qualitative interpretation of this sample gives a mixture of illite 2M and halloysite, therefore -although this is a well-crystallized illite- in the SWIR spectroscopy the mixture with halloysite diminishes the crystallinity measurement. This represents a shortcoming in the use of SWIR spectroscopy in the assessment of crystallinity degree of minerals when mixtures are present and their identification is difficult.

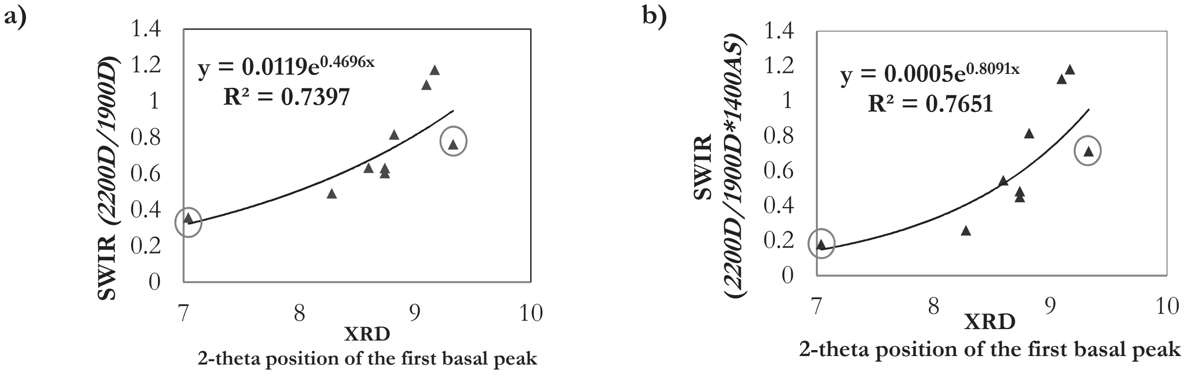

Figure 5-8: Correlation of the *crystallinity* degree measured with SWIR spectral parameters and the position of the first basal reflection of XRD profiles. a. XRD correlation with the *2200/1900D* parameter, b. correlation of XRD with the *2200D/1900D* and *1400AS* parameters. Samples enclosed in circles are considered as outliers.

For the remaining samples, the gradual increasing SWIR crystallinity degree is accompanied by the shifting of the XRD peaks towards larger 2-theta angles in a range from 8.3 to 9.2 °2θ. This is interpreted as the continuous decreasing of the d-spacing when the loss of water in the mineral structure turns into a more organized crystal lattice. Broad interlayering spacing represents higher proportion of smectite over illite and the continuous shrinking between layers is interpreted as predominance of illite over smectite. As a consequence of this process the structure of the smectite-illite minerals becomes more ordered, and hence, more crystalline, likewise is interpreted from the measured SWIR parameters.

5.3. *Crystallinity* in the Kaolin group

Samples in the 2175-2220 spectral range that present doublets in the 1400 nm and 2200 nm absorptions, and which 2200D/1900D ratio are higher than the smectite-illite group, are interpreted as kaolin minerals. As it has been explained before, the development of the characteristic doublets relates to the hydroxyl position in the crystal lattice, and therefore is related with the crystallinity degree of kaolins. Similarly to the smectite-illite minerals, the amount of water in the structure, measured as the 2200D/1900D, is also considered as an indicator of the degree of structural order. Complementary XRD and TGA analysis were used for validation and for improving the understanding about the kaolin specimens.

5.3.1. SWIR kaolin *crystallinity* in ground and laboratory SWIR spectroscopy

The increasing structural order from halloysite, to kaolinite and dickite is described by the development of a doublet near 2164 nm (Figure 5-9a). This particular feature starts as a bump in the less *crystalline* halloysite, which becomes more defined when turning into a more ordered structure in the kaolinite. In the dickite, the doublet is totally converted into a second feature with the minimum absorption near 2180 nm. The evolution of the 2164 nm doublet as function of the structural order is the basis of the kaolinite *crystallinity* index (KX, Equation 4-1), which uses the slopes between 2160-2177nm and 2184-2190nm as estimation of the shape of the doublet.

In order to show the gradual development of the 2164nm doublet –and therefore how the *crystallinity* increases- in the kaolin samples, the parameters of the KX were plotted separately instead of the whole index. In this sense, the *2160D/2177D* and *2184D/2190D* ratios are considered as the kaolin *crystallinity* parameters in the following analysis and the relation of their values is presented in Figure 5-9b. As is shown in Figure 5-9a and b, the most notorious changes are described by the *2160D/2177D* slope; its value increases from halloysite to kaolinite, since this part of the spectra is the most affected by the development of the doublet. Although there are also changes in the *2184D/2190D* slope, they represent a smaller variation and therefore are less significant. Different from halloysite and kaolinite is the behaviour of the spectral parameters in the dickite. Since the good development of the doublet shifts the position of the absorption to longer wavelengths, the *2184D/2190D* ratio is opposite to that of the other two minerals, thus setting up the main factor of differentiation for dickites.

The changes in *crystallinity* from halloysite to kaolinite, onwards considered as the *2160D/2177D* slope, were compared with the amount of water hosted by these minerals, which is also an indicator of the degree of structural order. Since on one hand the *2184D/2190D* slope is clear enough for dickite identification, and on the other hand from the literature is well-known that it does not contain significant amount of water, it is excluded in this part of the analysis. The relation between *crystallinity* and water content for halloysite and kaolinite is presented in Figure 5-9c; as expected, samples with poorly ordered structures contain higher water amounts, whereas for the more *crystalline* samples, there is no correlation between the degree of structural order and the water content. This lack of correlation might be due to different types of mixtures that are not identified in the reflectance spectra. For instance, mixtures with hydrated minerals such as halloysite and montmorillonite might increase the depth of the water features.

Furthermore, the presence of illite could smooth the 2164 nm doublet, giving the appearance of lower *crystallinity* degree, or small amounts of sulphates might enhance the doublet, seeming that the sample is highly *crystalline*.

a)

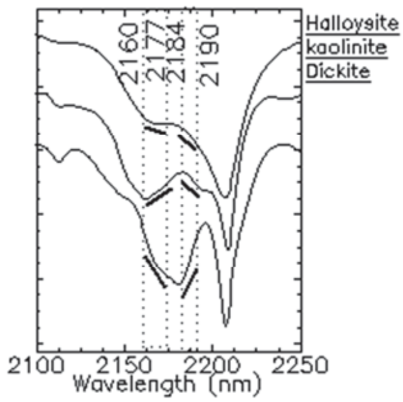

b)

c)

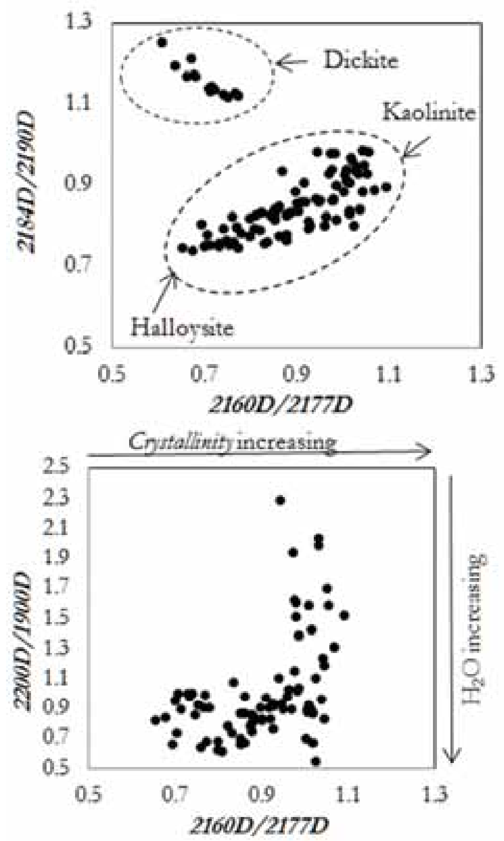

Figure 5-9: Spectral parameters used for the *crystallinity* analysis in kaolin minerals. a) Relation of the slope parameters*2160D/2177D* and *2184D/2190D* with the reflectance spectra. b) Slope parameters *2160D/2177D* vs. *2184D/2190D* used for differentiating of the kaolin minerals based in the shape of the 2164 nm doublet. c) Comparison between kaolinite *crystallinity* taken as the *2160D/2177D* slope and the water content as *2200D/1900D* ratio. Reflectance spectra from the USGS spectral library (Clark et al., 2007).

Similarly to the 2200 nm absorption, at 1400 nm doublets are developed because of the OH-stretching. Albeit the specific wavelength position and the definition of those features vary with the degree of crystallinity of the minerals, likewise at 2200nm, the 1400 nm feature is narrower, hindering its analysis. Nonetheless, some attempts of extracting slope or asymmetry parameters meaningful for crystallinity analyses were done, without satisfactory results. Therefore the 1400 nm absorption is not used as a direct measure of structural order in kaolin minerals, but just as support for the general observations.

In order to visualize the spatial distribution and the *crystallinity* variations of the kaolin minerals, the *2160D/2177D* values were mapped for halloysite and kaolinite, as well as the distribution of the dickite (Figure 5-10). A cluster of samples with different values or c*rystallinity* is located in the north-eastern part of the study area. In the outermost regions of the altered zone, well-*crystallized* kaolinite is present, whereas towards the centre, kaolin minerals are sparse and low-*crystallinity* is dominant.

5.3.2. Comparative analysis: Kaolin crystallinity in SWIR spectroscopy, XRD and TGA

XRD and TGA analysis were conducted over a selection of samples in order to determine whether the changes in crystallinity values correspond to changes in the structural order, or if they are affected by mixtures. The qualitative XRD results –conducted as the mineral matching with reference datasets in XRDcalc software- suggest that most of the samples are mixtures among kaolinite, halloysite, illite or montmorillonite (see Appendix 9). However, despite it was expected to find a dominant and sharp peak to characterize the kaolin samples -as it happened with the smectite and illite ones- several peaks between 10 and 14°2θ (8.9-6.2Å) were found instead (Appendix 6). This might be caused by the preparation of the samples that did not prevent a preferred orientation of the minerals, affecting the XRD measurements, and as a consequence making the qualitative results less reliable. Even though this might represent a shortcoming in the interpretation of the diffractograms, valuable information can still be extracted.

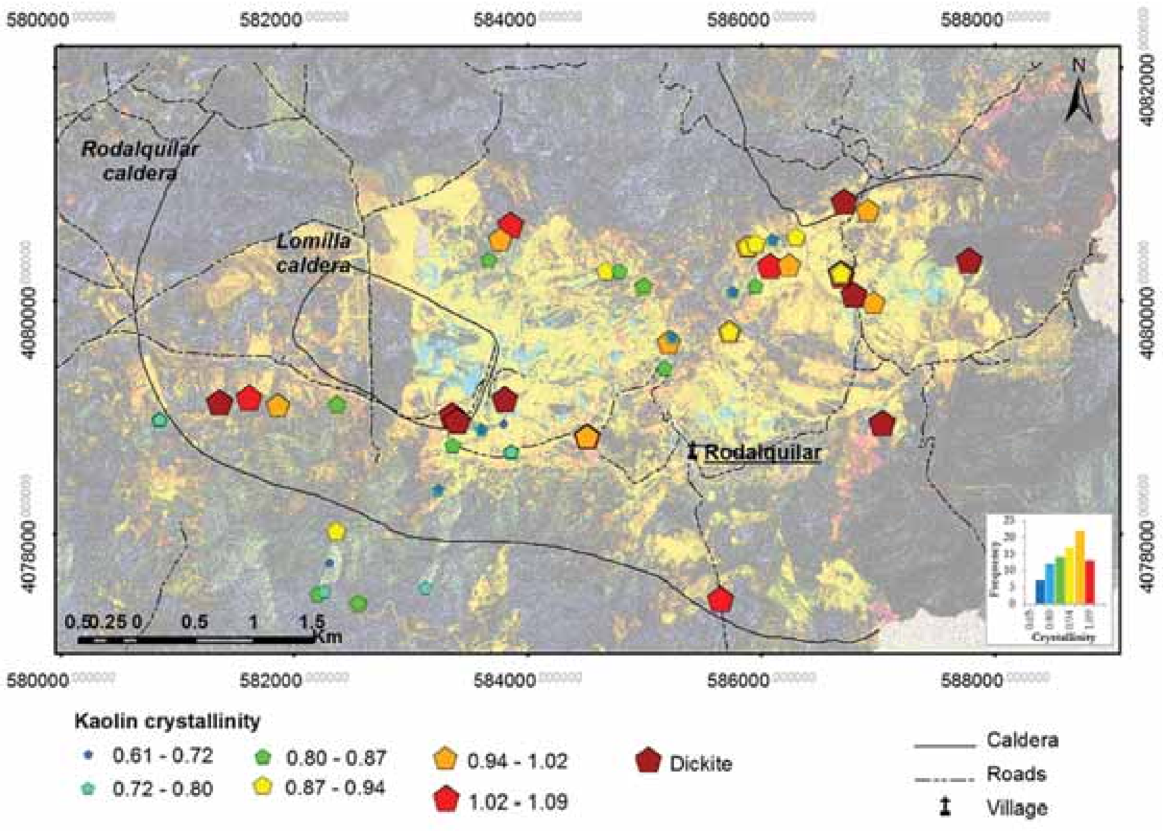

Figure 5-10: Spatial distribution of the ground and laboratory spectra identified halloysite and kaolinite and their variations in the *crystallinity* degree (blue to red colours) and spatial distribution of dickite (dark red). Background image: HyMap wavelength indicating the presence of minerals with strong Al-OH absorption at 2175 nm in cyan, 2195 in yellow and 2220 nm in magenta.

The characteristic values for the first basal reflection of kaolin minerals are about 7.2Å (12.3°2θ) for dickite and kaolinite, and 7.4 to 10Å (11.8-8.9°2θ) for halloysite. The range where the diffractions are present confirm that indeed, kaolin minerals are present in the samples, but the specific mineralogy, and even less the crystallinity degree, cannot be interpreted. Only for one sample, besides the typical kaolin reflections, there is one single peak at 8.9°2θ, that might indicate mixed interlayering with illite.

For identification of mineral mixtures, TGA analyses result are more reliable. The nature of these analyses allows a clear distinction between kaolin and smectite-illite minerals. Particularly, from the shape of the 1st derivative TGA curves the temperature of maximum rate of weight loss is easily inferred by the position of the peaks. The mass change -due to dehydration or dehydroxilation in clay minerals- occurs at specific temperatures for determined mineral groups and might be related with the degree of structural order. In kaolinite and halloysite, there is a single sharp peak about 500ºC, whereas for illite and montmorillonite, the peaks are broader and at higher temperatures.

Based on those criteria, the TGA and 1st derivative TGA curves were interpreted (see Appendix 8 and Appendix 9). Samples with only kaolin-like peaks were grouped as pure kaolin, regardless whether it is kaolinite or halloysite, and samples with kaolin-like and smectite or illite-like peaks were grouped as mixtures. Afterwards, the temperature of the kaolin peak in the 1st derivative TGA curve was compared with the measured SWIR *crystallinity* (Figure 5-11). Dickite is not included in this figure since it has different TGA curves and SWIR spectra.

Although the number of samples in each group (pure minerals and mixtures) is not enough for defining patterns, some relations can be foreseen. On one hand, samples with kaolin and smectite-illite mixtures present a random behaviour regarding TGA observations, meaning that indeed the mixture is affecting the *crystallinity* parameters measured with SWIR spectroscopy. On the other hand, in Figure 5-11 three out of four pure samples apparently present coherent trends respect to the kaolin temperature peak. In the sample with the highest *crystallinity* value the weight loss due to dehydroxylation occurs at the highest temperatures, whereas the remaining two samples with lower *crystallinity* present lower temperatures as well. Even though these samples are too few to lead to strong conclusions, they might suggest trends that are worth it to analyse more carefully with a larger set of samples.

Even though the weight-loss is proportional to the amount of water that is hosted in the crystal structure, it is also affected by the rate at which the samples are heated. Since the conditions of measurements were not the same for all the samples, it was not feasible to correlate the weight changes with the water content in the structure, and hence, the crystallinity.

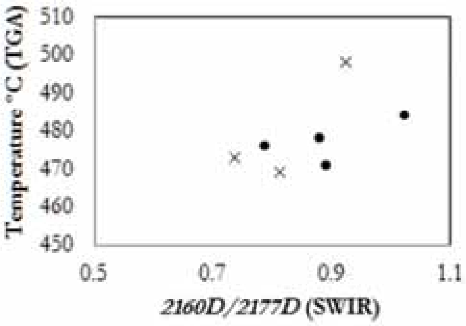

Figure 5-11: Comparison between SWIR *crystallinity* results and the temperature at the maximum rate of weight-loss of pure and mixed kaolin samples. Black circles represent pure kaolin samples and x represent mixtures.

5.4. Imaging spectrometry

Similarly to the ground and laboratory spectroscopy, the SWIR mineralogical analysis in the HyMap scene required first the identification of the general features and then the specific analysis about compositional and crystallinity changes in the smectite-illite and kaolin minerals. The lower spectral resolution, atmospheric disturbances and the variety of materials identified with the remote sensing techniques, makes the interpretation of imaging spectrometry more challenging than the laboratory methods.

Extrapolation of spectral parameters from laboratory to imaging spectrometry

Due to the importance of the water feature at 1.900 μm as a spectral parameter for *crystallinity* analysis, it is essential to make a good estimation of its depth in the absence of the spectral bands related to this feature. The depth of the water absorption feature is calculated based on the few recorded bands related with it by using the Equation 5-1. A1 and A2 are the HyMap bands centred at 2.006 and 1.953 μm, D1 and D2 their respective depth, and A3 is the expected wavelength of the maximum water absorption, set at 1.915 μm from the average of the 1900nm features in the laboratory spectra. For detailed explanation of Equation 5-1 see Appendix 10.

$$1900D = D1 + \left(\frac{(A1-A3)*(D2-D1)}{A1-A2}\right)$$ Equation 5-1

The 1900D, 2200W and 2200D parameters were calculated for the resampled spectral library in order to estimate the expected values in the HyMap analysis. The laboratory kaolin crystallinity results were compared with Equation 4-2 applied to the resampled library as well. The estimation of the 1900D parameter (Figure 5-12a) gives a very high correlation with laboratory results, confirming the usefulness of this type of estimation. The correlation for the 2200W parameter is also good, but as is illustrated in Figure 5-12b, wavelengths of illite-smectite minerals are generally underestimated, meaning that the HyMap wavelength results will give shorter wavelengths than the laboratory spectroscopy, that is an important parameter in smectite-illite composition analysis. Similar is the case of the 2200D parameter (Figure 5-12c), which is highly correlated but underestimated for all samples; therefore it will affect the crystallinity analysis for smectite-illite minerals. The comparison of the laboratory analysis for kaolin crystallinity with the method applied to the HyMap image give a good correlation, validating the applicability of this approach in the imaging spectroscopy analysis.

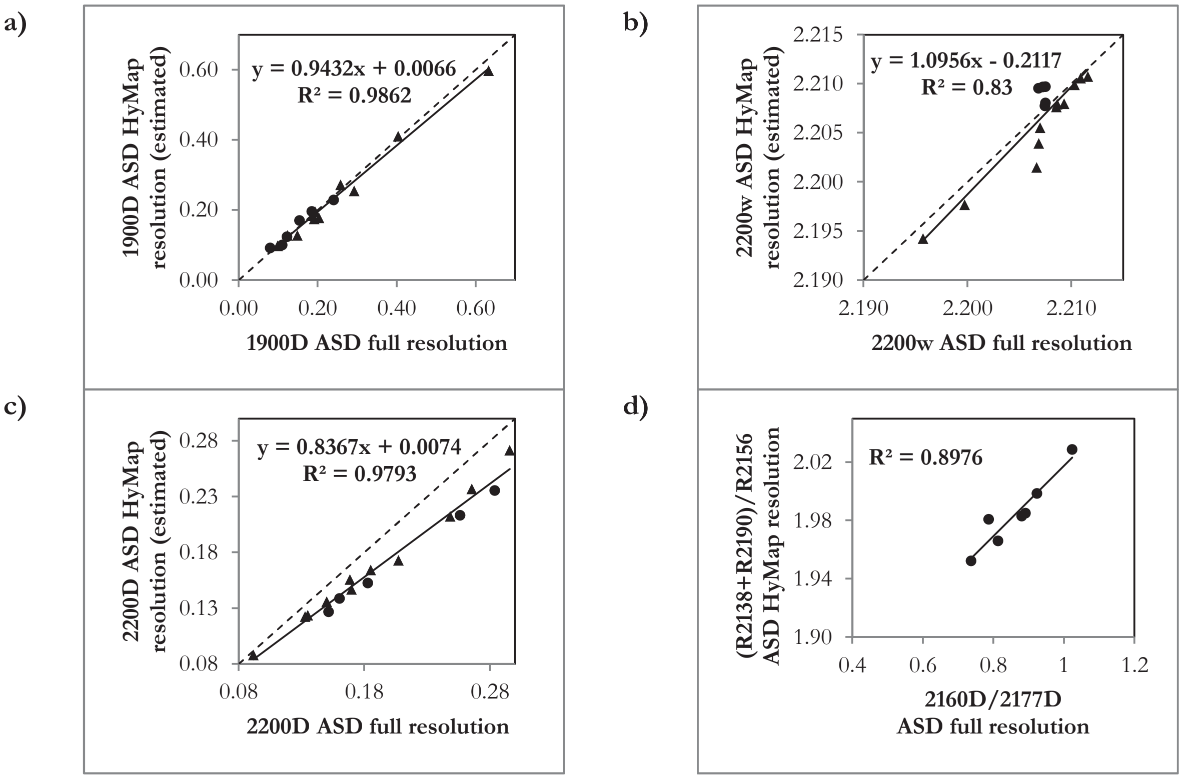

Figure 5-12: Estimation of values of the spectral parameters applied to the HyMap spectral resolution. a) *1900D* parameter: ASD full resolution measured from the spectra and ASD HyMap resolution calculated by using Equation 5-1; b) *2200W* parameter: ASD full resolution measured from the spectra and ASD HyMap resolution interpolated wavelength; c) *2200D* parameter: ASD full resolution measured from the spectra and ASD HyMap resolution interpolated wavelength, d) kaolin *crystallinity*: ASD full resolution measured from the slope parameter in the spectra and ASD HyMap resolution calculated by using Equation 4-2. Smectite-illite is represented by triangles and kaolin by circles.

5.4.1. Hydrothermal alteration mineralogy identified airborne imaging spectrometry

Although the Rodalquilar area is characterized for being a semi-desert area, there is still a vegetation cover that is detected by the HyMap sensor. As a consequence, identification of SWIR active mineralogy in the

Rodalquilar area involved first a process of identification of vegetation coverage. The NDVI index (Figure 5-14a) and the absorption feature of cellulose at 2.090 µm (Figure 5-14b) were used for detecting the distribution and abundance of vegetation that can hinder the mineralogical observations.

The areas covered by vegetation are mostly in south-west and south-east of the study area, as well as in the north. Some vegetation cover is also detected in the west-central part of the image. An area that extends since the centre towards the north-east is barren, as well as the area along the coast. All those areas with a vegetation cover were masked in the remaining image processing in order to avoid interference and misinterpretation of the vegetation features in the mineralogical analysis. The thresholds for masking were first chosen based on the utilization of these indices in other areas with similar characteristics and then adjusted to the image statistics (see Appendix 11).

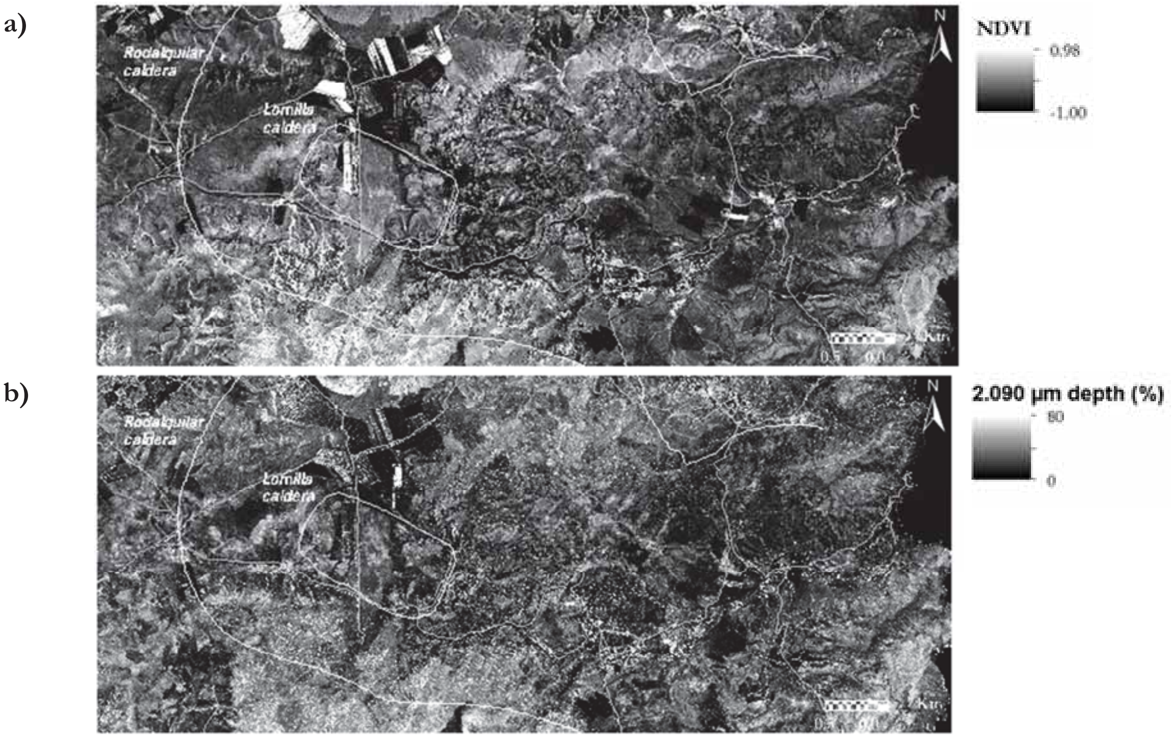

Figure 5-13: Identification of vegetation cover in the HyMap scene. a) NDVI (green vegetation); b) Depth of the cellulose absorption feature at 2.090µm

For identification of the dominant SWIR active mineralogy, a wavelength map that displays the main absorption features from 2.100 to2.400 µm was done. Figure 5-14a illustrates the distribution of the detected mineralogy, which broadly can be grouped into short and large wavelength minerals. The large wavelength group might correspond mostly with the absorption of carbonates at 2.350 µm, which in turn correspond with the Tertiary marine units (Figure 2-2). Aiming to enhance the minerals with shorter wavelengths, a new map for absorptions between 2.150 and 2.245 µm was done. This map, displayed in Figure 5-14b, shows particular abundance of minerals with short wavelength absorptions (blue to cyan colours in the image) concentrated mainly at the north-east of the image. The wavelength position and the distribution of these minerals lead to alunite interpretation; though pyrophyllite might have similar appearance in the image, it is expected to be less abundant than alunite. Wavelengths between 2.180 and 2.220 µm, represented with cyan to green colours, correspond typically to smectite, illite, muscovite and kaolinite; these minerals are abundant in the central and north-eastern zones of the image, but almost absent in the west. Finally, the longer wavelengths displayed in red colour are related with gypsum or jarosite and they are interpreted more as secondary products rather than hydrothermal alteration minerals.

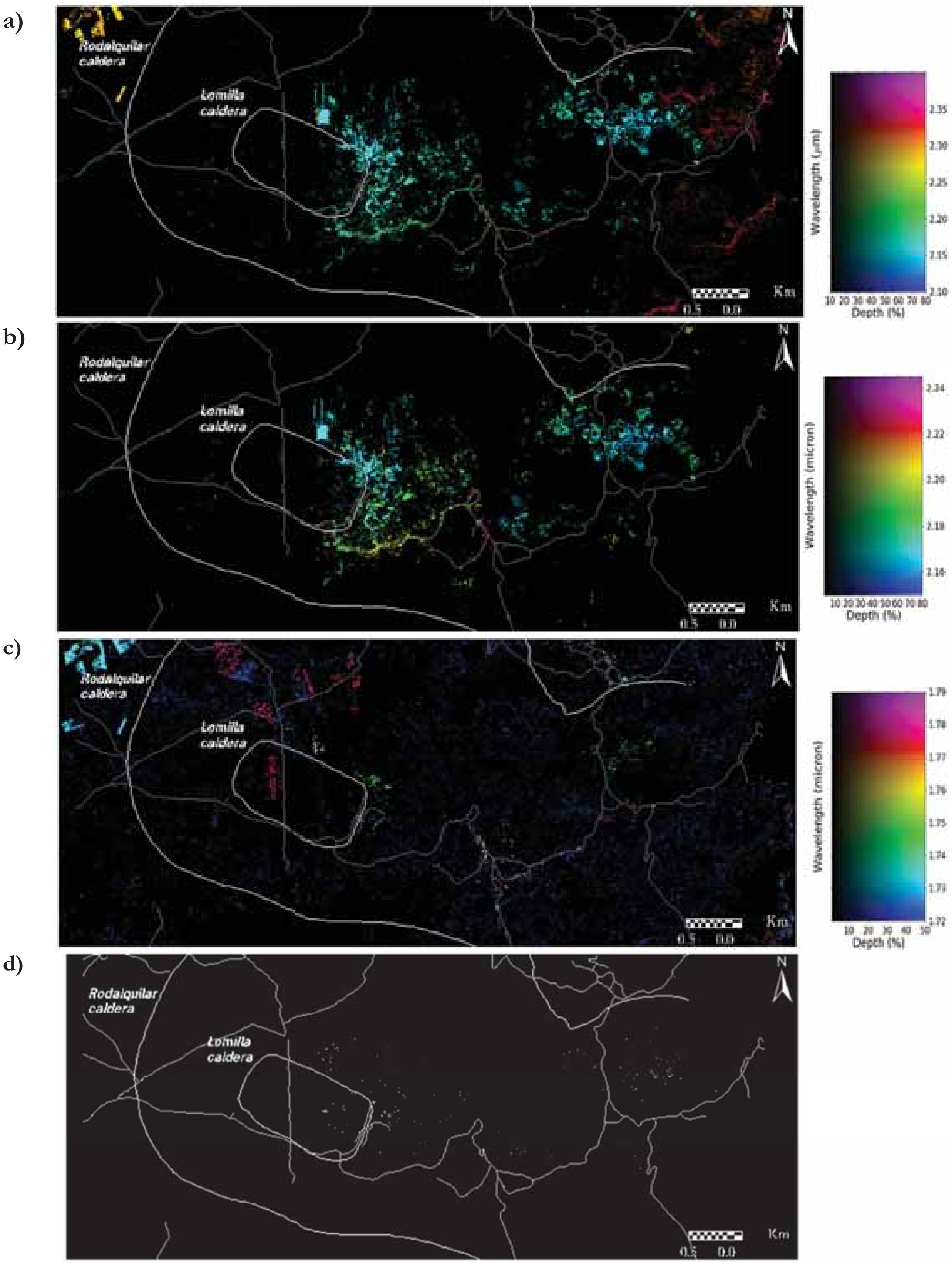

Figure 5-14: Identification of general mineralogy in the HyMap scene. a) 2.100-2.400 μm wavelength map for identification of general mineralogy; b) 2.150-2.245 μm wavelength mapping for enhancing only absorptions in that range; c) 1.720-1.790 μm wavelength mapping for sulphate minerals identification; d) abundance and distribution of pyrophyllite based on the wavelength position and shape of the 2.166 μm absorption feature.

Given the high abundance of sulphates identified in the image and reported in previous studies, a wavelength map for sulphates identification was done using the typical absorption at 1.750 μm. Abundant sulphates were displayed in the centre and north-eastern zones of the study area (yellow-green colour in Figure 5-14c), and might correspond with the alunite 2nd stage reported by Arribas et al. (1995). In order to avoid presence of mixtures or interferences of sulphates that affect the specific analysis of the smectite-illite and kaolin mineral groups, the depths greater than 0.1 between 1.730 and 1.780 μm were masked in the following analysis.

Finally, in order to check the mineral associations that are characteristics of the hydrothermal alteration zones, and to relate them with the *crystallinity* analysis, the distribution of pyrophyllite was mapped as well (Figure 5-14d). From the wavelength map, only features between 2.150 and 2.170 where it is expected to find the main absorption of pyrophyllite were used; besides the sulphate mask for sulphates was applied for extracting the alunite, that has the main absorption at the same wavelength position.

5.4.2. Smectite-illite *crystallinity* observed with imaging spectrometry

After applying masks for vegetation and sulphate minerals, and restricting the image only for those pixels containing absorptions between 2.170 and 2.225 μm, it is assumed that only smectite-illite and kaolin minerals are remaining in the image. The separation of these two mineral groups involved a new masking process. In a similar study, Cudahy et al. (2008) make use of three filters for smectite, white mica and kaolin differentiation. In this research, the smectite and white mica filters together are taken as smectite-illite filter, and the kaolin filter remains the same (Appendix 11).

After applying the smectite-illite filter, the distribution of these minerals in the study area is revealed (Figure 5-15a). Smectite-illite is particularly abundant at the central part of the Rodalquilar caldera, westward Lomilla caldera. The high abundance of these minerals extends along north-eastward direction, whilst southward and north-westward these minerals less abundant. Due to the masking process of minerals and other materials, it is possible that the actual abundance of the smectite-illite minerals is higher than displayed here.

The *crystallinity* assessment of smectite-illite in the HyMap scene based on the *2200D* and *1900D* parameters. The depth of AlOH feature was taken from the interpolated depth of the wavelength of minimum image, and the depth of the water feature from the application of Equation 5-1 to the image. Afterwards, a simple band ratio *2200D/1900D* gave the smectite-illite *crystallinity* variations in the study area. Figure 5-15b illustrates how the crystallinity values are changing throughout the Rodalquilar caldera. The colour scale ranging from dark-blue to red was used for indicating low and high *crystallinity*, respectively. The most remarkable feature is the concentration of highly *crystalline* minerals in the central part of the area, where also the smectite-illite minerals are more abundant. The degree of *crystallinity* is getting lower towards the caldera margins. Although in the laboratory spectra the *crystallinity* results were improved by integrating the 1400 nm feature as well, the extraction of spectral parameters in the HyMap scene were not successful, due to on one hand, half of the feature is obscured by the atmospheric interference, hindering the measurement of the asymmetry, and on the other hand, this part of the spectra is very sensitive for sulphates, making the results not reliable.

The compositional variation, specifically related with the Al content, was analysed by the shifting in the wavelength position of the AlOH feature. The image of the interpolated wavelength was colorized for highlighting the variations from 2.180 to 2.215 μm (Figure 5-15c). That wavelength map shows that even though the wavelength range where the *2200W* shifts is significant (from 2.190 to 2.010 μm), the absorptions between 2.00 and 2.005 μm are highly predominant. The shortest wavelengths are only present in the eastern part of the Lomilla caldera (Figure 5-15c inset). The small areas that show the shortest wavelength mostly coincide with the higher *crystallinity* zones, in the central part of the study area. It is worth it to mention that, as the result of the parameters in the HyMap resolution resampled spectral library, the value of *2200W* parameter might be some slightly larger than the actual ones, and as a therefore the interpretation about Al enrichment has to take this fact into account.

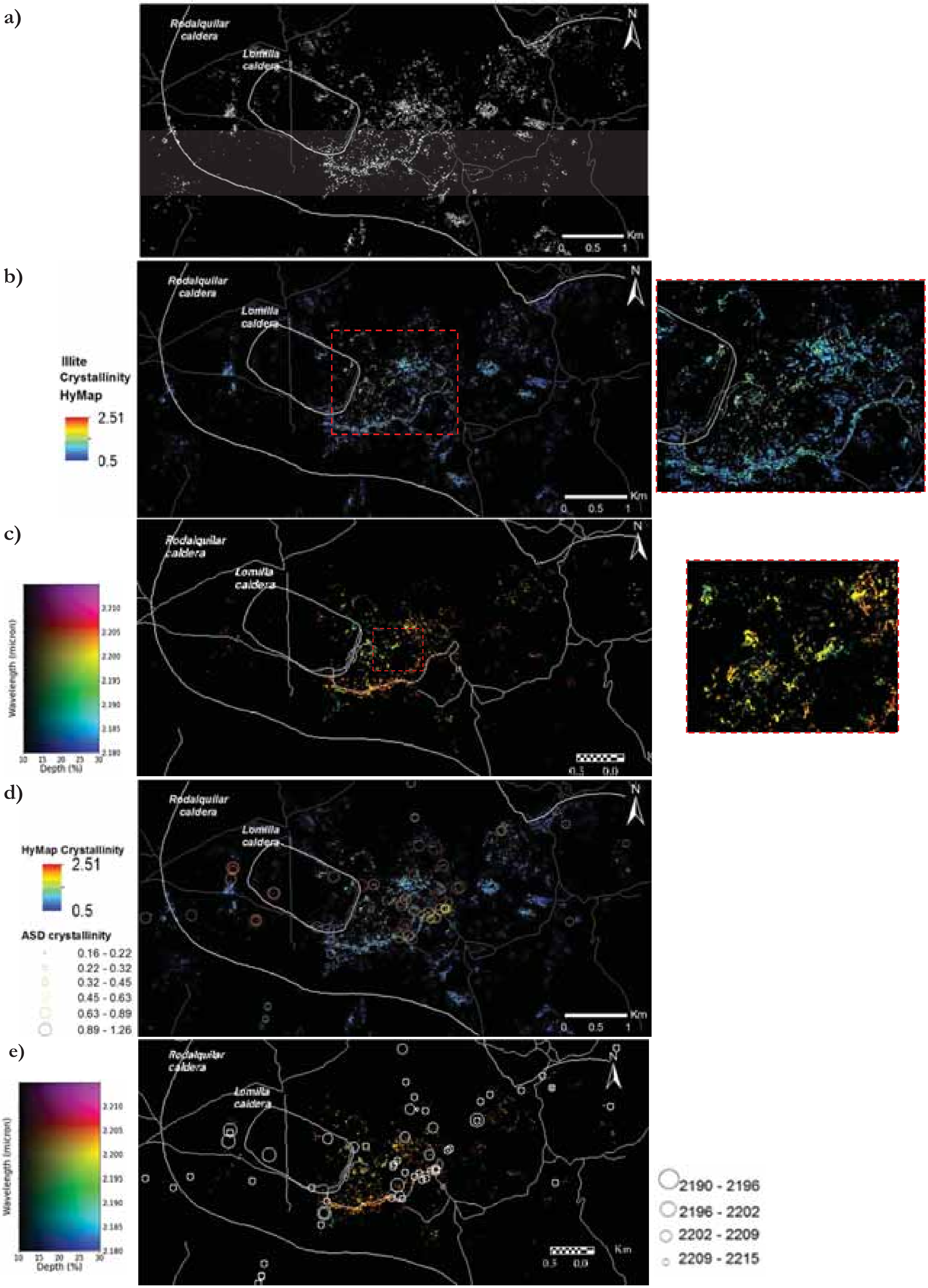

Figure 5-15: HyMap results for smectite-illite: a) HyMap distribution map; b) HyMap *crystallinity* map(*2200D/1900D*), c) composition map (*2200W*) and inset in an area with the shortest wavelength; d) HyMap and ASD *crystallinity* maps, e) HyMap and ASD composition maps

For validating these results, the obtained maps were compared with the results of the ground and laboratory spectroscopy in two different ways, first comparing the specific location of a sample point and its correspondent values in the image, and second, comparing the spatial patterns of the measured parameters for both samples and image.

The validation based on the individual location of the samples points consisted in the matching of the specific coordinates of a sample with the surroundings in windows of 3x3 and 5x5 pixels. A positive matching was given if at least one of the pixels of the assessed window contained smectite-illite. Then, for the points with positive matching, the *crystallinity* and wavelength values were correlated with the same results of the laboratory spectroscopy for a resampled spectral library. As is illustrated in Figure 5-16a, more than 75% of the points where the field data were collected are well identified in the image, validating the approach for the distribution of smectite-illite minerals. The correlation for the *crystallinity* and compositional results in the Figure 5-16b and c seems to be rather small; however, clearly there are trends in the data that lead to a positive correlation between the proximal and the remotely sensed data, validating the results of the latter. The presence of outliers might be related to, on one hand the highly mineralogical variability in a small distance, hindering the representativeness of individual samples in broad areas. On the other hand, the influence of surface patterns as river valleys or roads might bring allochtonous material that obscure the actual *crystallinity* patterns in the HyMap scene.

a)

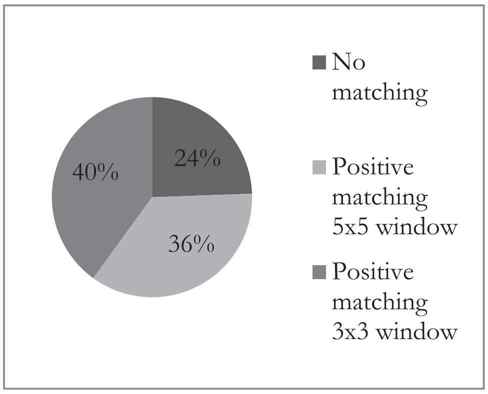

b)

c)

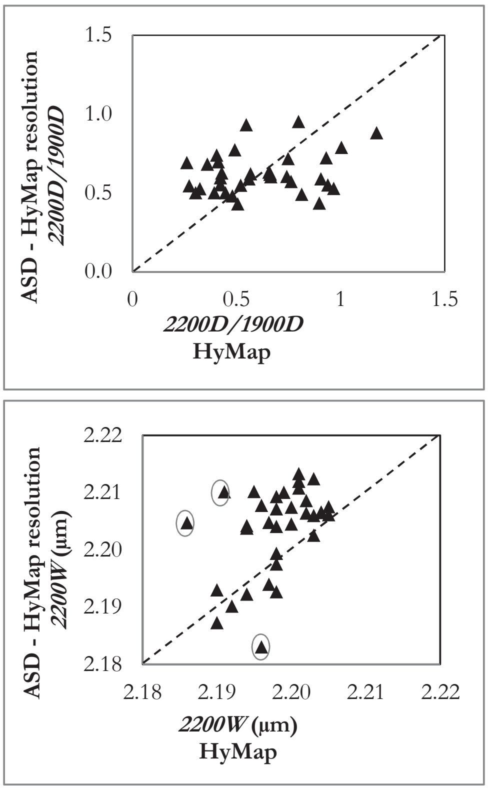

Figure 5-16: Validation of HyMap results for smectite-illite using field data. a) Level of matching between the individual location of the sample points and the pixels that identify the mineralogy; b) Correlation of the *crystallinity* parameters; c) Correlation of the composition parameters. Outliers are enclosed in circles.

In the second validation method, results of field and airborne spectroscopy were overlaid aiming to compare the spatial patterns regarding the variation in *crystallinity* and composition (Figure 5-15e). Regarding the areas of highest and lowest HyMap *crystallinity* values in the central and north-eastern parts of the area, respectively, the field data show a coherent behaviour indicating high and low values in a similar distribution. On the contrary, in the western part of the area where smectite-illite is almost absent and the few identified pixels have low values, the field data is representing opposite patterns. Due to the narrow range of wavelength variation for the identified smectite-illite, is difficult to visualize and compare the HyMap and ASD results; however, the patterns in both dataset coincide in identify the shortest wavelengths in the central part of the study area, and the longest wavelengths in the north-eastern side.

5.4.3. Kaolin *crystallinity* in imaging spectrometry

Owing to the nature of the index for kaolin *crystallinity* assessment in the hyperspectral scene (Equation 4-2), a continuum removed image –with all the before mentioned masks and filters applied- was used instead of the wavelength of minimum image. In the same way as in the smectite-illite interpretation, for kaolin identification the filter proposed by Cudahy et al. (2008) was applied to the HyMap image. After filtering, the distribution of the kaolin minerals in the study area is visualized (Figure 5-17a). Two major zones of abundance are detected, the first one surrounding the eastern part of the Lomilla caldera, and the second one in the north-eastern part of the Rodalquilar caldera. In between these two zones there are also kaolins present, though they are not related to the hydrothermal processes but they are tailing material from the old mining activity

The results of the kaolin *crystallinity* assessment that are illustrated in Figure 5-17b, show zones of higher *crystallinity* values in the central part of the first zone that decrease radially outwards, coinciding with the patterns of smectite-illite *crystallinity* values (Figure 5-15b). Despite of a small patch north-westward also have high values, the geometry of the area suggest that it does not correspond to a geological process, but heap-leach from the mining operation. Unlike the smectite-illite *crystallinity* map, the second zone with high kaolin abundance presents high *crystallinity* values, though the variation –that is also decreasing outwards- is rather small. The third small zone in the middle of the image has similar patterns: high *crystallinity* values in the central part, but with small variation along the area.

The validation of the HyMap results for kaolin distribution and *crystallinity* were conducted following the same methodology as in the smectite-illite group. The matching between the location of the sample points and the identified pixels in the image, shown in Figure 5-18a, gave a poor correlation between the field and the image data. There are three main reasons that can explain this large mismatch. The first one is given by the nature of the HyMap image itself, which records the dominant materials at the surface, that in many cases are related with soils, which obscure the hydrothermally altered rock below. The second one refers to the abundance of sulphates in the surface that can hide other materials, or is present along with the kaolin as mixtures, which are masked in the process of sulphate extraction. The last reason is about the process of kaolin separation from smectite-illite in the HyMap processing, which can over-filter desired information, as is mention by Cudahy (1997). For the pixels with positive matching, the *crystallinity* values estimated in the resampled spectral library were correlated with the image *crystallinity* results (Figure 5-18b). Although the level of correlation seems to be low, clear trends demonstrate that high and low values are coherent; the variation range estimated from the laboratory data is larger than the one in the image, but this can be easily explained by the facts that, on one hand, the reflectance values in laboratory conditions are higher than the ones retrieved from remotely sensed data, and on the other hand, because of the mineralogical variability inside a pixel might distort the features, even though there is a dominant mineralogy. In summary, there seems to be a correlation between the *crystallinity* values of proximal and remotely sensed data, which makes the interpretation of the HyMap scene reliable, at least for the highest *crystallinity* kaolin values that are related to hydrothermal processes. The influence of weathering product is still an unresolved issue in the study area.

For the second method of validation, the *crystallinity* values of the sample points were overlaid on the kaolin *crystallinity* image (Figure 5-17c). This visualization allows detecting where are the zones that represent the mismatch between the field and image data. In the south-western part of the image, no kaolins were identified at all, whereas the field points show that several samples were collected in those areas. The second source of mismatching corresponds to the surrounding of the abundance zones identified in the image. The disposition of the sample points suggest that the abundance zones could be more extended than in the image, in other words, that kaolin might be more abundant than mapped by HyMap. As it was explained before, over-filtering or over-masking seems to have hidden more information than required. Regarding the *crystallinity* values, patterns for low values for both, field and airborne data, appear to be related, whereas for the high values is not easy to make such relation because of the absence of sample points for kaolinite or halloysite in the image zones with high *crystallinity*. However, if the sample points for dickite -that represents a high level of *crystallization* than kaolinite and halloysite- are included, their distribution coincides with the high kaolin *crystallinity* values. Once again, this approach for assessing the *crystallinity* changes in the Rodalquilar caldera is validated.

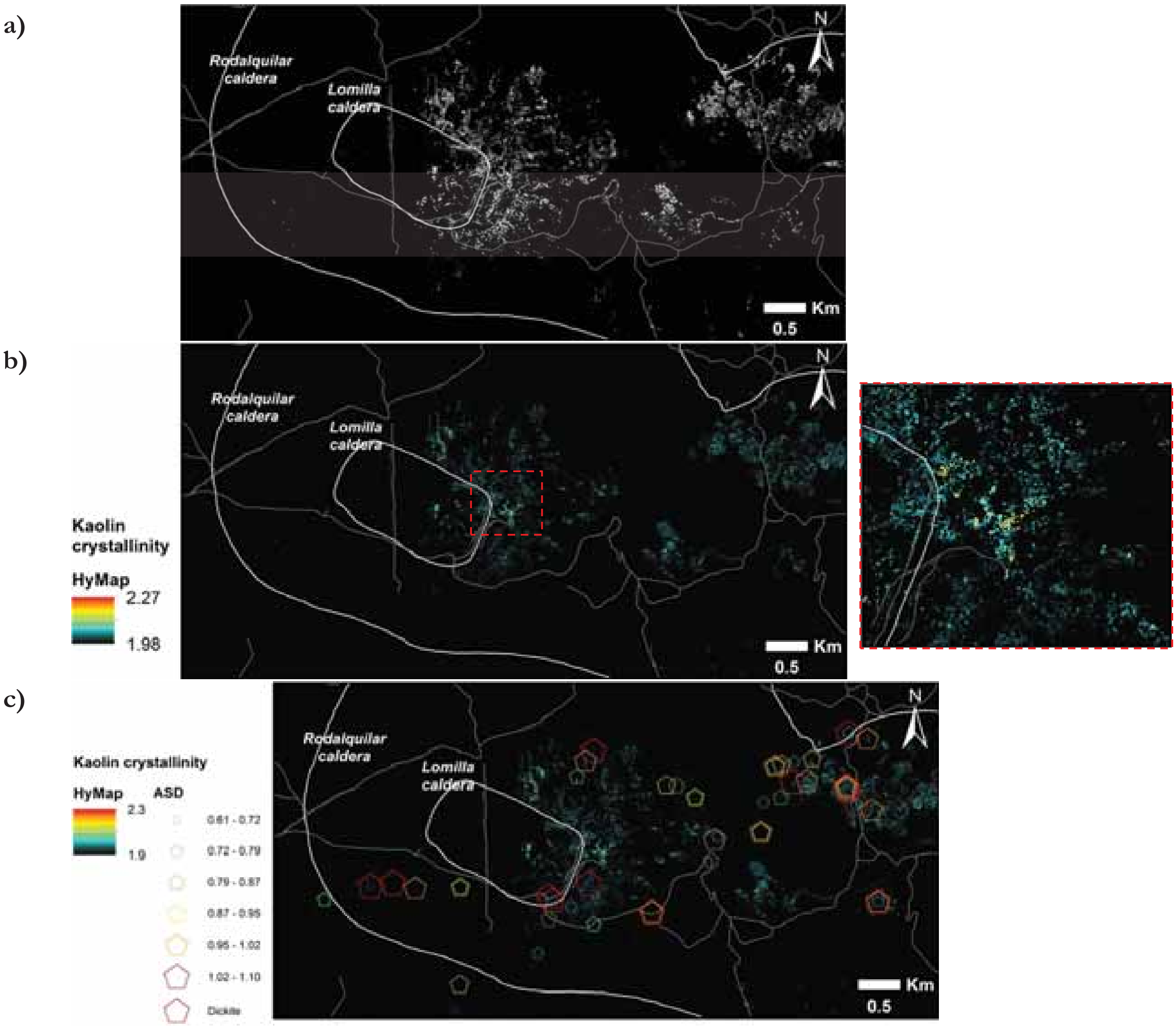

Figure 5-17: HyMap results of kaolin analysis: a) HyMap distribution map; b) HyMap *crystallinity* map; c) HyMap and ASD *crystallinity* map

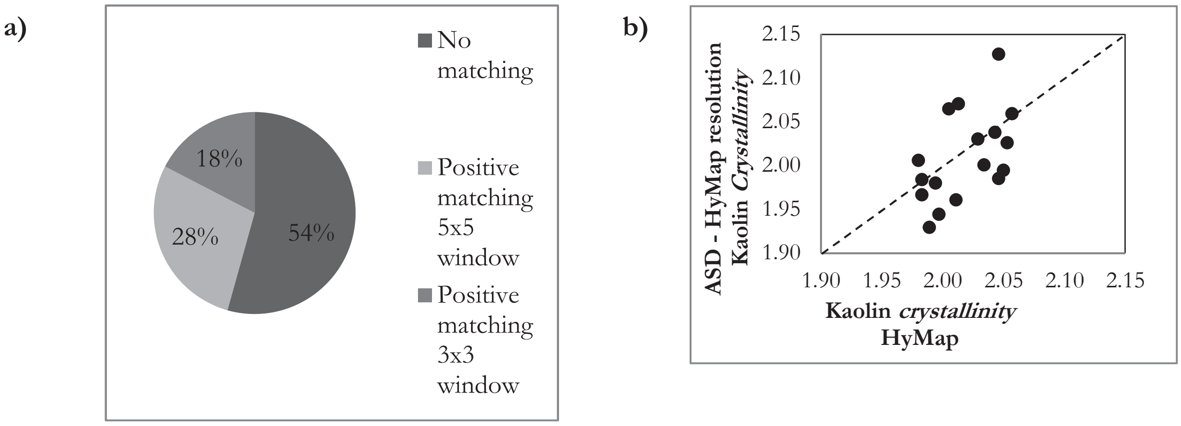

Figure 5-18: Validation of HyMap results for kaolin using field data. a) Level of matching between the individual location of the sample points and the pixels that identify the mineralogy; b) Correlation of the *crystallinity* values based on Equation 4-2.

6. DISCUSSION

The implementation of different techniques, including both proximal and remotely sensed techniques, lead to the detailed study of the *crystallinity* variations of smectite-illite and kaolin minerals in the Rodalquilar caldera complex. The analysis of those variations, their relevance to the understanding of the hydrothermal system and other implications of this research, are discussed below.

6.1. *Crystallinity* variations in smectite-illite and kaolin minerals

The identification of the dominant hydrothermal mineralogy, and the specific *crystallinity* analysis for smectite-illite and kaolin minerals were addressed through two different approaches. First, proximal techniques, making used of either field or laboratory data, and secondly, using remotely sensed data from imaging spectrometry. The interpretation of the proximal data led to the identification and calibration of the main parameters of analysis which were extrapolated to the hyperspectral image in order to get a complete overview of the study area.

SWIR spectroscopy is used as the principal tool to identify the dominant mineralogy in proximal and remotely sensed datasets (Figure 5-1, Figure 5-14a and Table 5-1). The thus recognized infrared active minerals are mostly products from hydrothermal processes, and hence are easily correlated with the typical alteration zones of epithermal systems. Minerals related to supergene alteration, such as alunite, or unaltered rocks, such as dolomite, are also recognized, and even though they do not add directly to the interpretation of the hydrothermal system, their identification is valuable for the understanding of the mineralogical parameters studied in detail. The most abundant minerals that were identified are characterized by their main absorption feature between 2170 and 2225 nm, and mainly correspond to smectite, illite and kaolin minerals.

Smectite-illite group

Smectite and illite minerals taken apart as one single group were analysed in detail for their *crystallinity* and compositional changes. Data from SWIR spectroscopy and XRD revealed that in the study area there are gradual changes in structural ordering and chemical composition from montmorillonite to illite, forming a mineral sequence. In the proximal SWIR data, that sequence is described by the spectral variations of the 1400, 1900 and 2200 nm absorptions, in agreement with the spectral parameters defined by Kruse and Hauff (1991) about the variations of illite polytypes. Minerals with deeper 1900 absorptions and right-asymmetric 1400 features are interpreted as well-hydrated and poorly *crystalline* whereas deeper 2200 absorptions and symmetric 1400 features are interpreted as poorly-hydrated and well *crystalline*. In this sense, the mineral sequence grade from the less *crystalline* end-member montmorillonite-like to the pure and well-*crystallized* illite. Steps in between are smectite-illite interlayering that decreases the smectite content and increases the illite proportion in accordance with the increasing in *crystallinity* degree (Figure 5-6a and b).

The comparison with XRD analysis demonstrates that the shape and depth of the 1400 and 1900 nm SWIR features are indeed correlated with the interlayer spacing of smectite-illite minerals. As is illustrated in Figure 5-8, D-space is correlated with the relation 2200D/1900D and the level of correlation increases when the 1400AS parameter is also taken into account, since all the features related with the degree of structural order are considered.

Based on the shifting of the *2000W* parameter, changes in the composition of the smectite-illite minerals were detected. Despite the fact that feature varies in a small range (Figure 5-6c), minerals with absorptions at shorter wavelength are clearly interpreted as aluminium-rich, as it is demonstrated by Duke (1994) and van Ruitenbeek et al. (2005). In the rock samples, highly *crystalline* illites with small *2200W* values are associated with minerals such as pyrophyllite and zunyite, confirming their per-aluminium content.

Crystallinity and compositional changes of smectite-illite minerals were detected along the complete study area by using the HyMap scene. Even though the 1400 nm feature could not be integrated with the HyMap parameters, the ratio *2200D/1900D* appeared to be useful for the detection of *crystallinity* changes, and a wavelength map for the *2200W* feature was found appropriated to trace the compositional variations. The integration of the HyMap image with the field and laboratory data allowed the identification of two zones of smectite-illite abundance, each one with different characteristics (Figure 5-15).

The first zone in the central part of the study area is marked by the highest *crystallinity* values and shorter wavelengths. The high degree of structural order might indicate that here highly-crystalline illite is dominant and therefore has been formed at temperatures around 300ºC. The prevailing aluminium content is indicator of acidic pH conditions (see Figure 3-1 and Reyes (1990)), meaning that this zone corresponds to the strongest hydrothermal alteration in the system, and this indeed matches with the high-sulfidation Cinto deposit.

In the second zone, in the eastern part of the area, smectite-illite is less abundant, the *crystallinity* is low and there is not significant variation in composition, but the *2200W* values are rather large, around 2205 nm. These characteristics might indicate that in this area the temperatures of alteration were lower and the pH more neutral, meaning that even though the rocks are altered, it is to a lower degree than in the first zone. Here, the Triunfo and Los Tollos low-sulfidation deposits are found. In the western part of the area, were the Maria Josefa deposit is located seems to have similar characteristic as the second zone, but the abundance of vegetation present obscures the features related to the hydrothermal alteration. In the Cinto area, open pit mining activities led to a full-exposure of fresh rock, making this area easily identifiable in the HyMap image; this might influence the clustering of illite in comparison with the Los Tollos area. The possible fact that beneath the soil cover in the Los Tollos well-ordered illite is present is not discarded, and therefore the interpretation done here so far should possibly change slightly. If this is the case, remotely sensed spectroscopy is not the most appropriate tool for the *crystallinity* analysis, but proximal spectroscopy carried out in, for example, drill cores should be used.

Kaolin group

Although the structural order and the spectral features for its measurement are clearer in kaolin than in smectite-illite minerals, the *crystallinity* analysis proved more difficult. The common presence of mixtures not easily identifiable distorts the shape of the absorption features thus hindering the interpretation. The interlayer spacing, location of hydroxyl groups in the structure and the amount of water measured with different techniques lead finally to the recognition of pure and mixed specimens, as well as the distinction of different levels of *crystallinity*.

SWIR spectroscopy along with XRD and TGA techniques were used to lead to a better interpretation of the structural variations in the kaolin group minerals. The similar features of kaolin mixtures with smectite-illite and poorly *crystallized* halloysite might led to the misinterpretation of the *crystallinity* values. Research conducted by Hauff et al. (1990) showed the importance on the identification of this type of mixtures in order to avoid confusion in the genetic interpretation of these minerals and developed strategies for their differentiation based only in the shape of the 1400 and 2200 nm doublets. However, in the analysed Rodalquilar dataset the behaviour of the 1400 doublet did not show coherent results, and as a consequence this feature was not taken into account in the analysis.

Although XRD is a well-known technique in the study of the crystallographic structure of minerals in general, different factors caused the results only to help in the mineral identification, but not with the crystal structure analysis. *Crystallinity* analysis with x-ray diffraction requires specific conditions for sample preparation (e.g. to avoid preference in particle orientation) and configuration of the system that were not used in this research. The different behaviour of kaolin and smectite-illite minerals when they are heated, makes of TGA analysis a more successful technique in mixtures identification. Even though the degree of structural order could not be directly quantified by using TGA, the temperature of the first derivative peak, as well as the identification of mixtures, correlated with the SWIR results led to the understanding of the latter (Figure 5-11).

Solving the problem of mixtures, in proximal SWIR spectroscopy the use of slope parameters shows better results than the relation between the 2200 and 1900 nm features. This implies that in the kaolin minerals the structural order is more related to the position of the hydroxyl group rather than in the amount of water in the structure. Variation in the slope parameter from halloysite to kaolinite and dickite gradually shows how the crystal lattice becomes more organized and stable.

The application of this parameter in the HyMap scene by using Equation 4-2, and its comparison with the location of the field points led to the identification of different degrees of crystallinity in the study area. Unfortunately, the used equation is only suitable for the analysis of the kaolin doublet in the halloysite-kaolinite position, but in the dickite, hence, the latter is therefore disregarded in the HyMap interpretation. The identification of dickite in the field and laboratory spectra, as well as its common association with pyrophyllite and well-*crystallized* illite however allow inferring its presence when needed.

From visualizing the distribution of the zones of major abundance of kaolin minerals (Figure 5-17a) it is evident that most of them coincide with the abundance zones of smectite-illite; however, the *crystallinity* variations behave differently. In first place, there is much less variation in kaolin than in smectite-illite and in second place, the low-*crystallinity* values in kaolin can be interpreted as low-intensity hydrothermal alteration or weathering products, which differentiation is beyond the scope of this research. Besides, despite the image processing intended to get the purest pixels as possible, there might be still mixtures that affect the *crystallinity* values. Therefore, only the more *crystalline* kaolin group minerals are interpreted as from hydrothermal origin. In Figure 5-17b, the more ordered kaolinites present in the Cinto area are slightly associated with the more *crystalline* illites, indicating the variations in the alteration patterns in this area. In the Los Tollos area, even though well-*crystallized* kaolinites are present, they are as well-ordered as the Cinto ones. The *crystallinity* degree and the absence of well-*crystallized* illite leads to an interpretation of temperature of hydrothermal alteration of around 200ºC in low pH acidic conditions (see Figure 3-1 and Reyes (1990)). High kaolin *crystallinity* values in other zones with unique geometric patterns might be related to recent events of mining rather than to geologic processes.

6.2. Crystallinity variations in the Rodalquilar caldera complex

This research intends to go further in the understanding of the Rodalquilar system by going beyond the identification of the mineralogy and the *crystallinity* changes of specific mineral groups. Based on research conducted by Arribas (1995) –which is about the general description and evolution of the deposit-, as well as the study carried out by Bedini et al. (2009) -which is so far the more advanced study using remote sensing techniques in the area-, in this section the obtained results explained previously are integrated with the current knowledge of the Rodalquilar caldera complex.

The mineralogy that prevails in the study area is related either to the lithological units or hydrothermal alteration or supergene processes. The SWIR active mineralogy identified by using the deepest feature in the 2100-2400 nm range in this study is almost the same as the identified end-members in Bedini et al. (2009) for implementation of the Multiple End-Member Spectral Mixture Analysis (MESMA). The surface distribution nevertheless varies from one technique to another for some minerals. The carbonates are the most straightforward mappable minerals, since their shape and the position of their absorption features differs so strongly from the other minerals (Figure 5-14a). The abundance and distribution of alunite is better identified using MESMA rather than wavelength mapping; since in this research alunite was identified aiming to avoid its interference in the smectite-illite and kaolinite analysis, the selection of thresholds led to the identification of only spectra with well-defined sulphate features, therefore its actual abundance might be underestimated (Figure 5-14b and c). The distribution pattern of pyrophyllite, which was considered important because of its association with well-ordered illite, even though is not highly abundant, is recognized in the Cinto and Los Tollos areas, similarly as it was identified in the MESMA analysis (Figure 5-14d)

The search for pure mineral spectra by applying different masks and filters in the hyperspectral image led to a very conservative approach about the distribution of smectite-illite and kaolin minerals. This does however not represent a drawback for the interpretation of the mineralogical changes, since it is only restricting to the clearest and most relevant data. Despite the fact that in this conservative approach the abundance represented in the smectite-illite and kaolin mineral map (Figure 5-15a and Figure 5-17a) differs considerably from the abundance retrieved by MESMA, the distribution of the commonly identified zones is the same. There is an advantage in applying heavy filters and masks for interpretation of altered zones, because it restricts the interpretation only to those areas where the alteration is clearest and therefore it is appropriate enough for the purposes of this research. Besides the abovementioned mineralogy, it is worth it to point out the identification of the mineral zunyite for the first time in the laboratory SWIR spectroscopy, which even though it had been previously reported by Arribas et al. (1995) using other methods. The spectral recognition of zunyite aids to the interpretation of compositional changes in illites.

An interpretation of the spatial distribution of the identified mineralogy is based on the published geological map of the Rodalquilar area (Figure 2-2). From this, it is clear that the abundance of the SWIR identified carbonates belong to the Tertiary marine sediments instead of hydrothermal alteration. The remaining minerals that constitute mostly the hydrothermal mineralogy and the secondary alunite are alteration products in the Cinto ash-flow and Las Lázaras ignimbrite. This is in agreement with the observations of Arribas et al. (1995); from the degree of *crystallinity* of both, smectite-illite and kaolin. It is noted that the most intense alteration is on the rocks of the Cinto ash-flow.

The relationship between the hydrothermal alteration zones proposed by Arribas et al. (1995) and the dominating mineralogy, as well as the *crystallinity* degree of smectite-illite and kaolin are illustrated in Figure 6-1a, b and c, respectively. Alteration minerals in the propylitic zone are hardly identified with SWIR spectroscopy as nor chlorite neither calcite are found in SWIR spectra, and only montmorillonite and smectite-illite are recognized by the very low *crystallinity* values. The intermediate argillic zone is dominated in Los Tollos-Triunfo area by low to moderate *crystalline* kaolin, whereas surrounding Cinto and part of Maria Josefa areas, the kaolin is accompanied by moderate *crystalline* smectite-illite. The advanced argillic alteration zone is covered with, are present well-*crystallized* kaolinite in the central part of the Cinto, and in most of the altered zone nearby Los Tollos. Smectite-illite is less abundant in the latter area than in intermediate argillic zone, but the degree of *crystallinity* is prone to increase with the intensity of alteration. Pyrophyllite is also present in this zone. SWIR active minerals are also identified in the vuggy silica zone, matching with abundant of pyrophillite and presence of zunyite and the highest illite *crystallinity*. The most *crystalline*, although much less abundant, kaolinite is also present in the vuggy silica alteration zone. From this relation *crystallinity*-alteration zone, it is evident how the increasing structural order of smectite-illite and kaolin minerals is extremely close-related with the distribution of the hydrothermal alteration zones. Since these minerals are present along all the hydrothermal alteration sequence, but the ordering of the crystal lattice is almost unique for each zone, the characterization of hydrothermal alteration zones by means of studying the *crystallinity* variations of smectite-illite and kaolin minerals is proven highly suitable. Figure 6-2 summarizes the relationship found between the hydrothermal alteration zones and the *crystallinity* variations in smectite-illite and kaolin minerals.

Previous work, and to some extent this research, have demonstrated how the *crystallinity* degree is a function of the hydrothermal temperature. Given the relationship between the hydrothermal alteration zones and the distribution of the *crystallinity* variations in the Rodalquilar caldera complex, the temperature of formation of the system can be inferred. In a typical smectite-illite sequence, pure montmorillonite is formed from surface conditions up to 170ºC (Figure 3-1 and Reyes (1990)). In the Rodalquilar caldera, this is interpreted as the most poorly-*crystallized* smectite-illites present in the propylitic zone, where the hydrothermal alteration is weak. The increasing *crystallinity* degree in both, smectite-illite and kaolinite, goes along with increasing abundance of these minerals and the intensity in the hydrothermal alteration.

a)

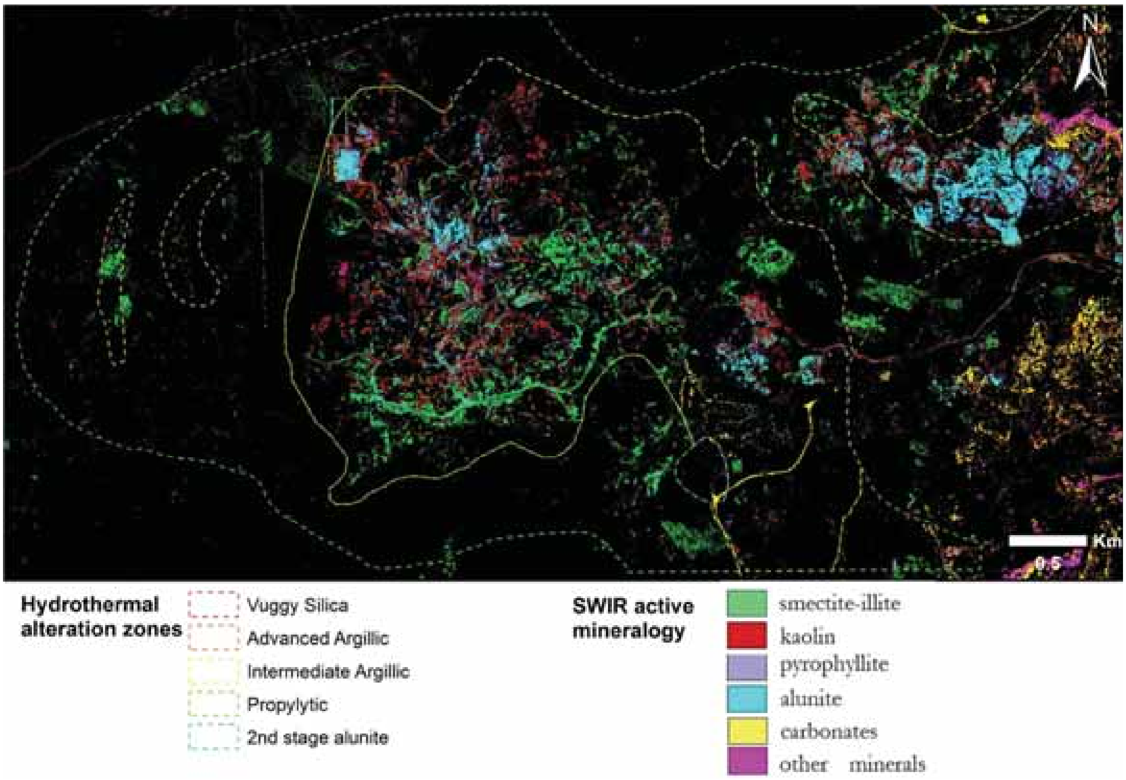

Figure 6-1: Relation of the alteration zones described by Arribas et al. (1995) with the a) general mineralogy, and *crystallinity* degree of b) smectite-illite, and c) kaolin. VG: vuggy silica, AA: advanced argillic, IA: intermediate argillic, P: Propylitic, 2al: 2nd stage alunite. For a detailed explanation of the hydrothermal alteration map see Figure 2-3.

b)

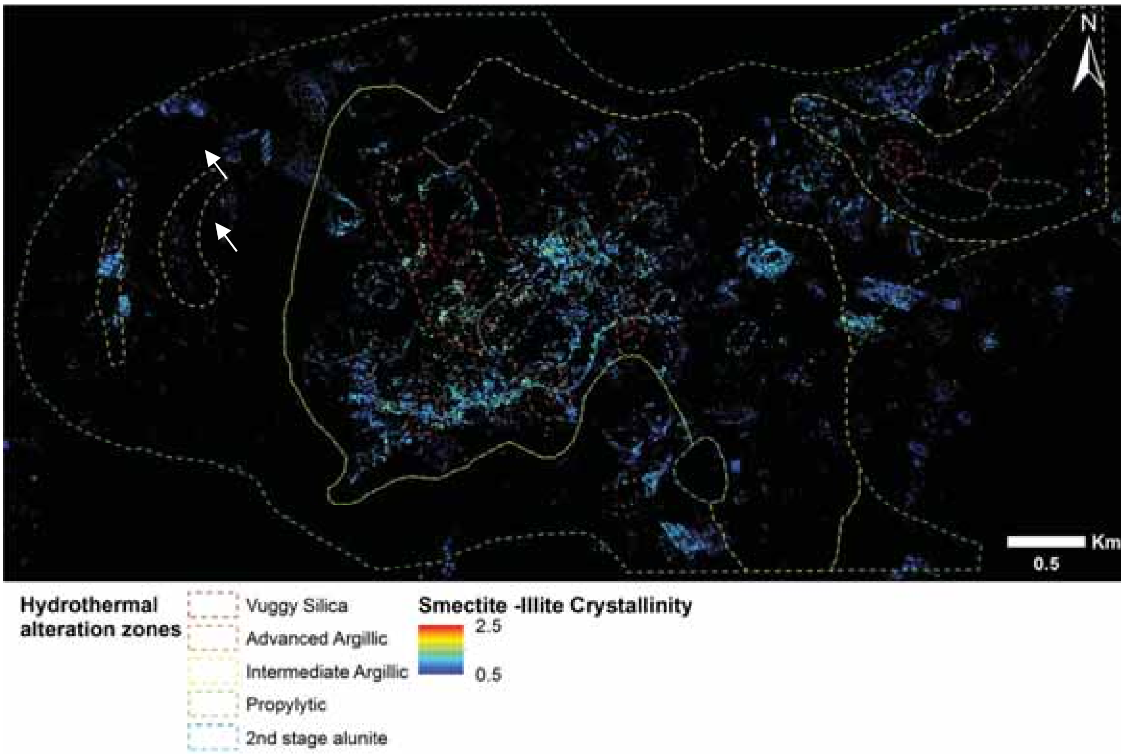

c)

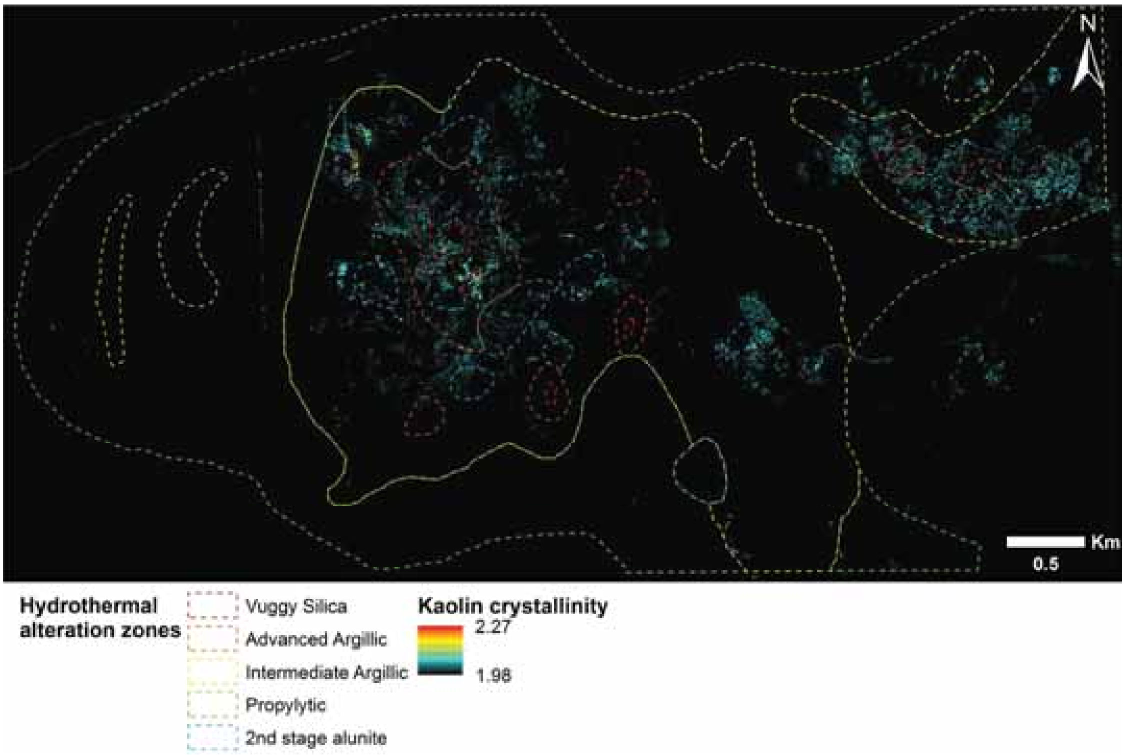

Figure 6-1 (cont): Relation of the alteration zones described by Arribas et al. (1995) with the a) general mineralogy, and *crystallinity* degree of b) smectite-illite, and c) kaolin. VG: vuggy silica, AA: advanced argillic, IA: intermediate argillic, P: Propylitic, 2al: 2nd stage alunite. For a detailed explanation of the hydrothermal alteration map see Figure 2-3.

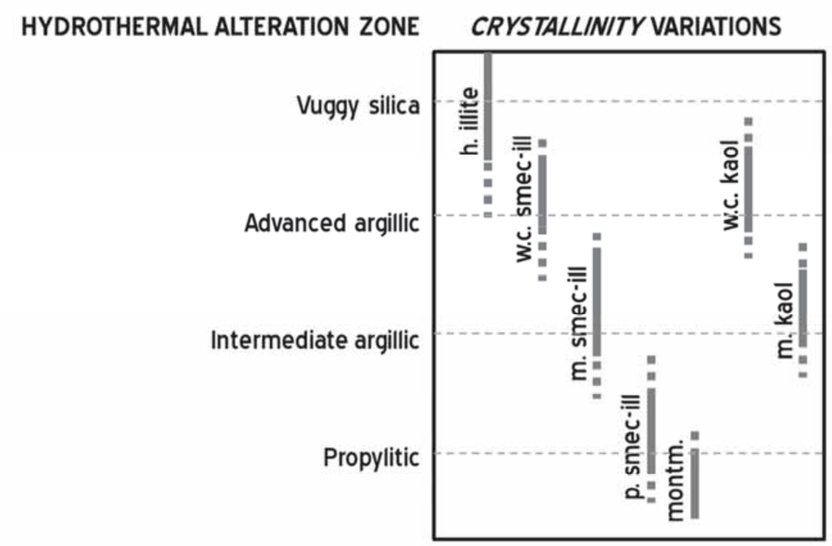

Figure 6-2: Relationship between the hydrothermal alteration zones and *crystallinity* variations in smectite-illite and kaolin minerals in the Rodalquilar caldera. **h:** highly *crystallized,* **w.c.:** well-*crystallized*, **m:** moderately-*crystallized*, **p.:** poorly-*crystallized*, **smec-ill:** smectite-illite, **montm:** montmorillonite, **kaol:** kaolinite.

Association of moderate *crystallinity* in smectite-illite and as well as in kaolin occurs around 200ºC, which would be the temperature of alteration in the intermediate argillic zone. Well-ordered structures associated with pyrophyllite and dickite point out raising temperature in the advanced argillic zone up to 250ºC, or even more. Finally, the highest *crystallinity,* especially in illites are typical of the vuggy silica zone, and represent temperatures around 300ºC. The specific mineral association of well-*crystallized* illite, abundant pyrophyillite and zunyite marks the highest temperature reached in the system about 350ºC in the Cinto area, in agreement with the results obtained with fluid inclusions by Arribas et al. (1995).

Due to the relatively small variation in composition of smectite-illite, its relation with the hydrothermal alteration zones does not show clear patterns. However in the Cinto area, where illites are interpreted well-*crystallized* and aluminium-rich, these characteristics can be compared with the chemical conditions of the advanced-argillic and vuggy-silica alteration. Aluminium enrichment is consequence of the base cations leaching in acidic pH conditions. The presence of Al-rich illite, in association with per-aluminous minerals such as pyrophyllite and zunyite is therefore evidence of the intense alteration in this part of the system.

The Cinto area, which is known as the highest-grade gold and minable zone in the Rodalquilar area (Arribas, 1995; Hernández Ortiz, 2002), with the highest smectite-illite and kaolin *crystallinity* and Al-rich minerals is therefore the area with the most intense hydrothermal alteration in the system. The interpreted temperatures as well as the chemical environment fit in the high-sulfidation classification, which widely identifies the Rodalquilar system. The Maria Josefa and Triunfo deposits with low-gold grades but higher lead/silver grades, and even the metal barren Los Tollos area, do not present the extreme conditions of temperature and pH as have been described in the Cinto area, where *crystallinity* and hence, hydrothermal temperatures are found to be lower, and there is no evidence of aluminium enrichment. As a consequence of all this, the intensity of alteration is not that strong, leading with mineralization typical of low-sulfidation systems.

The relationship between the intensity of hydrothermal alteration and the *crystallinity* degree of smectite-illite and kaolin minerals might be characteristic not only of the Rodalquilar system, but also in other similar deposits, thus providing a potential tool for characterization and exploration in epithermal systems.

7. CONCLUSIONS AND RECOMMENDATIONS

The analysis of *crystallinity* variations in smectite-illite and kaolin minerals using SWIR spectroscopy from proximal and remotely sensed sources, and the integration with other analytical techniques, applied in the Rodalquilar caldera complex lead to the following conclusions:

- Smectite-illite and kaolin minerals are variable in the structural ordering of their crystal lattice in the Rodalquilar epithermal system. These variations, named *crystallinity* changes, are a function of the water content and the position of the hydroxyl groups in the lattice, and are measurable with different techniques. In SWIR spectroscopy, either proximal or remotely sensed, the depth of the water feature at 1900nm related with the depth of the 2200nm feature gives a relative estimate of the water amount hosted in the mineral structure, and hence is and indicator of *crystallinity* degree. For smectite-illite minerals, the integration of the asymmetry of the 1400nm feature in proximal spectroscopy data enhances the *crystallinity* measurement. In the kaolin minerals the most useful parameters for measuring *crystallinity* changes are related to the absorption doublet at 2164nm. X-ray diffraction (XRD) and thermogravimetric analysis (TGA) are suitable complementary techniques to confirm these *crystallinity* variations.

- Smectite-illite group minerals have varying chemical compositions that are related to the degree of aluminium enrichment. Those compositional changes are detected by the shifting of the 2200nm feature towards shorter wavelengths when Al is increased in the minerals, and this can be well identified in proximal and remotely sensed SWIR spectroscopy. Even though there are no large compositional changes, aluminium-rich specimens are clearly identified because of the wavelength position around 2190 nm. In the Cinto area, aluminium-rich smectite-illite has also well-*crystallized* structures and its association with other per-aluminous minerals describes specific physic-chemical conditions for that area.

- *Crystallinity* variations in smectite-illite and kaolin minerals, as well as the compositional changes only in smectite-illite, are well correlated with their spatial distribution, and most important, with the intensity of the hydrothermal alteration in the Rodalquilar system. Poorly *crystalline* minerals associate with weak hydrothermal alteration and low temperatures, whereas the increasing *crystallinity* in both, smectite-illite and kaolin, is proportional to the intensification of the hydrothermal alteration. The *crystallinity* changes, interpreted together with other mineral associations led to establish 350ºC as the highest temperature in the epithermal system in the Cinto area. Despite the fact that the composition of smectite-illite tends to be relatively homogeneous, the variations towards aluminium-rich and well-*crystallized* specimens is characteristic of acidic (low pH) conditions. The integrated interpretation of *crystallinity* and compositional changes led to the identification and characterization of the mineralized areas in the Rodalquilar caldera.

- Of the different analytical techniques used for the identification of *crystallinity* changes, SWIR spectroscopy is the most suitable one. The results retrieved with this technique demonstrated to be accurate when compared with other methods. The use of spectral parameters in smectite-illite and kaolin minerals allowed a precise approach for the interpretation of features that explain the changes in structural order and composition. The most relevant drawback faced using SWIR spectroscopy was dealing with complicated mixtures of minerals with similar spectral profiles and same range for the main absorption features, which are prone to misinterpretation, as is common in the 2175-2220 nm spectral group. In this situation, TGA is the most successful technique in identification of mixtures, since the analysed properties differ considerably among mineral groups. Regarding the data acquisition, unlike TGA and XRD, the type sample preparation does not affect the spectral measurements, reducing the source of error in the retrieved data. TGA and XRD analyses entail more elaborate sample preparation and specific technical requirements that might induce variations in different sets of measurements. Particularly in this research with limited access to XRD, this fact represented the greatest disadvantage in XRD analyses.

- The increasing *crystallinity* values, particularly in smectite-illite minerals, are closely related to the gold mineralization in the Rodalquilar caldera. Illites with the most ordered structure are correlated with the zones of the most intense hydrothermal alteration and they are also surrounding the gold mineralized area in the Lomilla caldera. Asides, gold-barren systems as Los Tollos, are characterized for the absence of highly *crystalline* illites. These facts might indicate that the geological conditions under highly ordered structures in illites are formed, are the same required in the gold mineralization process. Based on this, *crystallinity* analysis particularly of smectite-illite seems to be a potential approach in gold exploration, which can be used as a vectoring tool. More detailed analysis in Los Tollos system about characterization of secondary and weathering products might confirm these observations.

Based on the results presented here above, there are some recommendations that would improve or expand this research:

- The shape of 1400nm absorption feature is a clear measure of *crystallinity* as well as a differentiation parameter of mineral mixtures only used here in proximal spectroscopy. It is recommended to include this absorption feature in the parameters used in imaging spectrometry, since its interpretation would strengthen the interpretation of *crystallinity* variations, while is a tool for mixtures definition.

- The interpretation of the *crystallinity* in kaolin minerals was limited to the well-ordered kaolinite, but changes in dickite and halloysite were so far not studied in detail in imaging spectroscopy. Analysis of *crystallinity* variations in the hyperspectral image of the kaolinite-dickite changes would complement the *crystallinity* analysis of smectite-illite, whereas variations from kaolinite to halloysite might distinguish the products of weak hydrothermal and weathering processes.

- Difficulties in the interpretation of XRD and TGA results were due to inadvertence either in the preparation of the samples or the execution of the analysis. Standardization of the laboratory measurements according with established protocols would improve enormously the results of these techniques, and as a consequence, their integration with spectroscopy data will provide increasing understanding of the spectral properties.

- Compositional and *crystallinity* variations analysed with SWIR spectroscopy in drill-cores of the Rodalquilar system would extend the 2D surface interpretation to a 3D cube that allows a complete modelling of the detected variations in the epithermal system, validating or adding valuable information about the geological processes that led to the formation of the hydrothermal system in the Rodalquilar caldera complex. Besides this, drill core information would allow the differentiation between weathering and hydrothermal alteration.

- Following the same approach regarding the spectral analysis for *crystallinity* and composition analysis in similar deposits would validate the results of this research, and at the same time it would refine this approach as a low cost tool for mineral exploration.

- New airborne hyperspectral sensors –as the AISAHAWK hyperspectral system of Specim or the HySpex spectrometer by Norsk Elektro Optic AS- are retrieving spectral data in the SWIR range with improved spatial and spectral resolution, as well as better signal to noise ratio. The recorded data quality is much better, allowing the analysis of the spectral parameters with less difficulty than in the HyMap data. Applying the same processing as proposed in this research by using newer spectral sources would improve the analysis of, for instance, doublets and asymmetry parameters, and improving at the same time the *crystallinity* analysis of the kaolin and smectite-illite minerals.

LIST OF REFERENCES

Arribas, A., 1993, Mapa geológico del distrito minero de Rodalquilar, Almería: Instituto Tecnológico GeoMinero de España, scale 1:25000.

-, 1995, Characteristics of high-sulfidation epithermal deposits, and their relation to magmatic fluids: Mineralogical Association of Canada Short Course, v. 23, p. 419-454.

Arribas, A., Cunningham, C. G., Rytuba, J. J., Rye, R. O., Kelly, W. C., Podwysocki, M. H., McKee, E. H., and Tosdal, R. M., 1995, Geology, geochronology, fluid inclusions, and isotope geochemistry of the Rodalquilar gold alunite deposit, Spain: Economic Geology and the Bulletin of the Society of Economic Geologists, v. 90, no. 4, p. 795-822.

Arribas, A. J., Rytuba, J. J., Rye, R. O., Cunningham, C. G., Podwysocki, M. H., Kelly, W. C., Arribas, A. S., McKee, E. H., and Smith, J. G., 1989, Preliminary study of the ore deposits and hydrothermal alteration in the Rodalquilar Caldera Complex, Southeastern Spain, US Geological Survey Open-File Report 89-327
report, 39 p.

Bedini, E., 2005, Mapping mineralogy in the Rodalquilar Caldera, Spain with airborne imaging spectrometer data using spectral information divergence and multiple endmember spectral mixture models [MSc Thesis]: ITC, 64 p.

Bedini, E., van der Meer, F., and van Ruitenbeek, F., 2009, Use of HyMap imaging spectrometer data to map mineralogy in the Rodalquilar caldera, southeast Spain: International Journal of Remote Sensing, v. 30, no. 2, p. 327-348.

Bish, D. L., and Duffy, C. J., 1990, Thermogravimetric analysis of minerals, *in* Stucki, J. W., Bisch, D. L., and Mumpton, F. A., eds., Thermal analysis in clay science, Volume 3, The Clay Minerals Society, p. 95-157.

Brathwaite, R. L., Christie, A. B., Faure, K., Townsend, M. G., and Terlesk, S., 2012, Origin of the Matauri Bay halloysite deposit, Northland, New Zealand: Mineralium Deposita, v. 47, no. 8, p. 897-910.

Brindley, G. W., Kao, C.-C., Harrison, J. L., Lipsicas, M., and Raythatha, R., 1986, Relation between structural disorder and other characteristics of kaolinites and dickites: Clays and Clay Minerals, v. 34, no. 3, p. 239-249.

Chororoka, K., 2012, Geochemical and spectral characterization of hydrothermal alteration facies at the epithermal gold mineralization at Rodalquilar, Spain [MSc Thesis]: University of Twente, ITC faculty, 76 p.

Clark, R. N., King, T. V. V., Klejwa, M., Swayze, G. A., and Vergo, N., 1990, High Spectral Resolution Reflectance Spectroscopy of Minerals: J. Geophys. Res., v. 95, no. B8, p. 12653-12680.

Clark, R. N., Swayze, G. A., Wise, R., Livo, K. E., Hoefen, T. M., Kokaly, R. F., and Sutley, S. J., 2007, USGS digital spectral library splib06a, *in* http://speclab.cr.usgs.gov/spectral.lib06/ds231/datatable.html,

Cocks, T., Jenssen, R., Stewart, A., Wilson, I., and Shields, T., 1998, The HyMap (TM) airborne hyperspectral sensor: The system, calibration and performance, Versailles, European Assoc Remote Sensing Laboratories, 1st Earsel Workshop on Imaging Spectroscopy, 37-42 p.

Corbett, G., 2002, Epithermal gold for explorationist: Journal of the Australian Institute of Geoscientists, p. 26.

Crowley, J. K., 1984, Near-infrared reflectance of zunyite: implications for field mapping and remote-sensing detection of hydrothermally altered high alumina rocks: Economic Geology, v. 79, no. 3, p. 553-557.

Crowley, J. K., and Vergo, N., 1988, Near-infrared reflectance spectra of mixtures of kaolin-group minerals; use in clay mineral studies: Clays and Clay Minerals, v. 36, no. 4, p. 310-316.

Cudahy, T., 1997, PIMA-II Spectral characteristics of natural kaolins, Mineral Mapping with Field Spectroscopy for Exploration, CSIRO / AMIRA, report 420R, 72 p.

Cudahy, T., Jones, M., Thomas, M., Laukamp, C., Cacceta, M., Hewson, R. D., Rodger, A., and Verall, M., 2008, Next generation mineral mapping: Queensland airborne HyMap and satellite ASTER surveys 2006-2008, report P2007/364, 93 p.

Di Battistini, G., Toscani, L., Laccarino, S., and Villa, I. M., 1987, K/Ar ages and the geological setting of calc-alkaline volcanic rocks from Sierra de Gata, SE Spain: Neues Jahrbuch fur Mineralogie, v. 8, p. 369-383.

Downs, R. T., and Hall-Wallace, M., 2003, The American Mineralogist crystal structure database: American Mineralogist, v. 88, no. 1, p. 247-250.

Duba, D., and Williams-Jones, A. E., 1983, The application of illite crystallinity, organic matter reflectance, and isotopic techniques to mineral exploration; a case study in southwestern Gaspe, Quebec: Economic Geology, v. 78, no. 7, p. 1350-1363.

Duke, E. F., 1994, Near infrared spectra of muscovite, Tschermak substitution, and metamorphic reaction progress: Implications for remote sensing: Geology, v. 22, no. 7, p. 621-624.

Ferrier, G., and Wadge, G., 1996, The application of imaging spectrometry data to mapping alteration zones associated with gold mineralization in southern Spain: International Journal of Remote Sensing, v. 17, no. 2, p. 331-350.

Grim, R. E., and Rowland, R. A., 1942, Differential thermal analysis of clay minerals and other hydrous materials. Part 1 and 2, p. 746-817.

Guggenheim, S., Alietti, A., Drits, V. A., Formoso, M. L. L., Galan, E., Koster, H. M., Paquet, H., Watanabe, T., Bain, D. C., and Hudnall, W. H., 1997, Report of the Association Internationale pour L'etude des Argiles (AIPEA) Nomenclature Committee for 1996: Clays and Clay Minerals, v. 45, no. 2, p. 298-300.

Guggenheim, S., Bain, D. C., Bergaya, F., Brigatti, M. F., Drits, V. A., Eberl, D. D., Formoso, M. L. L., Galán, E., Merriman, R. J., Peacor, D. R., Stanjek, H., and Watanabe, T., 2002, Report of the Association Internationale pour l'Etude des Argiles (AIPEA) Nomenclature Committee for 2001: Order, disorder and crystallinity in phyllosilicates and the use of the 'Crystallinity Index': Clay Minerals, v. 37, no. 2, p. 389-393.

Hauff, P., Kruse, F., Madrid, R., Fraser, S., Huntington, J., Jones, M., Watters, S., and Environm Res Inst, M., 1991, Illite crystallinity - case-histories using x-ray-diffraction and reflectance spectroscopy to define ore host environments: Proceedings of the Eighth Thematic Conference on Geologic Remote Sensing : Exploration, Engineering, and Environment Vols 1 and 2, p. 447-458.

Hauff, P. L., Kruse, F. A., and Madrid, R. J., 1989, Gold exploration using illite polytypes defined by X-ray diffraction and reflectance spectroscopy, Gold Forum on Technology and Practices - 'World Gold '89' p. 76-82.

Hauff, P. L., Kruse, F. A., and Thiry, M., 1990, Characterization of interstratified kaolinite/smectite clays using infrared reflectance spectroscopy (1.2 – 2.5 µm): Chemical Geology, v. 84, no. 1–4, p. 267-270.

Hedenquist, J. W., Arribas, A., and Gonzalez-Urien, E., 2000, Exploration for Epithermal Gold Deposits, Reviews in Economic Geology, Volume 13, Society of Economic Geologist, p. 245-277.

Hedenquist, J. W., and Henley, R. W., 1985, The importance of CO 2 on freezing point measurements of fluid inclusions; evidence from active geothermal systems and implications for epithermal ore deposition: Economic Geology, v. 80, no. 5, p. 1379-1406.

Henley, R. W., 1985, The geothermal framework of epithermal deposits, *in* Berger, B. R., and Bethke, P. M., eds., Geology and Geochemistry of epithermal systems, Volume 2, Society of Economic Geologists, p. 1-24.

Hernández Ortiz, F., 2002, El oro y las minas de Rodalquilar, años 1509-1990, Madrid, Junta de Andalucía, Consejería de Medio Ambiente, 236 p.

Hinckley, D. N., Variability in "crystallinity" values among the kaolin deposits of the coastal plain of georgia and south carolina, *in* Proceedings Clays and Clay Minerals, Proc. 11th Natl. Conf. , Ottawa, Ontario, 1963, Pergamon Press, p. 229-235.

Hunt, G. R., 1977, Spectral signatures of particulate minerals in visible and near IR: Geophysics, v. 42, no. 3, p. 501-513.

Hunt, G. R., and Ashley, R. P., 1979, Spectra of altered rocks in the visible and near infrared: Economic Geology, v. 74, no. 7, p. 1613-1629.

Kruse, F. A., and Hauff, P. L., 1991, Identification of illite polytype zoning in disseminated gold deposits using reflectance spectroscopy and X-ray diffraction-potential for mapping with imaging spectrometers: Geoscience and Remote Sensing, IEEE Transactions on, v. 29, no. 1, p. 101-104.

Kubler, B., and Jaboyedoff, M., 2000, Illite crystallinity: Comptes Rendus De L Academie Des Sciences Serie Ii Fascicule a-Sciences De La Terre Et Des Planetes, v. 331, no. 2, p. 75-89.

López Ruiz, J., and Rodríguez-Badiola, E., 1980, La Region Volcánica Neogena del Sureste de España: Estudios Geologicos, v. 36, p. 63.

Meyer, C., and Hemley, J. j., 1967, Wall rock alteration, *in* Barnes, H. L., ed., Geochemistry of hydrothermal ore deposits: New York, Rinehart and Winston Holt, p. 166-235.

Muffler, P., and White, D., 1969, Active Metamorphism of Upper Cenozoic Sediments in the Salton Sea Geothermal Field and the Salton Trough, Southeastern California: Geological Society of America Bulletin, v. 80, no. 2, p. 157-182.

Pirajno, F., 1992, Hydrothermal mineral deposits : principles and fundamental concepts for the exploration geologist, Berlin etc., Springer-Verlag, 709 p.

Pirajno, F., 2008, Porphyry systems; fossil and active epithermal systems, Hydrothermal processes and mineral systems: DE, Springer Verlag, p. 355-533.

Pontual, S., Merry, N., and Gamson, P., 1997, Spectral Analysis Guides for Mineral Exploration G-MEX, v. 1-8.

Post, J. L., and Noble, P. N., 1993, The near-infrared combination band frequencies of dioctahedral smectites, micas, and illites: Clays and Clay Minerals, v. 41, no. 6, p. 639-644.

Reyes, A. G., 1990, Petrology of Philippine geothermal systems and the application of alteration mineralogy to their assessment: Journal of Volcanology and Geothermal Research, v. 43, no. 1–4, p. 279-309.

Rieder, M., Cavazzini, G., D'Yakonov, Y. S., Frank-Kamenetskii, V. A., Gottardi, G., Guggenheim, S., Koval, P. V., Muller, G., Neiva, A. M. R., Radoslovich, E. W., Robert, J. L., Sassi, F. P., Takeda, H., Weiss, Z., and Wones, D. R., 1998, Nomenclature of the micas: American Mineralogist, v. 83, no. 11-12, p. 1366-1366.

Rodger, A., Laukamp, C., Haest, M., and Cudahy, T., 2012, A simple quadratic method of absorption feature wavelength estimation in continuum removed spectra: Remote Sensing of Environment, v. 118, no. 0, p. 273-283.

Rytuba, J. J., Arribas, A., Cunningham, C. G., McKee, E. H., Podwysocki, M. H., Smith, J. G., and Kelly, W. C., 1990, Mineralized and unmineralized calderas in Spain 2. Evolution of the Rodalquilar caldera complex and associated gold-alunite deposits: Mineralium Deposita, v. 25, p. S29-S35.

Saenger-van Oepen, P., Friedrich, G., and Vogt, J. H., 1989, Fluid evolution, wallrock alteration, and ore mineralization associated with the Rodalquilar epithermal gold-deposit in Southeast Spain: Mineralium Deposita, v. 24, no. 4, p. 235-243.

Serratosa, J. M., and Bradley, W. F., 1958, Determination of the Orientation of OH Bond Axes in Layer Silicates by Infrared Absorption: The Journal of Physical Chemistry, v. 62, no. 10, p. 1164-1167.

Sillitoe, R., and Hedenquist, J. W., 2003, Linkages between volcanotectonic settings, ore-fluid compositions, and epithermal precious metal deposits, *in* Simmons, S. F., ed., Special Publication: Understanding Crustal Fluids: Roles and Witnesses of Processes Deep Within the Earth, Volume 10, Society of Economic Geologist, p. 1-29.

Steiner, A., 1968, Clay minerals in hydrothermally altered rocks at Wairakei, New Zealand: Clays and Clay Minerals, v. 16, p. 193-213.

Stubican, V., and Roy, R., 1961, Isomorphous substitution and infra-red spectra of the layer lattice silicates: American Mineralogist, v. 46, no. 1-2, p. 32-51.

Thompson, A. J. B., Hauff, P. L., and Robitaille, A. J., 1999, Alteration mapping in exploration: Aplication of Short-Wave infrared (SWIR Spectroscopy), SEG Newsletter, Volume 39, p. 16-27.

Toscani, L., Venturelli, G., Barbieri, M., Capedri, S., Fernandez Soler, J. M., and Oddone, M., 1990, Geochemistry and petrogenesis of two-Pyroxene andesites from Sierra de Gata (SE Spain): Mineralogy and Petrology, v. 41, no. 2, p. 199-213.

Tuddenham, W. M., and Lyon, R. J. P., 1960, Infrared techniques in the identification and measurement of minerals: Analytical Chemistry, v. 32, no. 12, p. 1630-1634.

van Ruitenbeek, F. J. A., Cudahy, T., Hale, M., and van der Meer, F. D., 2005, Tracing fluid pathways in fossil hydrothermal systems with near-infrared spectroscopy: Geology, v. 33, no. 7, p. 597-600.

Velde, B., 1977, Proposed phase-diagram for illite, expanding chlorite, corrensite and illite-montmorillonite mixed layered minerals: Clays and Clay Minerals, v. 25, no. 4, p. 264-270.

Yoder, H. S., and Eugster, H. P., 1955, Synthetic and natural muscovites: Geochimica et Cosmochimica Acta, v. 8, no. 5–6, p. 225-280.

APPENDICES

Appendix 1: Rock and ground spectra location and spectral files

The complete database that includes the stations, location and spectral files of the ground data, as well as station, location, sample names, rock description, photographic record and spectral files of the laboratory data is attached in the digital version of this document.

Appendix 2: Syntax of functions used in HypPy software for the extraction of spectral parameters in the spectral libraries and in the HyMap scene

Parameter	**Syntax***	**Retrieved information/Description**
Spectral Library		
1400W	S[1010:1110].minwav(1)	Wavelength and depth of the deepest absorption feature in the specified range
1400D		
1400AS	S[1010:1110].peaks().asymmetry(1)	Asymmetry measured at the FWHM of the specified range
1700W	S[1330:1530].minwav(1)	Wavelength and depth of the deepest absorption feature in the specified range
1700D		
1900D	S[1500:1700].minwav(1)	Wavelength and depth of the deepest absorption feature in the specified range. Only the depth parameter is taken
2100-2500W	S[1750:2150].minwav(1)	Wavelength and depth of the deepest absorption feature in the specified range. Only the wavelength parameter is taken
2200W	S[1825:1870].minwav(1)	Wavelength and depth of the deepest absorption feature in the specified range.
2200D		
2200AS	S[1825:1870].peaks().asymmetry(1)	Asymmetry measured at the FWHM of the specified range
2160D, 2177D, 2184D, 2190D	1-(S[1810,1827,1834,1840])	Depth of the specified bands or wavelengths
HyMap Scene		
NDVI	(i1(0.860)-i1(0.687))/ (i1(0.860)+i1(0.687))	Abundance and distribution of green vegetation
1900D	((1-i1[20])+(((2.0652-1.9150)*((1-i1[14])-(1-i1[20])))/(2.0652-1.9531)))	Extrapolated depth of the 1.900 μm water feature
2200D/1900D	(i1[2])/(i2[0])	i1[2] = interpolated depth band from the wavelength of minimum image i2[0] = *1900D* image (single band)
Smectite-illite and kaolinite filter 1	(i1(2.318)+i1(2.295)+i1(2.369))/(i1(2.333) +i1(2.350)+i1(2.366))	Smectite-illite or kaolinite, depending the threshold
Smectite-illite and kaolinite filter 2	(i1(2.138)+i1(2.190))/(i1(2.156))	Smectite-illite or kaolinite, depending the threshold
Kaolin crystallinity	(i1(2.138)+i1(2.190))/(i1(2.156))	Kaolinite crystallinity

*S = spectral library, i = image, (####) = wavelength, [###] =band number, starting from 0

Equivalency between band number and wavelength for the ASD spectrometer and HyMap sensor:

ASD Band	Wavelength (nm)
1010	1360
1110	1460
1330	1680
1500	1800
1530	1860
1700	2050
1750	2100
1810	2160
1825	2175
1827	2177
1834	2184
1840	2190
1870	2220
2150	2500

HyMap band	Wavelength (μm)
17	0.687
29	0.860
95	1.953
101	2.065
105	2.138
106	2.156
108	2.190
114	2.295
116	2.318
118	2.366

Appendix 3: Results of laboratory SWIR analysis for Smectite-Illite crystallinity

Absorption parameters and SWIR smectite-illite *crystallinity* values. Only results of the subset of powdered samples used in other analytical methods and rock samples used for HyMap validation are shown. The complete table including all the measurements used is attached in the digital version of this document.

	1400 nm			**1900 nm**	**2200 nm**			**SWIR smectite-illite *crystallinity***	
Sample (powder)	***1400W***	***1400D***	***1400AS***	***1900D***	***2200W***	***2200D***	***2220AS***	***2200D/1900D***	***(1+1400AS)* (2200D/1900D)***
Powder samples									
04MRE141	1408	0.102	0.086	0.116	2195	0.129	-0.057	1.112	1.208
Mex 1-001-PM2	1410	0.269	0.136	0.181	2200	0.290	0.068	1.602	1.820
MRE-02-033 PM1	1412	0.171	0.103	0.199	2209	0.177	0.074	0.889	0.981
MRE-01-006 PM1	1411	0.054	0.033	0.092	2211	0.083	0.133	0.902	0.932
MRE-01-008 PM1	1412	0.119	0.097	0.146	2210	0.125	0.058	0.856	0.939
04MRE 129	1413	0.152	-0.017	0.256	2209	0.162	0.043	0.633	0.622
04MRE 146	1413	0.136	-0.007	0.193	2212	0.143	0.071	0.741	0.736
04 MRE 123	1412	0.198	0.004	0.290	2209	0.160	0.150	0.552	0.554
04MRE 027 PIMA	1413	0.471	0.004	0.635	2207	0.239	0.150	0.376	0.378
Rock samples									
04MRE005 P.013	1395	0.128	0.032	0.407	2209	0.214	0.072	0.526	0.543
04MRE027 PIMA	1411	0.363	0.055	0.662	2206	0.248	0.223	0.375	0.395
P.021-04MRE044	1410	0.184	0.048	0.355	2202	0.190	0.188	0.535	0.561
04MRE048 (2)	1412	0.084	-0.009	0.201	2205	0.103	0.271	0.512	0.508
04MRE051	1410	0.190	-0.026	0.348	2200	0.243	0.104	0.698	0.680
04MRE053	1413	0.095	0.061	0.156	2205	0.168	0.227	1.077	1.143
04MRE123	1411	0.220	0.016	0.426	2203	0.217	0.170	0.509	0.517
04MRE129	1411	0.181	0.067	0.358	2205	0.217	0.272	0.606	0.647

	1400 nm			1900 nm	2200nm			SWIR smectite-illite crystallinity	
Sample (rock)	***1400W***	***1400D***	***1400AS***	***1900D***	***2200W***	***2200D***	***2200AS***	***2200D/1900D***	***(1+1400AS)* (2200D/1900D)***
04MRE137	1411	0.147	0.029	0.27	2205	0.187	0.244	0.693	0.713
04MRE138	1411	0.208	0.062	0.351	2205	0.233	0.252	0.664	0.705
04MRE140	1410	0.196	-0.018	0.341	2200	0.232	0.051	0.680	0.668
04MRE141	1408	0.139	0.077	0.189	2197	0.222	0.018	1.175	1.265
04MRE142	1412	0.205	-0.018	0.366	2205	0.237	0.209	0.648	0.636
04MRE144	1413	0.154	0.008	0.353	2204	0.248	0.092	0.703	0.708
04MRE145	1411	0.142	-0.020	0.272	2205	0.187	0.230	0.688	0.674
04MRE146	1412	0.215	-0.002	0.402	2204	0.248	0.101	0.617	0.616
04MRE227a	1412	0.168	0.087	0.341	2205	0.174	0.231	0.510	0.554
Mex1-pm2	1410	0.189	0.038	0.22	2199	0.242	0.063	1.100	1.141
MRE01005pm1	1412	0.209	0.082	0.306	2205	0.249	0.213	0.814	0.880
MRE01006pm1	1412	0.082	-0.020	0.176	2206	0.134	0.234	0.761	0.746
MRE01008pm1	1410	0.127	-0.005	0.257	2206	0.163	0.210	0.634	0.631
MRE01014pm1	1411	0.280	0.089	0.441	2205	0.323	0.271	0.732	0.797
MRE01016pm1	1412	0.153	-0.025	0.292	2206	0.197	0.141	0.675	0.658
MRE01048pm	1411	0.233	0.083	0.373	2205	0.260	0.238	0.697	0.755
MRE01070pm2	1410	0.262	-0.019	0.362	2200	0.303	0.021	0.837	0.821
MRE01084pm5	1412	0.142	-0.040	0.294	2203	0.173	0.073	0.588	0.565
MRE03024pm	1412	0.135	0.083	0.212	2205	0.152	0.230	0.717	0.776
MRE03027pm	1413	0.064	-0.013	0.139	2206	0.091	0.112	0.658	0.649
05ch093	1411	0.225	0.079	0.348	2205	0.258	0.279	0.741	0.800
05ch100	1412	0.054	-0.030	0.148	2207	0.090	0.168	0.610	0.592
05ch101	1412	0.157	0.054	0.269	2206	0.206	0.130	0.766	0.807
06ch124	1413	0.108	-0.201	0.413	2207	0.207	0.271	0.501	0.400
06ch127	1409	0.186	0.019	0.365	2196	0.275	-0.037	0.753	0.768
06ch149	1413	0.273	0.366	0.490	2207	0.336	0.156	0.686	0.937
06ch164	1413	0.266	0.275	0.404	2207	0.291	0.192	0.720	0.918

	1400 nm			**1900 nm**	**2200nm**			**SWIR smectite-illite crystallinity**	
Sample (rock)	***1400W***	***1400D***	***1400AS***	***1900D***	***2200W***	***2200D***	***2200AS***	***2200D/1900D***	***(1+1400AS)* (2200D/1900D)***
06ch167	1408	0.230	-0.026	0.364	2195	0.300	0.028	0.824	0.803
06ch202	1413	0.169	0.177	0.337	2207	0.193	0.224	0.573	0.674
06ch203	1407	0.148	0.058	0.189	2193	0.207	0.079	1.095	1.159
jk06001	1413	0.217	0.237	0.423	2207	0.273	0.142	0.645	0.798
jk06100	1412	0.244	0.315	0.435	2206	0.304	0.172	0.699	0.919
jk06102	1407	0.255	0.063	0.340	2192	0.317	-0.034	0.932	0.991
jk06108	1410	0.179	-0.032	0.293	2203	0.212	-0.003	0.724	0.700
jk06109	1410	0.145	-0.011	0.272	2206	0.179	0.184	0.658	0.651
jk06110	1410	0.161	-0.003	0.301	2205	0.202	0.066	0.671	0.669
jk06114	1409	0.216	0.023	0.365	2199	0.263	-0.056	0.721	0.737

Appendix 4: Results of laboratory SWIR analysis for Kaolin crystallinity

Absorption parameters and SWIR smectite-illite *crystallinity* values. Only results of the subset of powdered samples used in other analytical methods and rock samples used for HyMap validation are shown. The complete table including all the measurements used is attached in the digital version of this document.

	1400 nm			**1900 nm**	**2200 nm**			**Crystallinity parameters**				**Kaolin crystallinity**			
Sample (powder)	***1400W***	***1400D***	***1400AS***	***1900D***	***2200W***	***2200D***	***2200AS***	***2160D***	***2177D***	***2184D***	***2190D***	***2200D/ 1900D***	***2160D/ 2177D***	***2184D/ 2190D***	***KX***
Powder samples															
MRE 01013 PM1	1414	0.131	0.034	0.079	2206	0.093	0.041	0.078	0.160	0.162	0.140	1.190	0.491	1.159	1.219
MRE 02-023	1413	0.176	0.470	0.185	2208	0.170	0.178	0.169	0.165	0.169	0.186	0.917	1.023	0.907	0.969
04MRE 139	1412	0.169	0.424	0.236	2207	0.140	0.095	0.116	0.130	0.140	0.158	0.592	0.891	0.882	1.010
04 MRE 136	1413	0.114	0.423	0.122	2207	0.092	0.151	0.080	0.090	0.101	0.117	0.757	0.881	0.862	1.005
04 MRE 228	1413	0.077	0.450	0.109	2207	0.083	0.175	0.067	0.085	0.093	0.102	0.765	0.787	0.906	1.029
Q2-6	1413	0.105	0.434	0.149	2208	0.091	0.246	0.090	0.097	0.102	0.114	0.613	0.923	0.899	1.004
04MRE 140	1412	0.198	0.162	0.393	2207	0.113	0.308	0.127	0.173	0.192	0.211	0.287	0.737	0.909	1.086
MRE01010	1412	0.154	0.359	0.186	2207	0.105	0.144	0.079	0.097	0.113	0.135	0.561	0.813	0.842	1.016
Rock samples															
04MRE008 S.017	1412	0.188	0.404	0.285	2208	0.247	0.157	0.167	0.164	0.160	0.167	0.867	1.018	0.958	0.984
04MRE051	1412	0.190	0.398	0.360	2207	0.299	0.190	0.139	0.157	0.161	0.193	0.831	0.885	0.834	1.003
04MRE052	1412	0.232	0.326	0.440	2207	0.307	0.220	0.142	0.167	0.172	0.208	0.698	0.850	0.827	1.015
04MRE054	1413	0.146	0.410	0.257	2207	0.220	0.197	0.100	0.114	0.118	0.143	0.856	0.877	0.825	1.002
04MRE055	1412	0.209	0.249	0.295	2207	0.264	0.272	0.089	0.125	0.135	0.179	0.895	0.712	0.754	1.029
04MRE122	1412	0.289	0.415	0.279	2207	0.396	0.175	0.279	0.275	0.273	0.302	1.419	1.015	0.904	0.947
04MRE127	1412	0.257	0.416	0.196	2208	0.333	0.211	0.246	0.234	0.231	0.249	1.699	1.051	0.928	0.945
04MRE130	1412	0.159	0.220	0.286	2207	0.210	0.279	0.070	0.100	0.108	0.143	0.734	0.703	0.755	1.025
04MRE133	1412	0.303	0.416	0.361	2207	0.399	0.229	0.290	0.283	0.282	0.302	1.105	1.025	0.934	0.952

	1400 nm			**1900 nm**	**2200 nm**			**Crystallinity parameters**				**Kaolin crystallinity**			
Sample (rock)	***1400W***	***1400D***	***1400AS***	***1900D***	***2200W***	***2200D***	***2200AS***	***2160D***	***2177D***	***2184D***	***2190D***	***2200D/ 1900D***	***2160D/ 2177D***	***2184D/ 2190D***	***KX***
04MRE139	1413	0.229	0.469	0.376	2208	0.335	0.184	0.171	0.180	0.182	0.211	0.891	0.950	0.863	0.985
04MRE143	1413	0.228	0.368	0.358	2207	0.325	0.104	0.167	0.165	0.167	0.201	0.908	1.012	0.831	0.95
04MRE223	1413	0.173	0.380	0.262	2207	0.257	0.106	0.116	0.121	0.125	0.156	0.981	0.959	0.801	0.975
04MRE225a	1412	0.224	0.331	0.308	2207	0.305	0.259	0.126	0.164	0.172	0.216	0.990	0.768	0.796	1.035
04MRE227	1412	0.236	0.296	0.416	2207	0.310	0.139	0.121	0.138	0.144	0.188	0.745	0.877	0.766	0.985
04MRE228	1413	0.255	0.509	0.332	2207	0.383	0.118	0.250	0.256	0.255	0.272	1.154	0.977	0.938	0.993
AQ1-Q1-3	1413	0.117	0.499	0.208	2208	0.213	0.211	0.103	0.107	0.108	0.131	1.024	0.963	0.824	0.982
AQ2-Q2-5	1413	0.238	0.496	0.136	2208	0.312	0.163	0.217	0.230	0.228	0.232	2.294	0.943	0.983	1.029
MRE01004pm1	1413	0.096	0.349	0.209	2208	0.204	0.162	0.093	0.108	0.110	0.130	0.976	0.859	0.846	1.011
MRE01010pm1	1412	0.154	0.359	0.186	2207	0.200	0.144	0.078	0.093	0.098	0.129	1.075	0.835	0.760	0.998
MRE01012pm1	1412	0.181	0.336	0.315	2207	0.274	0.179	0.111	0.129	0.135	0.174	0.870	0.860	0.776	0.994
MRE01015pm1	1413	0.097	0.336	0.159	2208	0.131	0.120	0.060	0.067	0.067	0.079	0.824	0.900	0.854	1.002
MRE01027pm	1413	0.324	0.508	0.364	2208	0.434	0.135	0.344	0.330	0.324	0.329	1.192	1.042	0.985	0.951
MRE01050pm	1412	0.240	0.226	0.354	2206	0.297	0.244	0.094	0.140	0.153	0.207	0.839	0.674	0.739	1.038
MRE01055pm	1413	0.238	0.261	0.415	2207	0.260	0.246	0.117	0.147	0.153	0.187	0.627	0.796	0.818	1.029
MRE01057pm	1413	0.166	0.326	0.344	2207	0.229	0.167	0.110	0.128	0.131	0.155	0.666	0.859	0.845	1.013
MRE01060pm	1412	0.143	0.191	0.250	2207	0.165	0.297	0.064	0.093	0.098	0.122	0.660	0.692	0.803	1.036
MRE01061pm	1413	0.093	0.323	0.204	2208	0.156	0.199	0.062	0.067	0.068	0.086	0.765	0.925	0.795	0.991
MRE01088pm	1413	0.011	0.063	0.144	2203	0.058	0.174	0.043	0.049	0.050	0.054	0.402	0.866	0.935	1.010
MRE01091pm	1412	0.091	0.331	0.140	2207	0.090	0.245	0.040	0.052	0.054	0.066	0.642	0.759	0.824	1.014
MRE02023pm1	1413	0.183	0.453	0.234	2208	0.289	0.191	0.177	0.170	0.170	0.192	1.235	1.041	0.885	0.956
MRE02024pm1	1413	0.157	0.419	0.249	2208	0.231	0.120	0.150	0.149	0.147	0.157	0.928	1.007	0.936	0.986
MRE02025pm1	1413	0.148	0.171	0.326	2208	0.149	0.241	0.063	0.077	0.079	0.095	0.457	0.822	0.834	1.012
MRE02033pm1	1412	0.191	0.199	0.295	2207	0.241	0.254	0.072	0.111	0.120	0.161	0.817	0.651	0.745	1.038
MRE02034pm1	1412	0.175	0.263	0.231	2207	0.227	0.287	0.081	0.111	0.120	0.158	0.983	0.732	0.759	1.022
MRE03021pm	1413	0.192	0.490	0.194	2207	0.311	0.122	0.169	0.173	0.174	0.202	1.603	0.977	0.861	0.975
MRE03022pm	1413	0.155	0.350	0.320	2207	0.176	0.090	0.080	0.078	0.079	0.098	0.550	1.024	0.801	0.974

	1400 nm			**1900 nm**	**2200 nm**			**Crystallinity parameters**				**Kaolin crystallinity**			
Sample (rock)	***1400W***	***1400D***	***1400AS***	***1900D***	***2200W***	***2200D***	***2200AS***	***2160D***	***2177D***	***2184D***	***2190D***	***2200D/ 1900D***	***2160D/ 2177D***	***2184D/ 2190D***	***KX***
MRE03025pm	1413	0.103	0.355	0.183	2207	0.135	0.201	0.048	0.058	0.061	0.081	0.738	0.830	0.757	1.000
TES 05ch064	1413	0.211	0.437	0.287	2207	0.316	0.153	0.172	0.183	0.186	0.215	1.101	0.940	0.865	0.990
04MRE008S.016	1414	0.267	0.142	0.098	2207	0.347	-0.010	0.222	0.311	0.314	0.275	3.534	0.714	1.142	1.312
04MRE013	1414	0.198	-0.005	0.165	2208	0.287	0.001	0.164	0.258	0.258	0.216	1.739	0.636	1.194	1.307
04MRE120	1414	0.313	0.567	0.111	2207	0.364	0.030	0.246	0.333	0.335	0.298	3.279	0.739	1.124	1.314
MRE01013pm1	1414	0.223	0.001	0.078	2208	0.285	0.001	0.164	0.270	0.270	0.216	3.654	0.607	1.250	1.359
MRE02032pm1	1414	0.293	0.017	0.121	2208	0.366	0.016	0.239	0.357	0.356	0.294	3.025	0.669	1.211	1.455
MRE02035pm1	1414	0.316	0.173	0.219	2207	0.390	0.042	0.254	0.358	0.363	0.319	1.781	0.709	1.138	1.389
MRE03023pm	1414	0.276	-0.001	0.218	2207	0.367	0.073	0.219	0.332	0.335	0.287	1.683	0.660	1.167	1.406
MRE03056	1414	0.359	0.573	0.074	2208	0.454	0.059	0.316	0.409	0.409	0.365	6.177	0.773	1.121	1.384

Appendix 5: Samples selected for validation and detailed analytical methods and nomenclature of the corresponding raw files

Sample	ASD_rock	ASD_powder	XRD	TGA	Mineral group
04MRE141	Rod00205	Rod-p_00001	XRD1	NA	smectite - illite
Mex 1-001-PM2	Rod00320	Rod-p_00002	XRD2	Mex 1-001-PM2	smectite - illite
MRE-02-033 PM1	Rod00519	Rod-p_00003	XRD3	NA	smectite - illite
MRE-01-006 PM1	Rod00344	Rod-p_00004	XRD4	NA	smectite - illite
MRE-01-008 PM1	Rod00352	Rod-p_00006	XRD5	NA	smectite - illite
04MRE 129	Rod00180	Rod-p_00007	XRD6	NA	smectite - illite
04MRE 146	Rod00221	Rod-p_00008	XRD7	NA	smectite - illite
04 MRE 123	Rod00162	Rod-p_00009	XRD8	NA	smectite - illite
04MRE 027 PIMA	Rod00064	Rod-p_00011	XRD9	04MRE 027 PIMA	smectite - illite
MEX 1-PM4	Rod00325	Rod-p_00012	XRD10	MEX 1-PM4	zunyite
04MRE 004(3) PIMA 002 C	Rod00016	Rod-p_00013	XRD11	NA	sulphate (alunite)
04MRE AQ 1-3	Rod00268	Rod-p_00014	XRD12	NA	sulphate (alunite)
MRE 01013 PM1	Rod00369	Rod-p_00015	XRD13	MRE 01013 PM1	kaolin
MRE 02-023 PM1	Rod00488	Rod-p_00016	XRD14	MRE 02-023 PM1	kaolin
04MRE 139	Rod00199	Rod-p_00017	XRD15	04MRE 139	kaolin
04 MRE 136	Rod00190	Rod-p_00018	XRD16	04 MRE 136	kaolin
04 MRE 228	Rod00248	Rod-p_00019	XRD17	04 MRE 228	kaolin
Q2-6	Rod00310	Rod-p_00020	XRD18	Q2-6	kaolin
04MRE 140	Rod00203	Rod-p_00021	XRD19	04MRE 140	kaolin
MRE01010	Rod00358	Rod-p_00022	XRD20	MRE01010	kaolin

NA = not analysed

Appendix 6: Results of XRD analysis: diffractograms and extracted peaks

XRD DIFFRACTOGRAMS

XRD PEAKS

XRD 1

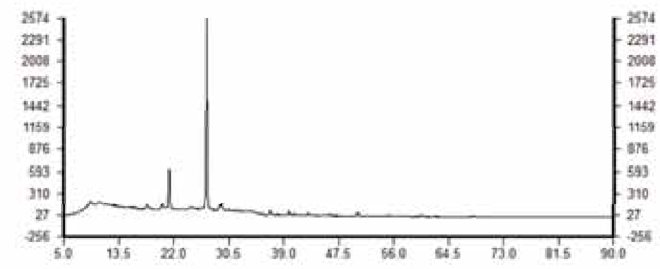

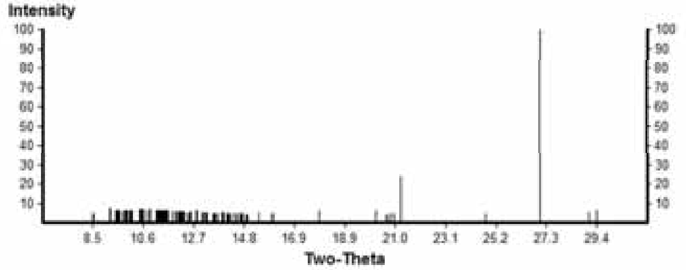

XRD 2

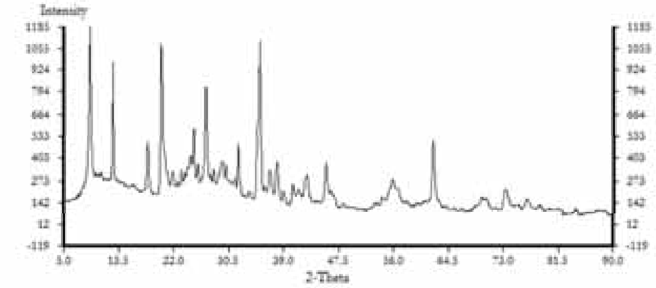

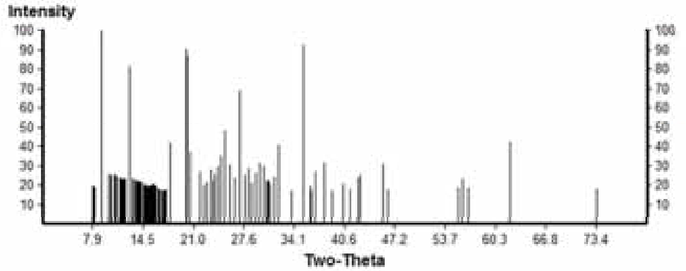

XRD 3

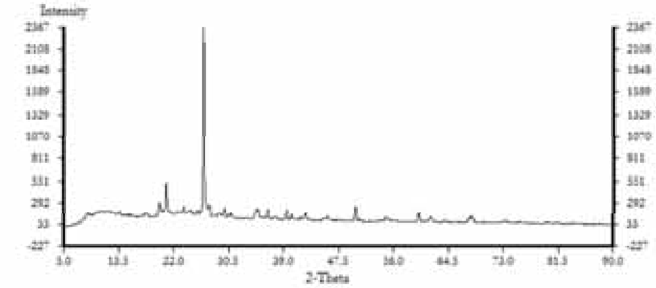

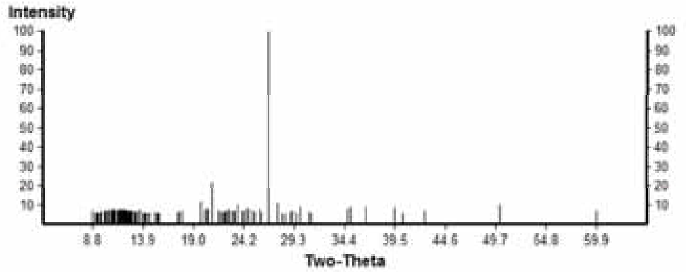

XRD 4

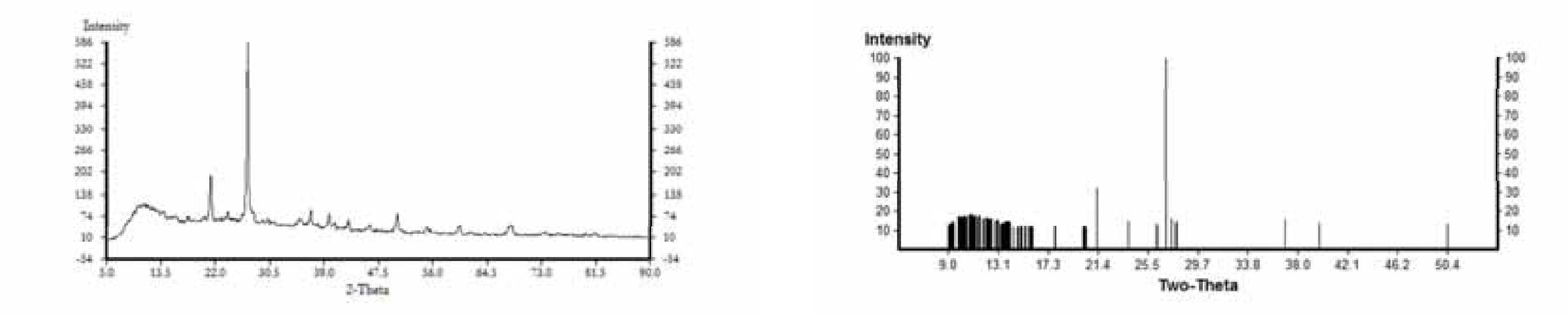

XRD 5

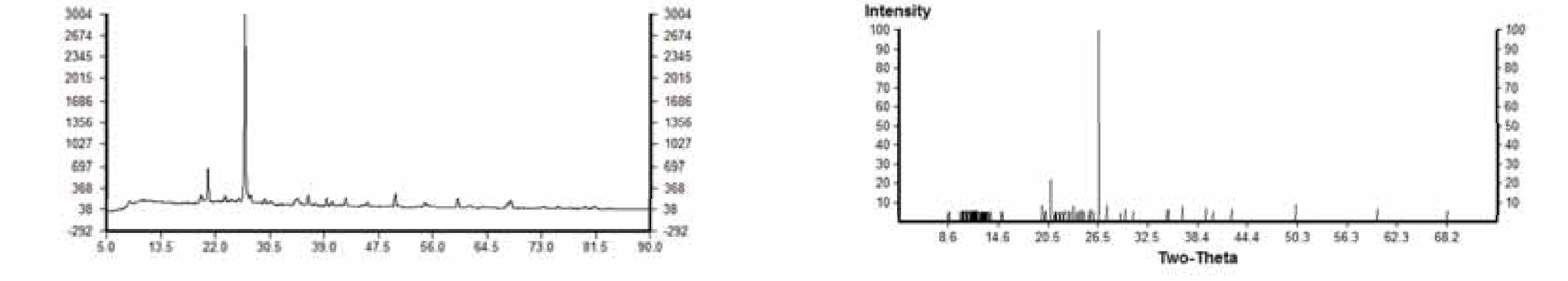

XRD 6

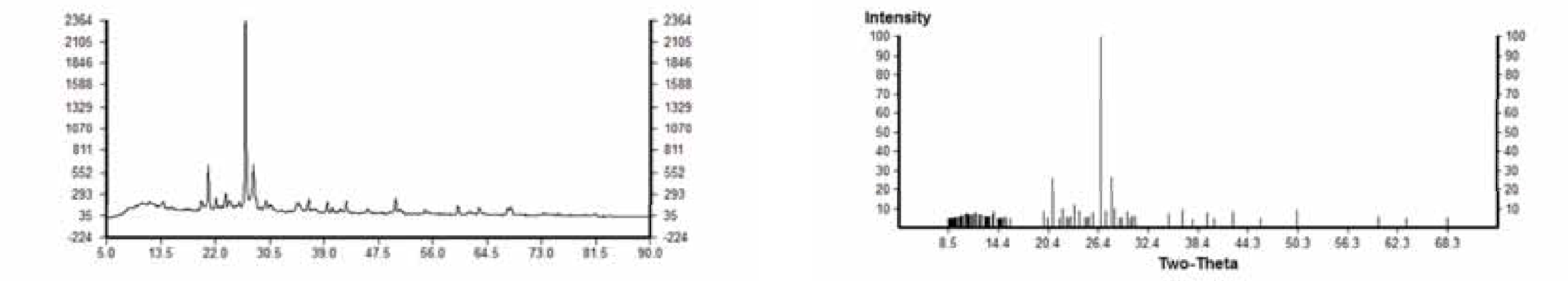

XRD 7

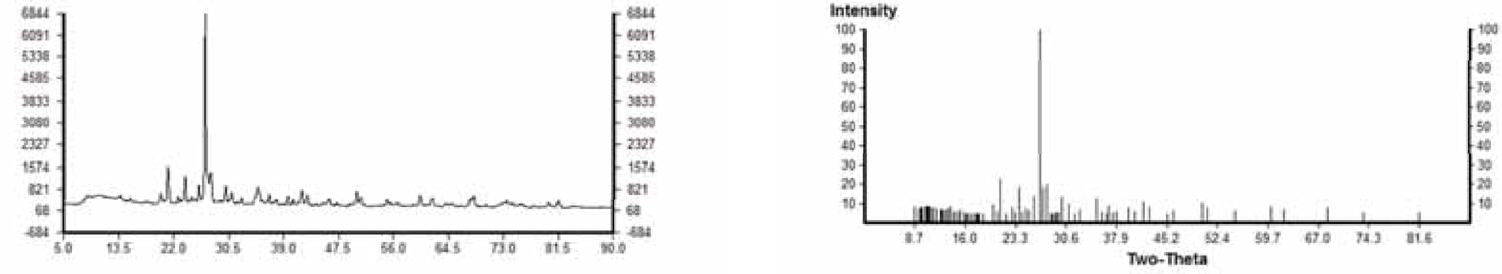

XRD 8

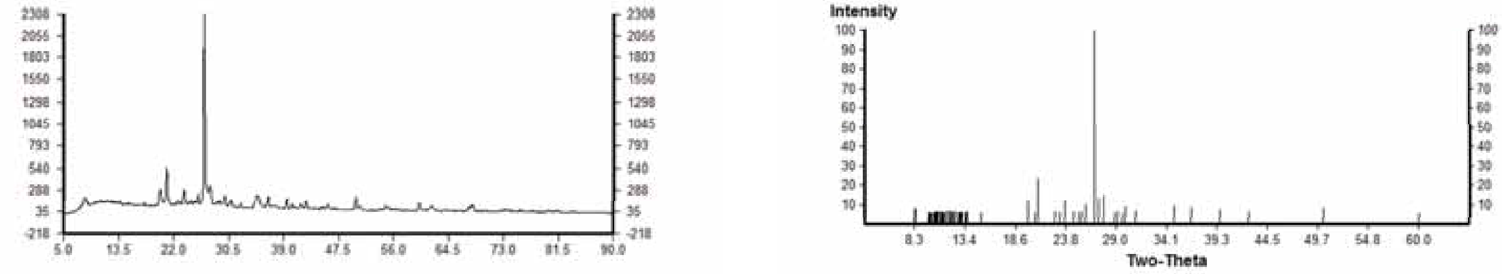

XRD 9

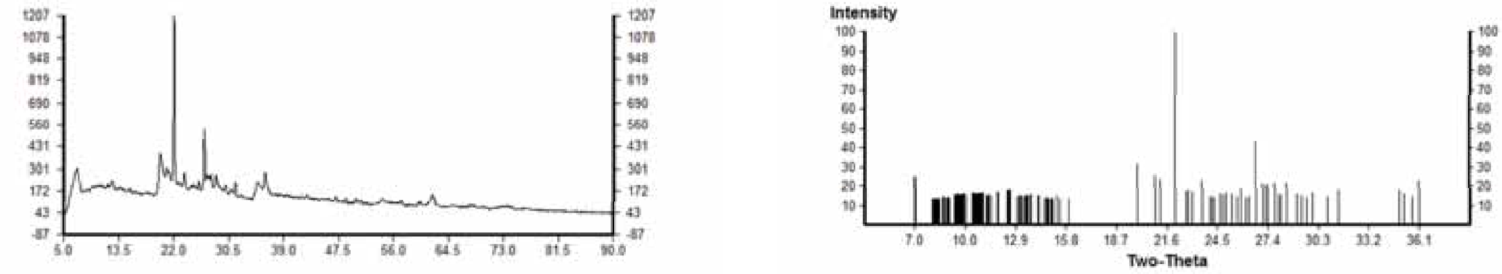

XRD 10

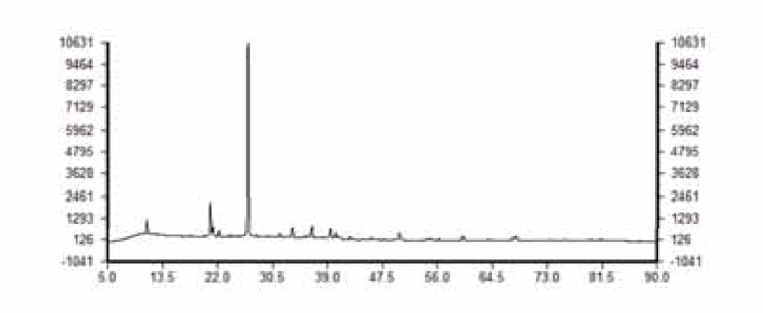

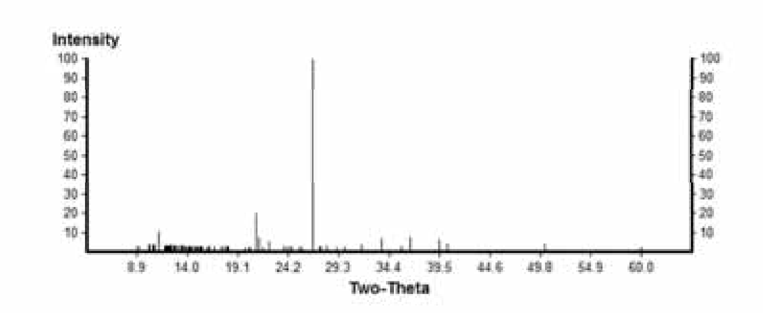

XRD 11

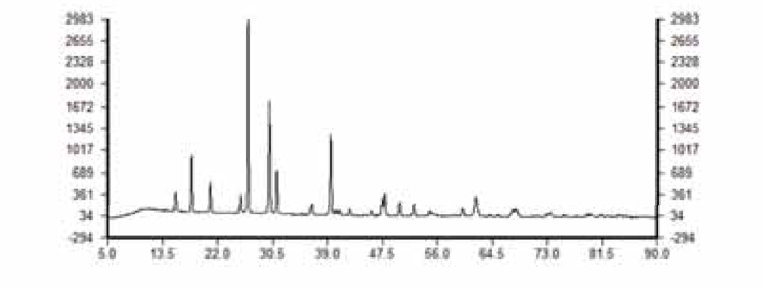

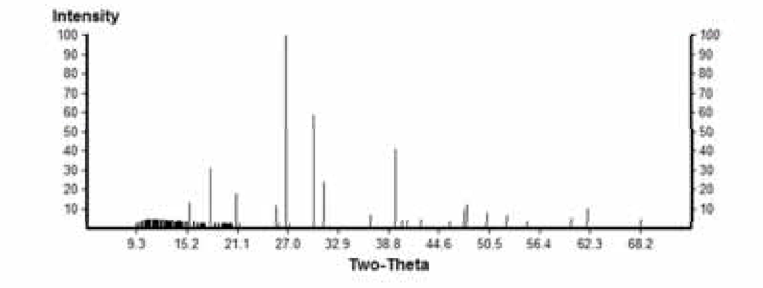

XRD 12

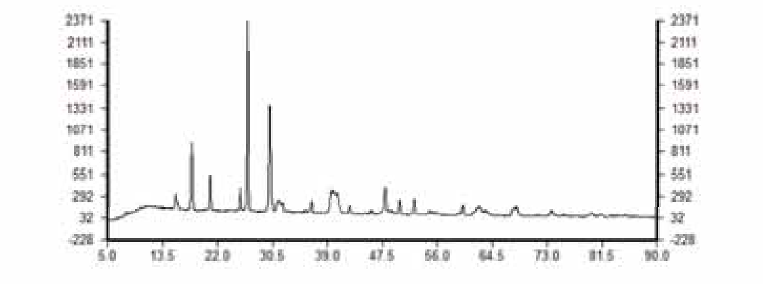

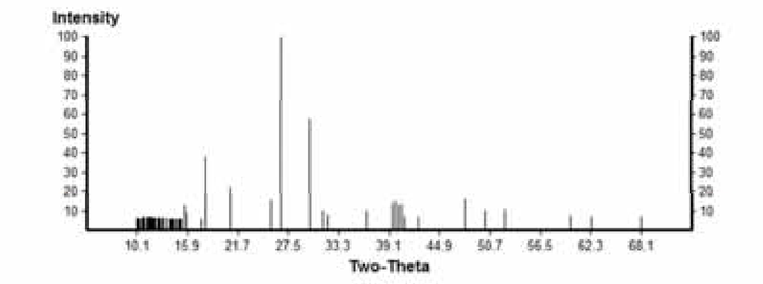

XRD 13

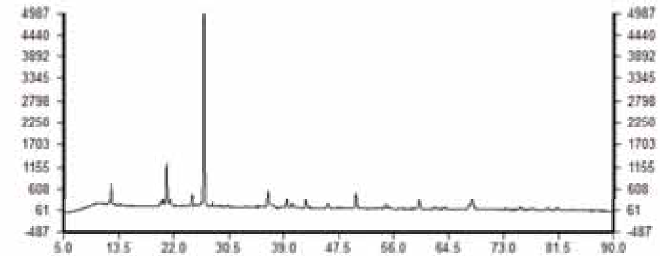

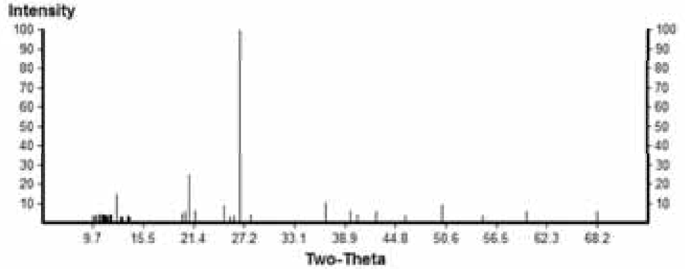

XRD 14

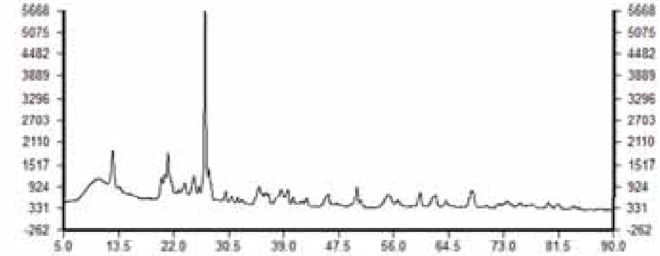

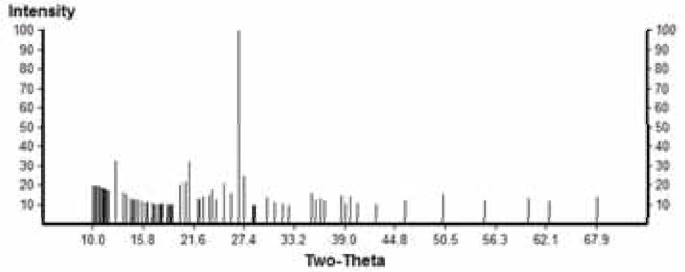

XRD 15

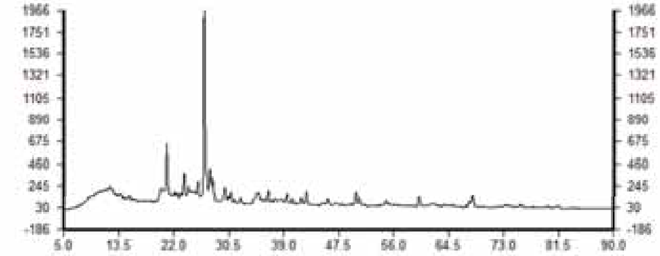

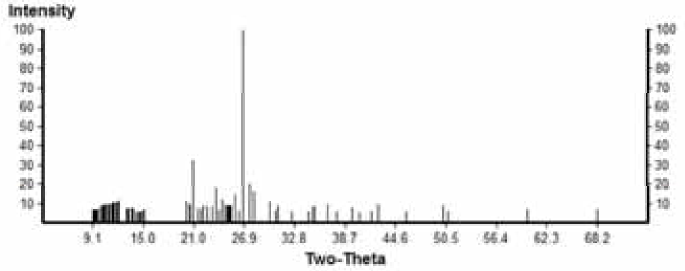

XRD 17

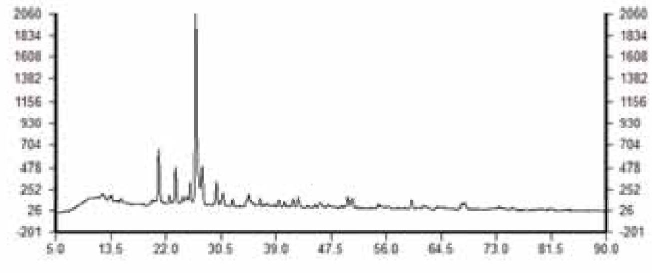

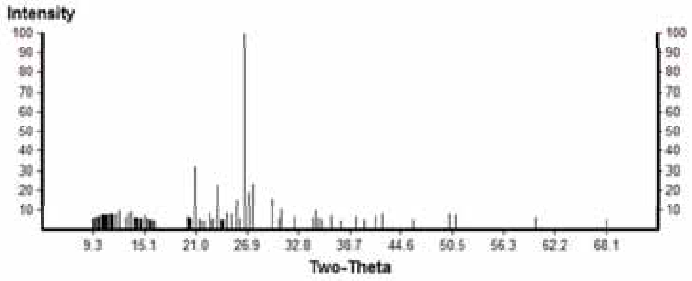

XRD 18

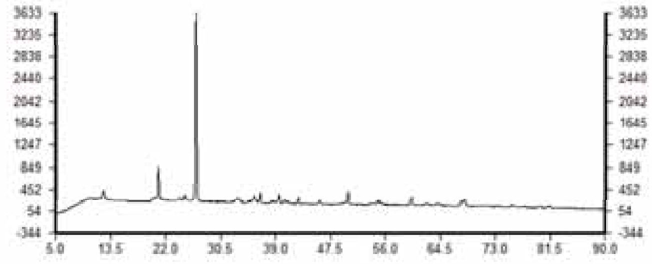

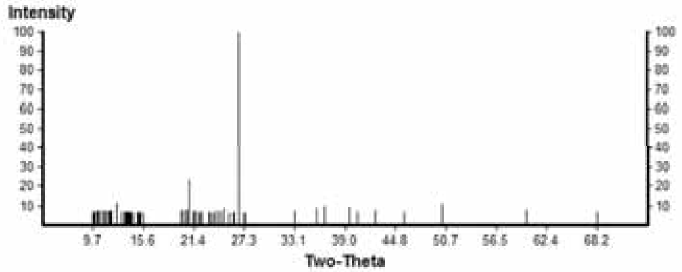

XRD 19

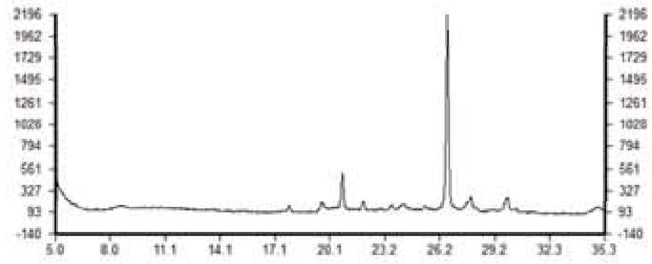

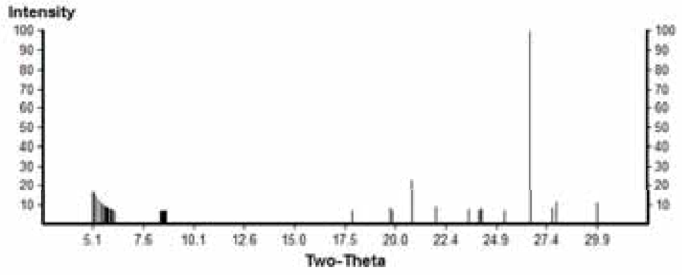

XRD 20

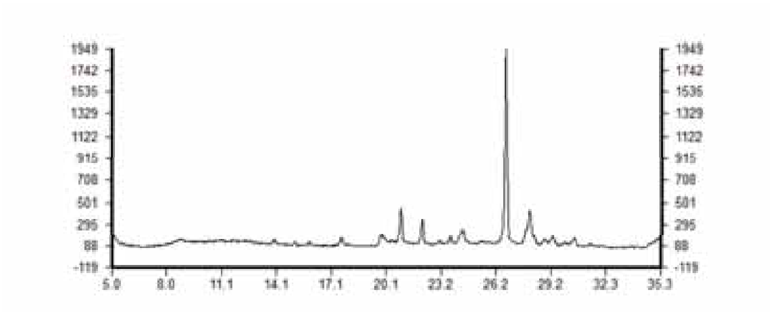
1949
1742
1535
1329
1122
915
708
501
295
88
-119
5.0
8.0
11.1
14.1
17.1
20.1
23.2
26.2
29.2
32.3
35.3

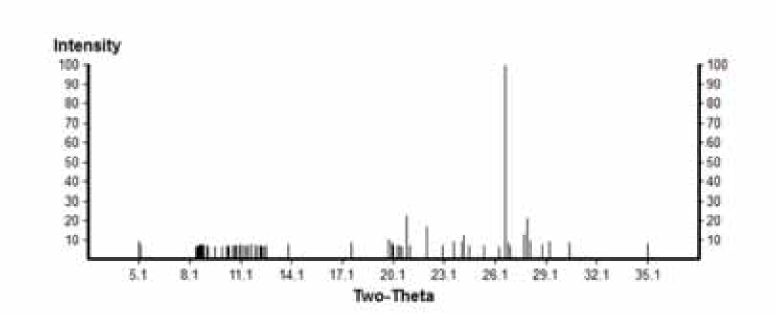
Intensity
100
90
80
70
60
50
40
30
20
10
5.1
8.1
11.1
14.1
17.1
20.1
23.1
26.1
29.1
32.1
35.1
Two-Theta

Appendix 7: Results of XRD analysis: position of the five most intense peaks. In bold letters are the peaks between 5 and 15 2θ degree

	1st peak			2nd peak			3rd peak			4th peak			5th peak		
	Angle (2θº)	**D-spacing (Å)**	**Intensity (%)**	**Angle (2θ°)**	**D-spacing (Å)**	**Intensity (%)**	**Angle (2θº)**	**D-spacing (Å)**	**Intensity (%)**	**Angle (2θ°)**	**D-spacing (Å)**	**Intensity (%)**	**Angle (2θº)**	**D-spacing (Å)**	**Intensity (%)**
XRD1	27.1	3.8	100.0	21.3	4.8	24.4	***9.2***	***9.5***	***6.8***	29.4	3.5	7.1	17.9	5.8	6.6
XRD2	***9.1***	***9.7***	***100.0***	35.3	2.9	92.8	20.1	5.1	91.2	12.6	8.1	81.9	26.3	3.9	24.6
XRD3	26.6	3.9	100.0	20.9	4.9	22.1	19.8	5.2	12.1	27.5	3.8	11.3	***8.8***	***10.1***	***7.5***
XRD4	27.1	3.8	100.0	21.3	4.8	32.5	***9.3***	***9.4***	***18.8***	27.5	3.8	16.7	36.9	2.8	15.9
XRD5	26.6	3.9	100.0	20.9	4.9	22.1	50.1	2.1	9.2	19.8	5.2	8.8	***8.6***	***10.3***	***5.5***
XRD6	26.7	3.9	100.0	28.0	3.7	26.8	20.9	4.9	26.6	23.6	4.4	12.6	***8.5***	***10.4***	***5.3***
XRD7	26.9	3.9	100.0	21.1	4.9	23.3	27.8	3.7	20.2	23.7	4.3	18.5	***8.7***	***10.2***	***9.0***
XRD8	26.7	3.9	100.0	20.9	4.9	23.8	27.6	3.7	15.1	19.9	5.2	12.7	***8.3***	***10.6***	***8.4***
XRD9	22.1	4.7	100.0	26.7	3.9	43.8	19.9	5.2	31.9	20.9	4.9	25.7	***7.0***	***11.8***	***25.2***
XRD10	26.7	3.9	100.0	20.9	4.9	20.1	***11.1***	***9.3***	***11.0***						
XRD11	26.7	3.9	100.0	30.0	3.5	59.0	39.5	2.6	41.5	18.0	5.7	31.4	***15.5***	***6.6***	***13.4***
XRD12	26.6	3.9	100.0	30.0	3.5	58.2	18.0	5.7	38.9	20.9	4.9	22.8	***15.6***	***6.6***	***13.6***
XRD13	26.7	3.9	100.0	20.9	4.9	25.1	***12.4***	***7.2***	***15.3***	36.6	2.8	11.1	50.2	2.1	10.1
XRD14	26.8	3.9	100.0	***12.6***	***7.0***	***33.2***	21.1	4.9	32.3	27.4	3.8	25.4			
XRD15	26.7	3.9	100.0	20.9	4.9	33.2	27.6	3.8	20.9	23.6	4.4	18.6	***12.2***	***7.6***	***12.1***
XRD17	26.6	3.9	100.0	20.9	4.9	32.0	27.6	3.8	23.7	29.8	3.5	15.9	***12.2***	***7.6***	***10.0***
XRD18	26.3	3.9	100.0	20.9	4.9	23.8	***12.4***	***7.2***	***11.9***	50.2	2.1	11.6	36.6	2.8	10.5
XRD19	26.6	3.9	100.0	20.8	5.0	23.4	27.9	3.7	11.9	29.8	3.5	11.9	***8.9***	***10.0***	***7.5***
XRD20	26.7	3.9	100.0	20.9	4.9	23.1	28.0	3.7	22.0	22.1	4.7	17.6	***10.3***	***8.5***	***7.1***

Appendix 8: TGA and 1st derivative TGA curves

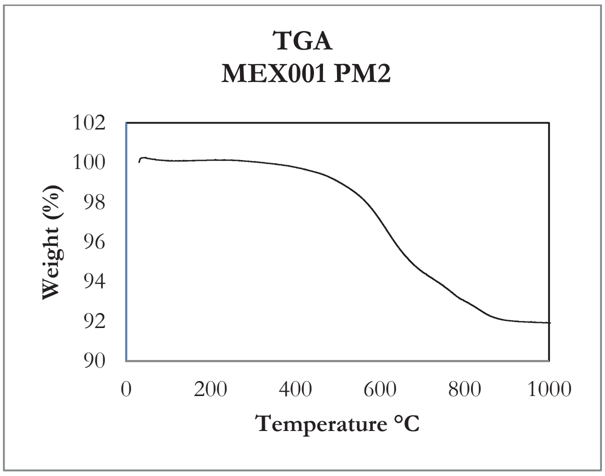

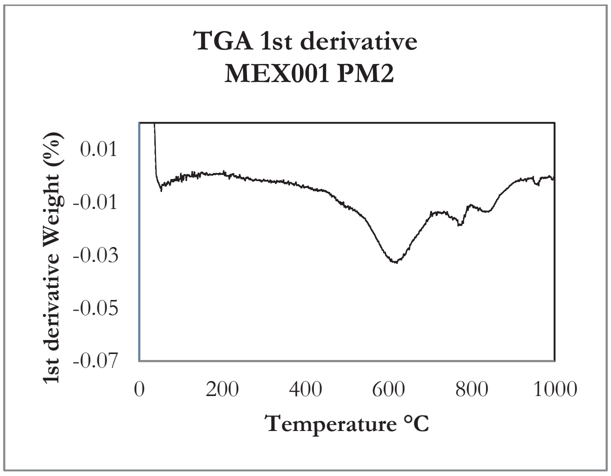

Sample size: 16.64 mg

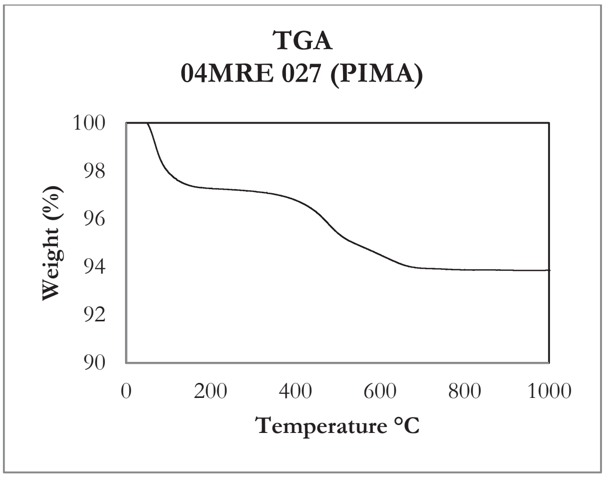

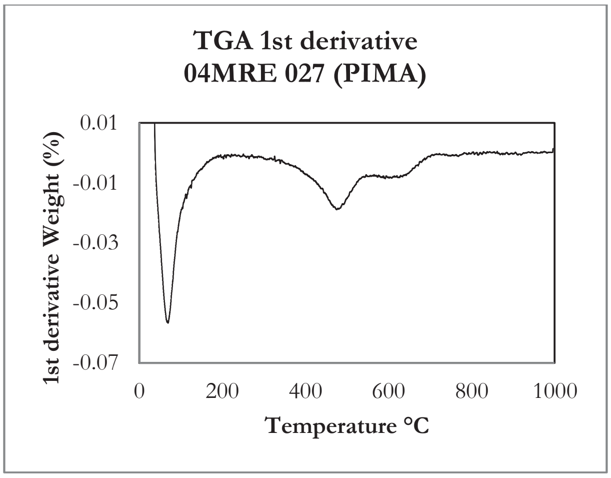

Sample size:12.84 mg

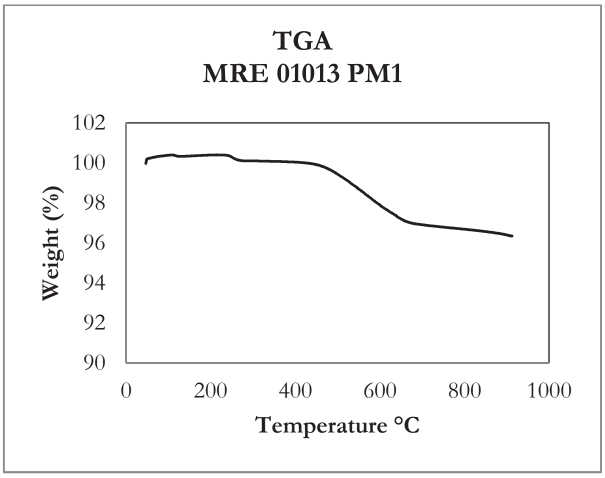

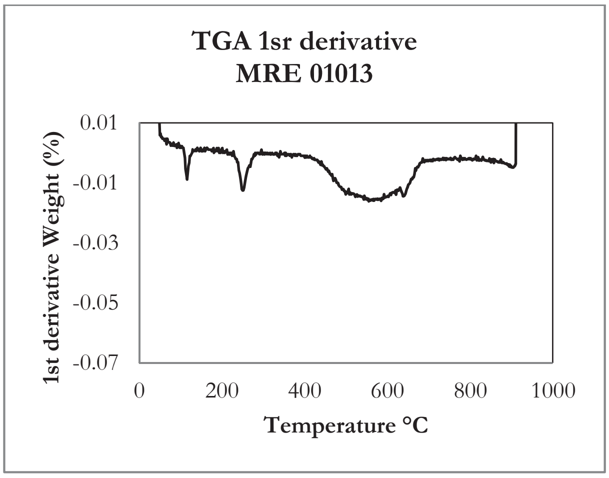

Sample size: 16.21 mg

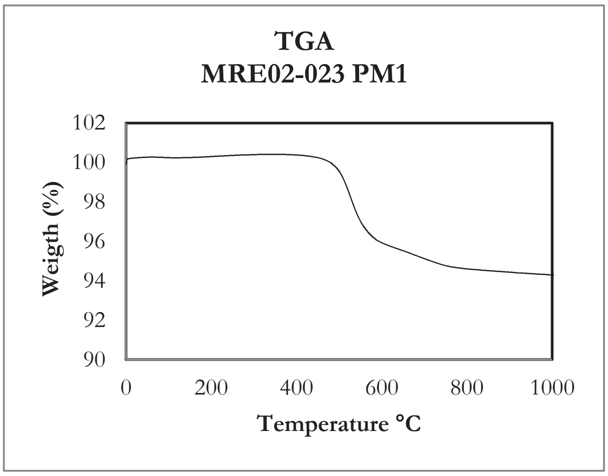

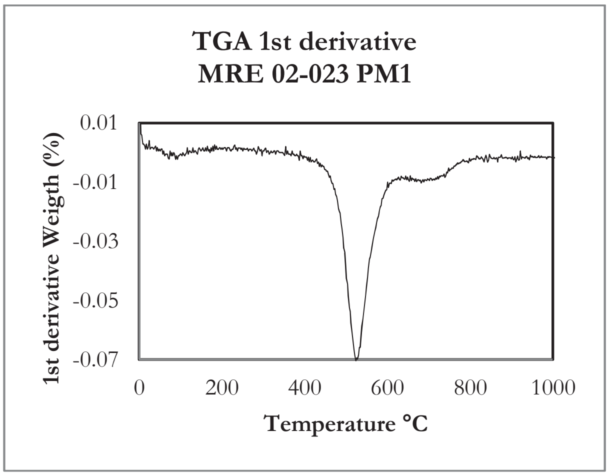

Sample size: 12.63 mg

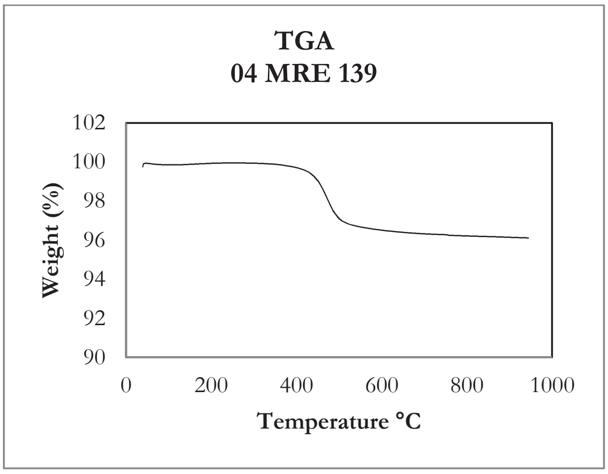

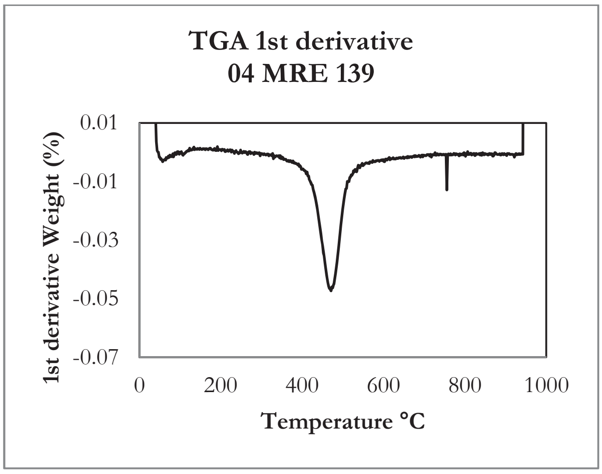

Sample size: 20.26 mg

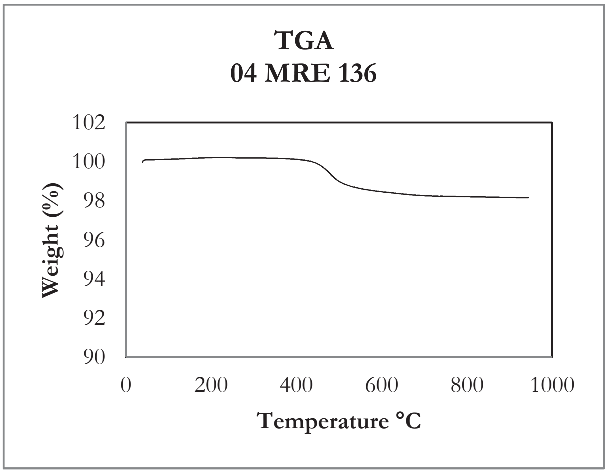

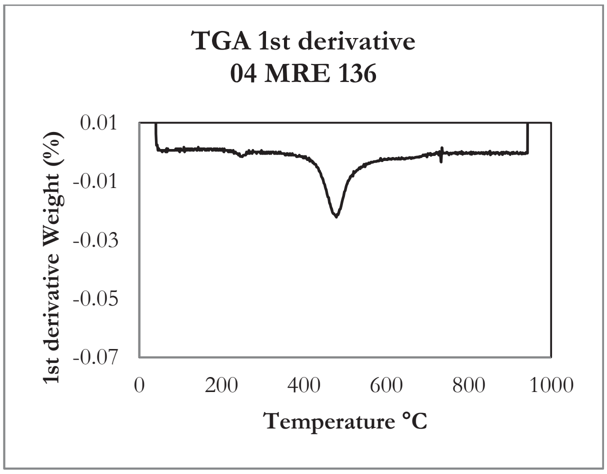

Sample size: 35.46 mg

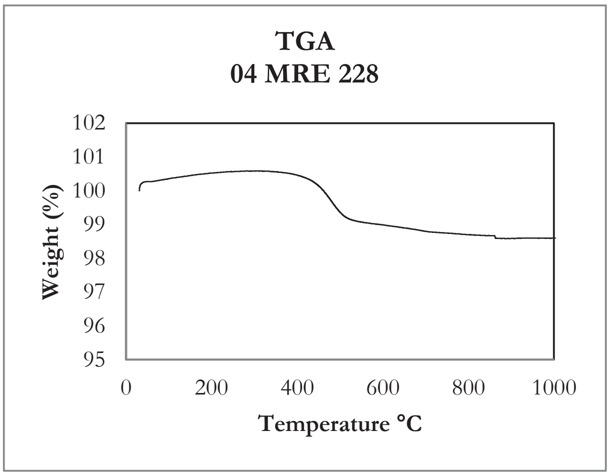
TGA
04 MRE 228

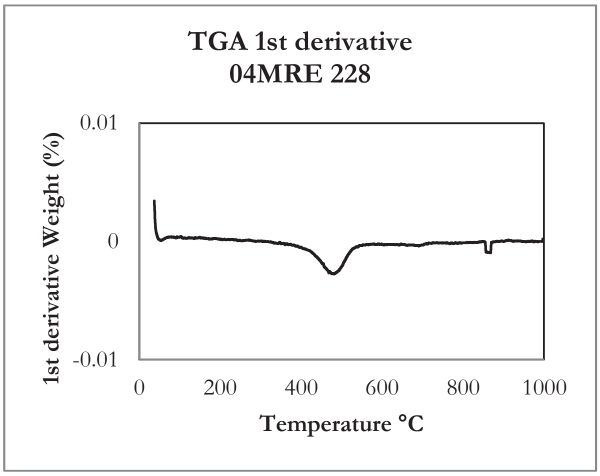
TGA 1st derivative
04MRE 228

Sample size: 15.68 mg

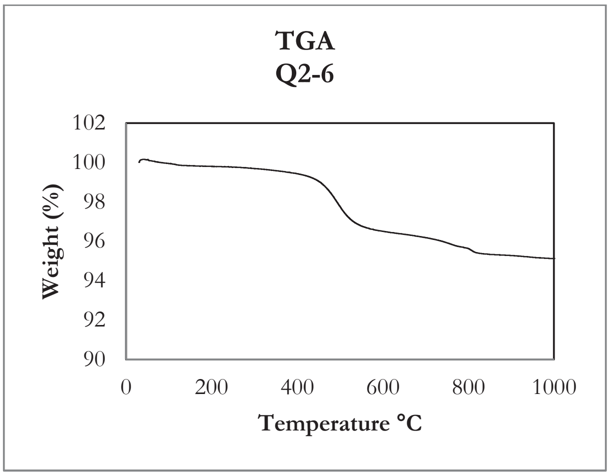
TGA
Q2-6

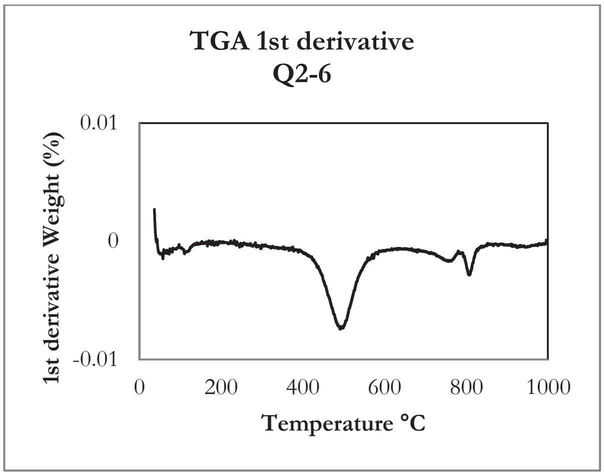
TGA 1st derivative
Q2-6

Sample size: 22.55 mg

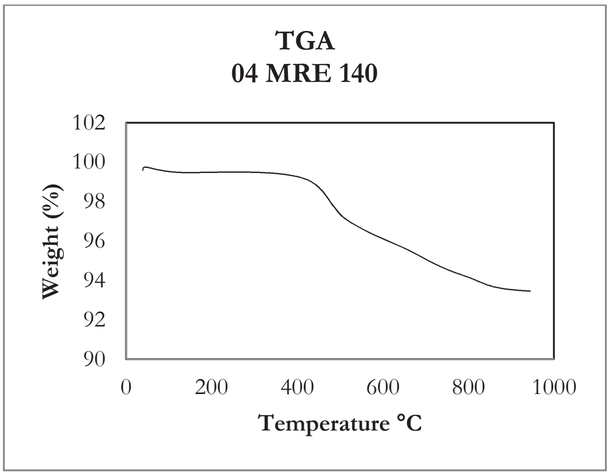
TGA
04 MRE 140

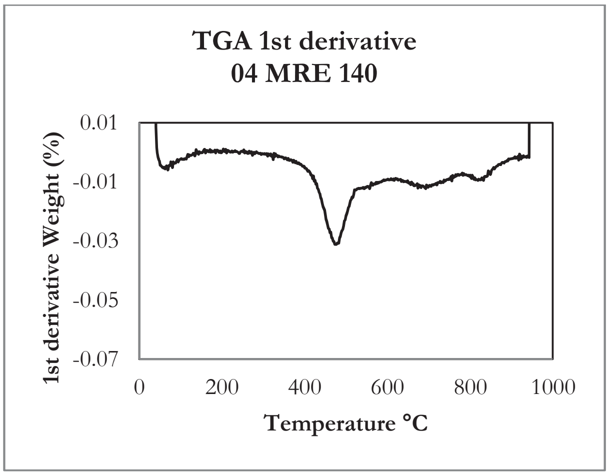
TGA 1st derivative
04 MRE 140

Sample size: 21.24 mg

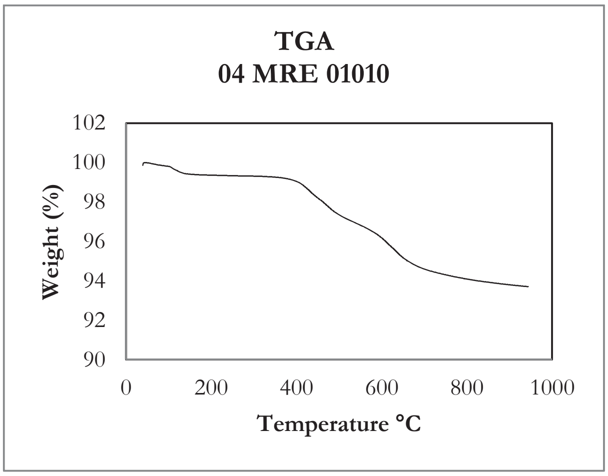

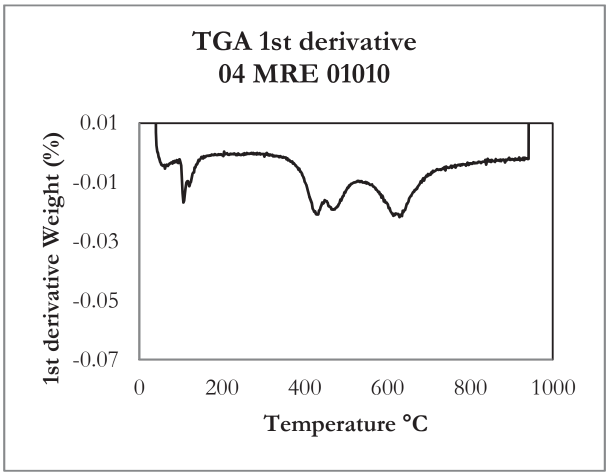

Sample size: 27.85 mg

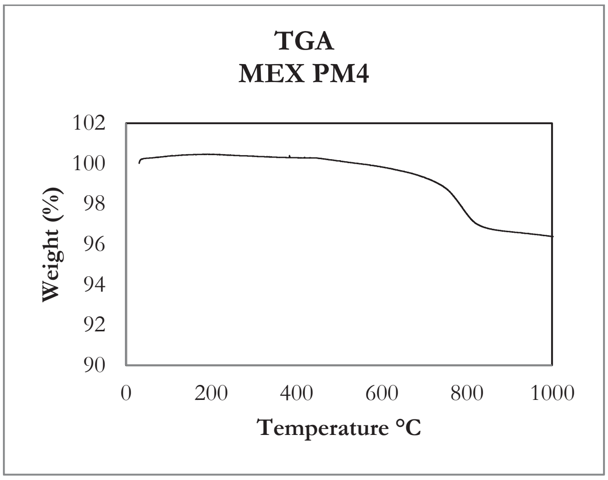

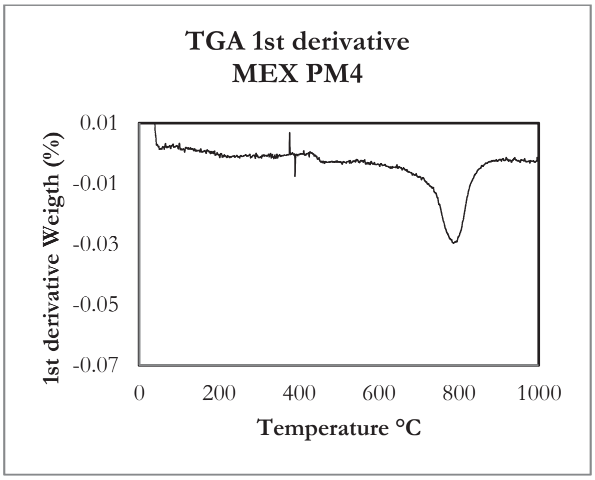

Sample size: 17.00 mg

Appendix 9: Identified mineralogy for SWIR (rock and powder), XRD and TGA analysis for a subset of samples

Sample	SWIR interpretation (rock)*	SWIR interpretation (powder)*	XRD interpretation	TGA interpretation
04MRE141	Illite (IS class 1)	Illite + jarosite (IS class 1)	Illite 2M1, quartz	NA
Mex 1-001-PM2	Illite (IS class 1)	Illite (IS class 1)	Illite 2M1 and Kaolinite 1Md	Illite/smectite (illite)
MRE-02-033 PM1	Illite (IS class 2)	Illite (IS class 2)	Illite 2M1, quartz, *adularia*	NA
MRE-01-006 PM1	Illite (IS class 2)	Illite (IS class 2)	Illite 2M1 and Halloysite, quartz, *adularia*	NA
MRE-01-008 PM1	Illite (IS class 3)	Illite (IS class 3)	Illite 2M2 and montmorillonite, quartz, quartz,	NA
04MRE 129	Illite + montmorillonite (IS class 4)	Illite (IS class 4)	Illite 1Md, quartz	NA
04MRE 146	Illite (IS class 4)	Illite + montmotillomnite (IS class 4)	Illite 1M and Illite 2M1, quartz	NA
04 MRE 123	Montmorillonite + illite (IS class 5)	Montmorillonite + illite (IS class 5)	Montmorillonite, quartz	NA
04MRE 027 PIMA	Montmorillonite (IS class 6)	Montmorillonite (IS class 6)	Montmorillonite and halloysite	Illite/smectite (montmorillonite) + kaolin (halloysite)
MEX 1-PM4	Zunyite	Zunyite	Zunyite, quartz	Pyrophyllite
04MRE 004(3) PIMA 002 C	K alunite	K alunite + halloysite	Alunite, quartz	NA
04MRE AQ 1-3	Na alunite	Na alunite	Alunite	NA
MRE 01013 PM1	Dickite	Dickite	kaolinite or dickite, quartz	Dickite
MRE 02-023 PM1	Kaolinite	Kaolinite + muscovite	kaolinite and montmorillonite, quartz	Kaolin (kaolinite) + Illite/smectite or muscovite
04MRE 139	Halloysite	Halloysite	halloysite and kaolinite, quartz	Kaolin (halloysite)
04 MRE 136	Mixture (halloysite-kaolinite)	Mixture (halloysite-kaolinite)	halloysite and kaolinite, quartz	Kaolin (halloysite)
04 MRE 228	Mixture (halloysite-illite)	Mixture (kaolinite-illite)	halloysite and kaolinite, quartz	Kaolin (halloysite)
Q2-6	Mixture (kaolinite- illite)	Mixture (kaolinite- illite)	halloysite, montmorillonite	Kaolin (kaolinite) +

			and kaolinite, quartz	illite/smectite
04MRE 140	Mixture (halloysite-illite)	Mixture (kaolinite-illite)	Montmorillonite, illite, halloysite, quartz	Kaolin (kaolinite) + Illite/smectite
MRE01010	Mixture (halloysite-illite)	Mixture (halloysite-illite)	Illite 1Md, halloysite, kaolinite and montmorillonite, quartz	Kaolin (Halloysite) + illite/smectite (montmorillonite)

NA= not analysed with this technique

* Interpretation for smectite-illite and kaolins is from the crystallinity analysis in the corresponding sections

Appendix 10: Estimation of the water absorption feature at HyMap resolution

Extrapolation of water absorption feature

In the HyMap scene, absorption related with the water feature is recorded only between 1.95-2.11 μm that correspond with part of the right slope of this feature. The wavelength of the maximum absorption is around 1.91 μm and might be calculated by extrapolating the slope till that wavelength (Figure 7-1). Two absorption points, P_1 and P_2, are taken to define the right slope of the feature, whereas P_3 is the expected position of the minimum value for the water absorption feature. A1, A2 and A3 are the wavelength position of P1, P2 and P3, respectively. D1 and D2 are the correspondent depths of P1 and P2, and D3 is the depth value of the water feature to calculate.

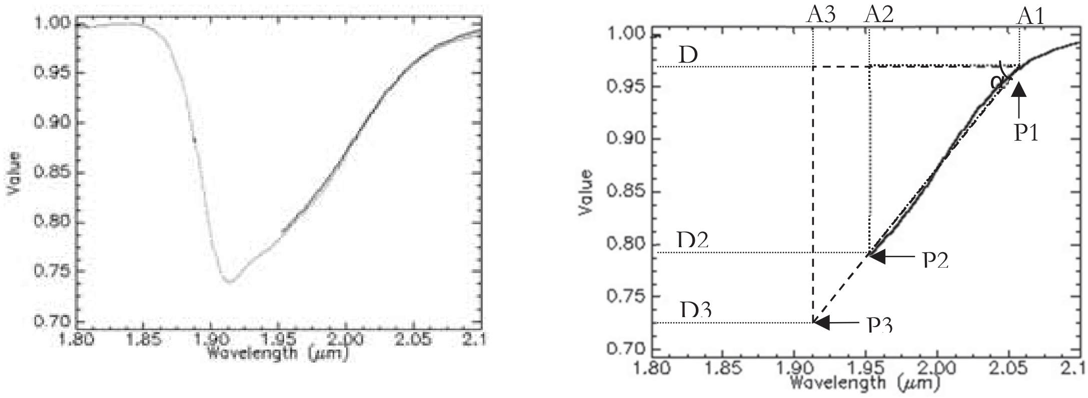

Figure 7-1 Left: comparison between laboratory spectra (dotted line) and resampled spectra to HyMap resolution (solid line), showing the missed part of the water feature in HyMap. Right: Parameters used in the depth extrapolation of the water feature on laboratory resampled spectra (thick solid line) based on known absorption points P1 and P2 (thin solid line) and the expected position of the feature P3 (dashed line).

Two triangles can be drawn from the absorption parameters in Figure 7-1. The first one (solid line) is defined by the depth and wavelength position of P1 and P2, whilst the second one (dashed line) is defined by the correspondent values of P1 and P3. Based on the given values, the function that suits better for the extrapolation of D3 is the tangent of the α angle, which is common for both triangles (equations 1 and 2). From them, expected depth of the water feature can be calculated using equation 4.

$$\tan\alpha = \frac{D2-D1}{A1-A2} \qquad \text{(eq. 1)}$$

$$\tan\alpha = \frac{D3-D1}{A1-A3} \qquad \text{(eq. 2)}$$

$$\frac{D2-D1}{A1-A2} = \frac{D3-D1}{A1-A3} \qquad \text{(eq. 3)}$$

$$D3 = D1 + (((A1-A3)*(D2-D1))/(A1-A2)) \qquad \text{(eq. 4)}$$

The depth of the water feature on the resampled spectra was estimated with the equation 4 using the HyMap band 101 centered at 2.06 μm as P1 and HyMap band 95 centered at 1.95 μm as P2. A3 is set as 1.915 μm from the average of the value of the water feature of illites, smectites and kandites observed in the laboratory spectra

Appendix 11: Masks used in HyMap processing

Mask	**Description**	**Thresholds**
NDVI	Abundant green vegetation	0.15 < NDVI <0.5
Cellulose	Abundant dry vegetation	Wavelength of minimum 2.00-2.15 μm Depth >0.03
Sulphate	Abundance of sulphates	Wavelength of minimum 1.730-1.780 μm Depth > 0.01
Smectite-illite and kaolinite FILTER 1*	Smectite-illite or kaolinite, depending the threshold, based on the secondary absorptions between 2.250-2400 μm	Filter 1>1.025 illite Filter 1<1.025 smectite Filter 1<1.025 kaolin
Smectite-illite and kaolinite FILTER 2*	Smectite-illite or kaolinite, depending the threshold, based on the secondary absorptions between 2.250-2400 μm	Filter 2<1.98 illite Filter 2<1.98 smectite Filter 2>1.98 kaolin
Smectite-illite maks	Selection of smectite and illite pixels	Filter 1 (illite) + filter 1 (smectite) + filter 2 (illite) + filter 2 (smectite)
Kaolin mask	Selection of kaolin pixels	Filter 1 (kaolin) + filter 2 (kaolin)

* After Cudahy et al. (2008)